

# **Plasma Turbulence Studies Using Correlation Doppler Reflectometry on the ASDEX Upgrade Tokamak**

Der Fakultät für Physik  
der Ludwig-Maximilians-Universität München  
zur Erlangung des akademischen Grades eines  
Doktors der Naturwissenschaften (Dr. rer. nat.)  
vorgelegte Dissertation

von

Jasmine Schirmer

aus Montreal

14.09.2005

Erstgutachter: Prof. Dr. Hartmut Zohm  
Zweitgutachter: Prof. Dr. Harald Lesch

Tag der mündlichen Prüfung: 21.11.2005

## Zusammenfassung

Eines der wichtigsten Ziele der Fusionsforschung mit magnetisch eingeschlossenen Plasmen ist das Verständnis und die Kontrolle der Turbulenz im Plasma. Die Turbulenz verursacht einen zusätzlichen radialen Teilchen- und Wärmetransport vom Plasmazentrum zu den umgebenden Strukturen, wodurch die Einschlussgüte vermindert wird. Diagnostiken zur Untersuchung der Plasmaturbulenz sind allerdings rar und beschränkt in ihren Möglichkeiten. Im Rahmen dieser Arbeit wurde eine neue Diagnostikmethode zur Messung von Plasmarotationsprofilen und Turbulenzeigenschaften, die Dopplerreflektometrie, weiterentwickelt. Ähnlich einem Mikrowellenradar werden hierbei die von denjenigen radialen Positionen im Plasma reflektierten Mikrowellen detektiert, an denen der Brechungsindex Null wird. Diese Diagnostikmethode wurde zur Messung der Turbulenzkorrelation erweitert, indem ein zweiter Dopplerreflektometerkanal hinzugefügt wurde, sodass nun zwei Mikrowellenstrahlen mit leicht unterschiedlichen Frequenzen ins Plasma eingekoppelt und detektiert werden können. So ein radiales Korrelations-Dopplerreflektometersystem kann simultan die Messwerte des radialen elektrischen Feldes  $E_r$  und seiner Verscherung  $\partial E_r / \partial r$  (beides Parameter für die ein fundamentaler Zusammenhang zur Turbulenzunterdrückung vermutet wird), zusammen mit Messungen der Eigenschaften der Plasmaturbulenz, wie z.B. der radialen Korrelationslänge der Turbulenz  $L_r$ , liefern. Messungen dieser Größen wurden im Rahmen dieser Arbeit für einen weiten Bereich von Plasmaparametern untersucht. Es hat sich herausgestellt, dass  $E_r$  und die zugehörige Verscherung tatsächlich mit dem Einschluss des Plasmas in Verbindung stehen: ihr Absolutwert am Plasmarand steigt mit der Einschlussgüte. Ebenso wurde ein Anstieg in der Verscherung von  $E_r$  an derselben radialen Position gefunden, an der die radiale Korrelationslänge der Turbulenz abfällt. Diese Beobachtung ist im Einklang mit theoretischen Modellen, die eine Unterdrückung der turbulenten Fluktuationen im Plasma bei ansteigendem Absolutwert der Verscherung vorhersagen, was zu einer Reduktion von  $L_r$  führt. Messungen von  $L_r$  in Abhängigkeit der senkrechten Komponente des Wellenzahlvektors  $k_{\perp}$ , wurden ebenfalls ausgewertet und führten zu einer Untersuchung der Antwortfunktion des Korrelations-Dopplerreflektometers. Hierfür wurde ein zweidimensionaler Algorithmus mit finiten Zeitschritten (FDTD — finite difference time domain code) verwendet. Die Simulationsergebnisse zeigen, dass der Absolutwert der gemessenen Korrelationslänge von den radialen, poloidalen und senkrechten Wellenzahlen der Turbulenz abhängt.

## Abstract

One of the major goals of the tokamak fusion program is the understanding and control of plasma turbulence. Turbulence causes additional radial transport of heat and particles to the tokamak vessel walls, thereby degrading the overall confinement of the plasma. Diagnostics for the study of tokamak turbulence are unfortunately scarce and limited in what they can measure. A new diagnostic technique, Doppler reflectometry, has been developed for measurements of plasma rotation profiles and turbulence properties. It is a type of microwave radar technique which uses the back-scatter of microwaves from a radial position in the plasma where the refractive index equals zero. In this thesis work, the technique is extended for turbulence correlation measurements by adding a second Doppler reflectometer channel where two microwave beams are launched into the plasma with a small frequency difference. A radial correlation Doppler reflectometer system can provide simultaneous measurements of the plasma radial electric field  $E_r$  and its shear  $\partial E_r / \partial r$  (both parameters are believed to be fundamental for suppressing turbulence) together with measurements of the properties of the plasma turbulence, such as the radial correlation length of the turbulence  $L_r$ . These measurements are explored in this thesis work for a wide range of plasma conditions. It was found that  $E_r$  and its associated shear are indeed linked to plasma confinement. Their absolute values increase with confinement at the plasma edge. An increase in the absolute value of  $E_r$  shear was also detected at the same plasma edge region where a decrease in radial correlation lengths of the turbulence was measured. This observation is in agreement with theoretical models which predict that an increase in the absolute shear suppresses turbulent fluctuations in the plasma, leading to a reduction in  $L_r$ . Measurements of  $L_r$  versus the perpendicular wavenumber of the turbulence  $k_{\perp}$  were also obtained, which prompted an investigation of the correlation Doppler reflectometer response function using a 2-dimensional finite difference time domain (FDTD) code. The simulation results show that the magnitude of the measured  $L_r$  is dependent on the radial, poloidal and perpendicular wavenumbers of the turbulence.

## Parts of this dissertation were published in:

J.Schirmer, G.D.Conway, W.Suttrop, H.Zohm and the ASDEX Upgrade Team, (2004) *Radial Electric Field Shear and Correlation Length Measurements in ASDEX Upgrade using Correlation Doppler Reflectometry*, in: Europhysics Conference Abstracts (CD-ROM, Proc. of the 31st EPS Conference on Plasma Physics, London, 2004), P-4.127.

J.Schirmer, G.D.Conway, W.Suttrop, S.Klunge, H.Zohm and the ASDEX Upgrade Team, (2004) *Plasma Turbulence Studies Using Correlation Doppler Reflectometry On The ASDEX Upgrade Tokamak*, in: Conference Digest of the 2004 Joint 29th International Conference on Infrared and Millimeter Waves and 12th International Conference on Terahertz Electronics, Karlsruhe, 2004, P-2.56.

J.Schirmer, G.D.Conway, H.Zohm, W.Suttrop, E.Holzhauer and the ASDEX Upgrade Team, (2005) *Radial Correlation Doppler Reflectometry on ASDEX Upgrade*, in: IPP-Report 2/9 (Proc. of the 7th International Reflectometry Workshop for Fusion Plasma Diagnostics, Garching, 2005).

G.D.Conway, J.Schirmer, W.Suttrop, S.Klunge, E.Holzhauer, D.Wagner, H.Zohm and the ASDEX Upgrade Team, (2003) *Latest results and future plans for Doppler reflectometry on ASDEX Upgrade*, in: Proc. 6th International Reflectometry Workshop for Fusion Plasma Diagnostics, San Diego, 2003.

G.D.Conway, J.Schirmer, S.Klunge, W.Suttrop, E.Holzhauer and the ASDEX Upgrade Team, (2004) *Plasma rotation profile measurements using Doppler reflectometry*, Plasma Physics and Controlled Fusion 46, 951-970.

D.P.Coster, A.Chankin, G.D.Conway, L.Horton, L.Kaveeva, C.Konz, J.Neuhauser, M.Reich, T.Ribeiro, V.Rozhansky, J.Schirmer, B.D.Scott, M.Tsalas, S.Voskoboynikov and the ASDEX Upgrade Team, *Edge simulations of an ASDEX Upgrade Ohmic shot*, in: Europhysics Conference Abstracts (CD-ROM, Proc. of the 32nd EPS Conference on Plasma Physics, Terragona, 2005), P-1.008.

L.D.Horton, G.D.Conway, A.W.Degeling, T.Eich, A. Kallenbach, P.T.Lang, J.B.Lister, A.Loarte, Y.R.Martin, P.J.McCarthy, H.Meister, J.Neuhauser, J.Schirmer, A.C.C.Sips, W.Suttrop and the ASDEX Upgrade Team, (2004) *ITER-relevant H-mode physics at ASDEX Upgrade*, Plasma Physics and Controlled Fusion 46, B511-B525.

L.D.Horton, A.V.Chankin, Y.P.Chen, G.D.Conway, D.P.Coster, T.Eich, E.Kaveeva, C.Konz, B.Kurzan, J.Neuhauser, I.Nunes, M.Reich, V.Rozhansky, S.Saarelma, J.Schirmer, J.Schweitzer, S.Voskoboynikov, E.Wolfrum and the ASDEX Upgrade Team, (2005) *Characterization of the H-mode edge barrier at ASDEX Upgrade*, Nuclear Fusion 45, 856-862.

H.Meyer, P.G.Carolan, G.D.Conway, G.Cunningham, L.D.Horton, A.Kirk, R.Maingi, F.Ryter, S.Saarelma, J.Schirmer, W.Suttrop, H.R. Wilson and the MAST, ASDEX Upgrade and NSTX teams, (2005) *H-mode physics of near double null plasmas in MAST and its applications to other tokamaks*, submitted to Nuclear Fusion.

Y.S.Na, G.D.Conway, O.Gruber, J.Hobirk, M.Maraschek, D.Nishijima, F.Ryter, J.Schirmer, A.C.C.Sips, A.Stäbler, G.Tardini and the ASDEX Upgrade Team, (2005) *Transport Studies in Improved H-mode at ASDEX Upgrade*, submitted to Nuclear Fusion.

# Acknowledgement

In the three years of this research work, I benefited from the knowledge, encouragement and support of several people. At this stage, I would like to express my gratitude.

It is a pleasure to thank my academic supervisor Professor Hartmut Zohm. He has given me the opportunity to take on this project and has bestowed on me support and trust. Our monthly meetings have given me the motivation I needed to complete this work.

I thank Dr. Garrard Conway for his supervision and for introducing me to the fascinating world of microwave technology. He has invested a tremendous amount of time in satisfying my curiosity. I am especially grateful to him for the last few months, in which he gave up his weekends for the correction of this thesis work.

I would also like to thank Dr. Wolfgang Suttrop who acted as my mentor. His support both academically and morally is greatly appreciated. Both his widespread knowledge in physics and his ability to explain difficult concepts in the simplest way continue to inspire me.

I am highly indebted to Dr. Eberhard Holzhauer, who has written the 2D FDTD code used in this thesis work. Although he is based in Stuttgart and has recently entered retirement, our constant telephone communication right until the end of this thesis kept the work on track and ensured progress in this field. The simulation results are a credit to him.

The Doppler reflectometry group at ASDEX Upgrade is fortunate to have Mr. Ewald Schmid as a technician. I have learned a lot from him about electronics and even had the opportunity to improve my Bayrisch at the same time.

I am thankful to Dr. Christoph Fuchs for providing a fitting program for density profiles, to Dr. Emanuele Poli who offered support in the use of the TORBEAM code and to Dr. Hans Meister who always had an answer to any IDL programming problem. I also appreciate Dr. Bruce Scott and Dr. Frank Jenko for taking on the difficult challenge of explaining tokamak turbulence theory to an experimentalist.

This thesis would surely not have been possible without the entire ASDEX Upgrade team. I benefited greatly from the numerous colleagues and friends which make up this team.



# Contents

<b>1</b>	<b>Introduction</b>	<b>1</b>
1.1	Fusion Energy . . . . .	1
1.2	Magnetic Confinement . . . . .	3
1.3	Plasma Turbulence . . . . .	4
1.4	Scope of this Work . . . . .	5
<b>2</b>	<b>Tokamak Operation</b>	<b>7</b>
2.1	The ASDEX Upgrade Tokamak . . . . .	7
2.2	Plasma Heating Systems . . . . .	10
2.3	Plasma Configuration . . . . .	11
2.3.1	Plasma Shape . . . . .	11
2.3.2	Magnetic Field Line Helicity and Co-/Counter- NBI Injection . . . . .	13
2.4	Plasma Scenarios . . . . .	15
2.4.1	Low Confinement versus High Confinement Discharges . . . . .	15
2.4.1.1	Edge Localized Modes (ELMs) . . . . .	17
2.4.2	Improved H-mode . . . . .	18
2.4.3	Quiescent H-mode . . . . .	18
<b>3</b>	<b>Plasma Turbulence</b>	<b>21</b>
3.1	Anomalous Transport . . . . .	21
3.2	Properties of Plasma Turbulence . . . . .	22
3.3	Turbulence Measurements in Tokamaks . . . . .	24
3.4	Turbulence Suppression . . . . .	25
3.4.1	The Radial Electric Field . . . . .	25
3.4.2	The Radial Electric Field Shear . . . . .	26
3.4.2.1	BDT Model . . . . .	28
<b>4</b>	<b>Doppler Reflectometer Diagnostic</b>	<b>31</b>
4.1	Theory of Doppler Reflectometry . . . . .	31

4.1.1	Fundamental Wave Theory . . . . .	31
4.1.2	Microwave Propagation in a Plasma . . . . .	32
4.1.2.1	The Ordinary Mode . . . . .	34
4.1.2.2	The Extraordinary Mode . . . . .	34
4.1.3	Principle of Doppler Reflectometry . . . . .	35
4.1.4	Reflectometer Signals : Homodyne versus Heterodyne Detection . . .	37
4.2	Doppler Reflectometer Diagnostic in ASDEX Upgrade . . . . .	39
4.2.1	Hardware Components . . . . .	39
4.2.2	Data Control and Acquisition . . . . .	41
4.3	Development of a new Correlation Doppler Reflectometer System . . . . .	42
<b>5</b>	<b>Measurement Technique &amp; Data Analysis</b>	<b>45</b>
5.1	Reflection Cutoff Layers . . . . .	45
5.1.1	Electron Density Profiles . . . . .	46
5.1.2	Poloidal Cross Sections of the Radial Cutoff Layers . . . . .	48
5.1.3	Beam Tracing with TORBEAM . . . . .	50
5.2	Obtaining the Doppler Shifted Frequency, $f_D$ . . . . .	52
5.2.1	Measurement Difficulties in H-mode . . . . .	53
5.3	Single Channel Doppler Reflectometer . . . . .	54
5.3.1	Calculation of the Perpendicular Rotation of the Turbulence . . . . .	55
5.3.2	Calculation of the ExB velocity and the Radial Electric Field . . . . .	56
5.4	Dual Channel Doppler Reflectometer . . . . .	57
5.4.1	Calculation of the Radial Electric Field Shear . . . . .	57
5.4.2	Calculation of the Radial Correlation Lengths of the Turbulence . . .	58
5.5	Errors in the Doppler Measurement . . . . .	61
<b>6</b>	<b>Perpendicular Rotation Measurements</b>	<b>63</b>
6.1	The L-H Transition . . . . .	63
6.2	ExB Velocity Components . . . . .	65
6.2.1	The Toroidal Impurity Velocity . . . . .	65
6.2.2	The Ion Diamagnetic Velocity . . . . .	66
6.2.3	The Poloidal Velocity . . . . .	67
6.3	Dependence on Plasma Confinement . . . . .	67
6.4	Dependence on Plasma Configuration . . . . .	68
6.5	Dependence on Magnetic Field . . . . .	71
6.6	Summary . . . . .	72

<b>7</b>	<b>The Radial Electric Field and its Associated Shear</b>	<b>75</b>
7.1	Measurement of the Radial Electric Field . . . . .	75
7.1.1	Dependence on Plasma Confinement . . . . .	75
7.1.2	Dependence on Plasma Heating . . . . .	78
7.1.3	Dependence on Plasma Shape . . . . .	81
7.1.4	Comparison with Modeled $E_r$ Profiles . . . . .	84
7.2	Measurements of the Radial Electric Field Shear . . . . .	85
7.3	Summary . . . . .	88
<b>8</b>	<b>Radial Correlation Length of the Turbulence</b>	<b>91</b>
8.1	Experimental Measurements . . . . .	91
8.1.1	Radial Correlation Lengths in L-mode and H-mode . . . . .	91
8.1.2	$L_r$ as a Function of Plasma Normalized Radius . . . . .	92
8.1.3	The Relationship Between $L_r$ and $k_{\perp}$ . . . . .	93
8.2	2D Full Wave Simulation of Doppler Reflectometry . . . . .	95
8.2.1	The 2D Finite Difference Time Domain Full Wave Code . . . . .	95
8.2.2	The Input Parameters . . . . .	96
8.2.2.1	Experimental Electron Density and Magnetic Field . . . . .	96
8.2.2.2	Antenna Characteristics . . . . .	97
8.2.2.3	Modeling Turbulent Density Fluctuations . . . . .	98
8.2.3	Obtaining $L_r$ from the 2D Full Wave Code . . . . .	99
8.2.4	Testing of the 2D Code . . . . .	100
8.2.4.1	Radial Electric Field Patterns and Density Fluctuation Levels	101
8.2.4.2	The I and Q Output Signals . . . . .	104
8.2.5	Results . . . . .	106
8.3	Summary . . . . .	111
<b>9</b>	<b>Conclusions and Outlook</b>	<b>113</b>



# Chapter 1

## Introduction

The World Energy Council projects that by the year 2050 the world wide energy demand will be double its present level. With such expected high energy consumption, the need for new long-term sources of energy is evident. At present day, the main energy sources consist of exhaustible resources of coal, gas, and oil. These sources are known for creating air pollution and are thus, not considered environment friendly. Other energy sources include hydroelectric, solar and wind power, the exploitation of which is limited to specific locations. Even nuclear power in the form of fission, although capable of producing large amounts of inexpensive fuel, is not favorable due to the radioactive waste created. In light of this information, alternative forms of energy should be investigated to ensure a future energy supply which is both diverse and sustainable.

### 1.1 Fusion Energy

Fusion, as a possible new source of energy, was first considered in the late 1930s once it had been recognized as the power of the sun and other stars [1]. Since then, fusion research has been undertaken in laboratories all over the world aimed at reproducing fusion on Earth in a controlled manner. Fusion is a process where atomic nuclei of light elements are combined to form heavier elements, thereby releasing energy. The sun generates its energy by fusing hydrogen isotopes into stable helium in three steps:



Reaction 1.1 requires a weak interaction in order to transform protons to neutrons. This weak interaction makes these fusion processes very slow. Nevertheless, the sun (and all other stars) overcome the slow reaction rates due to their large mass. On Earth, however, this weak interaction and its associated small reaction probability must be avoided since a fusion reactor

is many orders of magnitude smaller than a star. Possible candidates for fusion reactions on Earth are:



These reactions are induced by collisions between their reactant particles and therefore their cross sections are of fundamental importance. The cross sections for these reactions can be seen in figure 1.1.

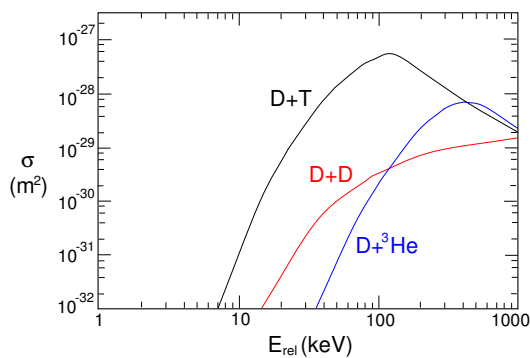


Figure 1.1: *Cross sections for different fusion reactions.*

The reactants essential for reaction 1.4 are deuterium and tritium. Deuterium, a hydrogen isotope, can be extracted from our oceanic waters, about 30 grams per cubic meter of water. If burned in a fusion reactor, this amount of deuterium could produce as much energy as 300 cubic meters of gasoline, clearly demonstrating the huge amounts of energy which are to be gained using fusion. Tritium, on the other hand, is an unstable radioactive isotope of hydrogen and therefore does not occur naturally. Nevertheless, tritium can be produced in a nuclear reaction between the neutrons, released from the D-T reaction, and lithium, an element found in great supplies in the Earth's crust.

To achieve 'ignition', a condition where fusion becomes self-sustaining without additional applied heating, the D-T atoms must be first heated by external means to sufficiently high temperatures (at least 20 keV). The high temperature increases the thermal motion of the electrons and nuclei so that they separate. A hot gas, where nuclei and electrons are no longer bound together, is called a plasma. In addition to heating the plasma, one must also confine the hot plasma. The cross section for Coulomb collisions is greater than the cross section for fusion and hence, many attempts are needed for a fusion collision. Confinement is necessary to keep the electrons and nuclei trapped in a specific volume for a sufficient length of time to undergo the fusion reaction and to minimize heat loss. The fusion reaction then provides itself the total energy required to heat the plasma from the fusion-born alpha particles and ignition is finally

At low energies, the cross section for fusion is small due to the Coulomb barrier preventing the nuclei of the reactants to approach each other close enough to fuse [2]. This repulsive force is eventually overcome as the kinetic energy of the nuclei increases. Actually, the deuterium-tritium reaction (reaction 1.4) can occur even before the Coulomb barrier is overcome because of quantum mechanical tunneling. From figure 1.1, it can be seen that reaction 1.4 has the highest cross section at lowest energies and is therefore the most promising reaction.

reached. The progress towards ignition can be expressed as a parameter,  $nT\tau_E$  where  $n$  is the density,  $T$  the temperature and  $\tau_E$  the energy confinement time. The energy confinement time gives an indication of the quality of the heat insulation. It increases with the volume of the plasma since a larger plasma is better confined in the core than a smaller plasma. Figure 1.2 shows the research progress of several international fusion devices towards ignition. It is expected that the next generation device ITER will come close to or reach ignition.

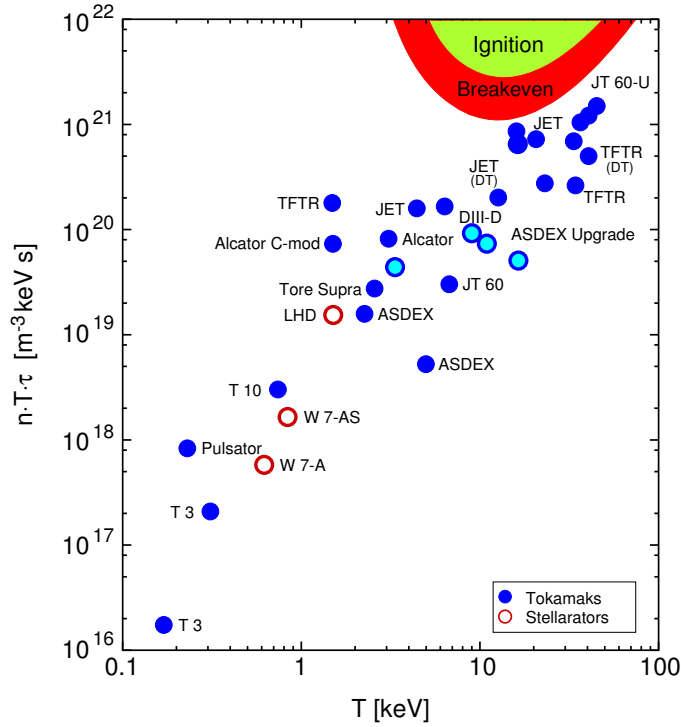


Figure 1.2:  $nT\tau_E$  values in different experiments.

## 1.2 Magnetic Confinement

There are several methods for confining a plasma, whereby the most feasible approach is magnetic confinement. In an external magnetic field, charged particles follow a helical gyro-orbit along the magnetic field lines and therefore their orbits are confined to the field lines within an order of the gyro-radius. This makes it possible to confine a plasma effectively in a magnetic configuration. A linear magnetic configuration (i.e. a cylinder) has been proved inadequate for fusion confinement due to the large end losses involved. These losses can be completely avoided by closing the field lines in what is known as a toroidal configuration (i.e. a torus). However, such a configuration with a pure toroidal magnetic field is subject to particle losses arising from various drifts. The curvature of the magnetic field and its gradient create the so-called grad B drift which separates ions and electrons in the vertical direction. This gives rise to an electric field  $E$ , which leads to an outward  $E \times B$  drift of the whole plasma. By

adding helicity to the magnetic field lines (i.e. a poloidal magnetic field component), the field lines become twisted and the undesirable drifts are compensated for. Presently, there are two main toroidal devices taking advantage of helical magnetic field lines: the stellarator and the tokamak, as seen in figure 1.3.

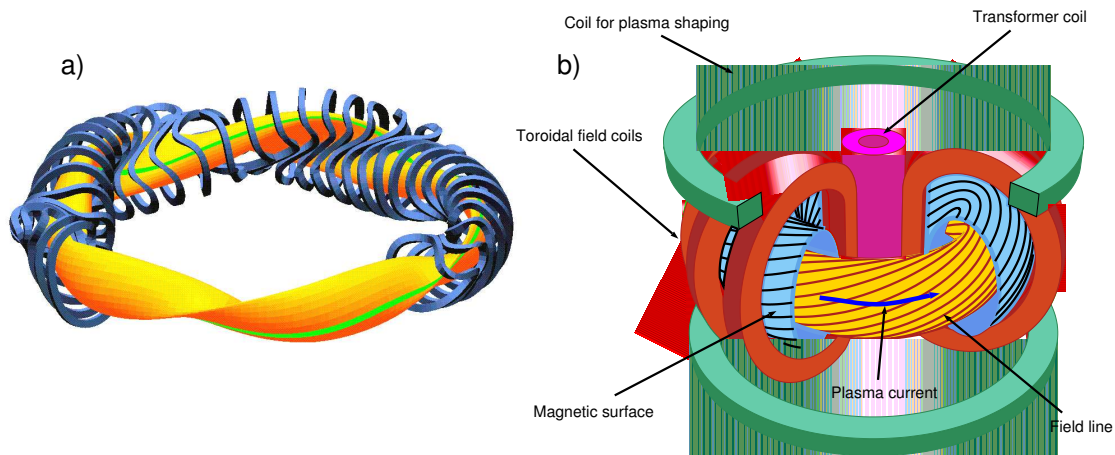


Figure 1.3: *Schematic Drawing of a Stellarator (a) and a Tokamak (b).*

In a stellarator, the poloidal magnetic field is generated by a complicated winding of external coils. The advantage of such a device is its potential to sustain a steady-state plasma. No strong plasma current is needed to maintain the poloidal magnetic field. Nevertheless, the tokamak is preferred at present due to its simple coil geometry (from the engineering point of view) and its toroidal symmetry. In a tokamak, the toroidal magnetic field is generated by the toroidal field coils whereas the poloidal magnetic field is created by the plasma toroidal electric current. This plasma current is induced by a central solenoid transformer where the plasma acts as the secondary winding of the transformer core. Since a transformer can induce current only for a finite time, alternative methods for driving current need to be researched to achieve steady-state tokamak operation. The additional vertical field coils illustrated in figure 1.3(b) are mainly for plasma shaping and stability. Further details about tokamaks and in particular, the ASDEX Upgrade Tokamak, operated at MPI Garching, on which this thesis is based, can be found in chapter 2.

### 1.3 Plasma Turbulence

In a tokamak, a set of nested magnetic flux surfaces are formed by the helical field lines as can be seen in figure 1.3(b). Each surface has the topology of a torus and does not intersect with the other surfaces. On each magnetic surface, plasma parameters are nearly constant since the charged particles are moving parallel to the magnetic field and so particle transport is fast. Perpendicular to the flux surfaces (in the radial direction), the transport is slow and as a result, plasma parameters (such as mass, charge and energy) may vary in this direction. Their

variation leads to gradients in the plasma, resulting in fluxes which determine the structure of the plasma [3].

The rate of transport in a tokamak caused by Coulomb collisions is known as *neoclassical transport*. Tokamak experiments have shown that ion thermal transport is similar to the neoclassical prediction, although electron thermal transport is substantially higher [4, 5]. In addition, plasmas with auxiliary heating exhibit even higher transport rates than those without external heating (i.e. Ohmic plasmas). Hence, the predictions of neoclassical transport do not support the experimental measured values of total fluxes. As a result, transport is often *anomalous*. This *anomalous transport* has long been believed to be caused by micro-instabilities in the plasma [6]. The fluctuations in the electric and magnetic fields caused by micro-instabilities lead in turn to fluctuations in the velocities and positions of the plasma particles, and thus to transport.

The incoherent type of motion arising from plasma instabilities is denoted turbulence. Understanding plasma turbulence and how to control it are the key issues dominating the realization of a reactor relevant tokamak. The gradients in the plasma are recognized as the driving forces for the multitude of turbulence existent in a plasma. Nevertheless, it was found that the mechanism for turbulence stabilization is generic for many types of turbulent fluctuations [7]. It is now widely accepted that a sheared  $E \times B$  flow deforms and tears the turbulent eddies in the plasma, reducing their radial correlation extent and thus limiting the transport of energy and particles across the field lines [8]. The importance of the  $E \times B$  shear flow make measurements of the radial electric field in a plasma  $E_r$  and in particular its first derivative  $\partial E_r / \partial r$  highly desirable.

## 1.4 Scope of this Work

Plasma turbulence and its relationship to anomalous transport is one of the most important outstanding problems of tokamak research. The major obstacle for validating a satisfactory theory of turbulence in tokamaks is a scarcity of experimental data. For studying micro-turbulence in tokamaks, a variety of diagnostics such as laser and microwave scattering, beam emission spectroscopy (BES) and heavy-ion beam probe (HIBP) exist. These diagnostics are used for measuring turbulent fluctuations in one or several of the plasma parameters: density, temperature, potential and magnetic field. However, the majority of fluctuation diagnostics have limitations. They are either heat sensitive and as such cannot measure far into the plasma core or they are expensive and their analysis is complicated. Another diagnostic, namely standard reflectometry, has had some success in particular in its measurement of density fluctuations. Reflectometry offers good resolution and is not restricted to the plasma edge. As well, the technique does not perturb the plasma as it is based on the reflection of a microwave beam from a location of given plasma density and magnetic field, corresponding to an index of refraction of zero (i.e. plasma cut-off position). A relatively new extension of this diagnostic is Doppler reflectometry, having first been introduced around 1999. It is based on the back-scatter of microwaves from a plasma cut-off position. Thus, it is a hybrid diagnostic, combining the wavenumber sensitivity of scattering diagnostics with the radial resolution of standard reflec-

tometry. The main difference to standard reflectometry is that the microwave beam in the Doppler reflectometry technique is launched into the plasma at an oblique angle,  $\theta_{tilt}$ . Consequently, the diagnostic selects density perturbations with wavenumbers in the reflecting cut-off layer perpendicular to the magnetic field ( $k_{\perp} = 2k_o \sin\theta_{tilt}$ ) according to the Bragg condition. To date, Doppler reflectometry has been used for the measurement of the propagation velocity of these perturbations,  $u_{\perp}$  [9, 10, 11]. The perpendicular rotation is obtained from the Doppler shift of the returning microwave. Since the perpendicular rotation is a measure of the plasma  $E \times B$  velocity, the plasma radial electric field  $E_r$  may be extracted. This is one aspect of the diagnostic, which is studied in this thesis. A survey in both perpendicular rotation and radial electric field measurements are presented for a variety of plasma conditions in the ASDEX Upgrade tokamak.

Furthermore, by using two microwave sources at slightly different frequencies, several properties of the turbulence may be inferred. This technique developed as a part of this thesis project is called correlation Doppler reflectometry. For the first time, the technique is used for the measurements of radial electric field shear  $\partial E_r / \partial r$  and radial correlation lengths  $L_r$  of the turbulence. These parameters are of major interest to the fusion community since  $E_r$  shear is believed to be fundamental for turbulence suppression and  $L_r$  gives an indication of the type of turbulence and its behaviour in the plasma. The relationship between  $L_r$  and  $k_{\perp}$ , obtained experimentally by the correlation Doppler reflectometer, can give additional information on the turbulence. The measurements however revealed unexpected behaviour, which motivated the undertaking of numerical simulations of the Doppler reflectometer response using a 2-dimensional full-wave finite-difference time-domain (FDTD) code.

This thesis is organized as follows: chapter 2 reviews basic tokamak operation, such as possible plasma configurations and heating since the measurements presented are obtained from a wide scope of plasma discharges. Chapter 3 describes the types of turbulence relevant in tokamaks and the diagnostics used for measuring its properties. Chapter 4 introduces the principle of Doppler reflectometry as a diagnostic for plasma turbulence measurements while chapter 5 describes the methods and techniques used for data analysis. In chapters 6 through 8, the experimental measurements of perpendicular rotation, radial electric field and its shear and radial correlation lengths are presented. Chapter 8 also includes the simulation results from the 2D full-wave code. Finally, the conclusions and outlook are given in chapter 9.

# Chapter 2

## Tokamak Operation

This chapter is an introduction to basic tokamak operation. The emphasis is placed on the ASDEX Upgrade tokamak, upon which this thesis work is based. The various plasma scenarios, configurations and tokamak heating systems employed on ASDEX Upgrade will be described. These topics will be touched upon again in the discussion of the Doppler reflectometry measurements.

### 2.1 The ASDEX Upgrade Tokamak

The ASDEX Upgrade tokamak, named after its predecessor ASDEX (**A**xiSymmetric **D**ivertor **E**Xperiment), is a middle sized tokamak with a major radius of 1.65m and a minor radius of 0.5m. The technical data and main parameters of the device are listed in Tables 2.1 and 2.2. ASDEX was one of the first tokamaks to use a divertor concept. With the help of a divertor, the impact of wall contact on plasma operation is minimized, thereby keeping the plasma well confined and free of undesirable impurities. Consequently, this improvement in plasma confinement led to the discovery of the high confinement mode (H-mode) on ASDEX [12]. An H-mode plasma has roughly double the energy confinement time than the earlier low confinement mode (L-mode) plasmas. Both these plasma scenarios, along with several others, will be described further in section 2.4.

One of the main goals of ASDEX Upgrade is to provide data needed for next generation fusion devices, such as ITER. Figure 2.1 illustrates the poloidal cross sections of ASDEX Upgrade and ITER. A poloidal cross section offers a view of a vertical slice through one side of the donut-shaped tokamak. In the poloidal cross sections of figure 2.1, the principal components of these two tokamaks may be seen. An array of vertical magnetic field coils, controlling the plasma shape, and the primary winding of the transformer are illustrated as yellow boxes. The green outer layer represents the tokamak toroidal field coils. Not shown in the ASDEX Upgrade cross section, is the vacuum chamber which encloses the plasma and is needed to provide low base pressure and control the hydrogen pressure outside the plasma. In the core of the tokamaks, the plasmas are outlined in red. The similarity between the two cross sections indicates the ITER relevance of ASDEX Upgrade.

**Technical data:**

Total height of the experiment	9 m
Total radius over all	5 m
Weight of the experiment	800 t
Material of the first wall	approx. 70% tungsten, 30% carbon
Number of toroidal field coils	16
Number of poloidal field coils	6
Maximum magnetic field	3.1 T
Plasma current	0.4 MA - 1.4 MA
Pulse duration	< 10 s
Time between pulses	15 - 20 min
Amount of data / pulse	approx. 1 GByte
Plasma heating:	up to 30 MW
Ohmic heating	1 MW
Neutral beam injection heating	20 MW (with $^2\text{H} = \text{D}$ )
Injection energy	60 keV and 93 keV
Ion-Cyclotron heating	8 MW (30 MHz - 120 MHz)
Electron-Cyclotron heating	2 MW (140 GHz)

Table 2.1: *Technical data of ASDEX Upgrade as of 2005***Typical plasma parameters:**

Major plasma radius $R_0$	1.65 m
Minor horizontal plasma radius $a$	0.5 m
Minor vertical plasma radius $b$	0.8 m
Ellipticity $b/a$	1.8
Triangularity (top/bottom)	0.4 / 0.4
Plasma types	deuterium, hydrogen, helium
Plasma volume	14 m <sup>3</sup>
Plasma mass	3 mg
Electron density	1 x 10 <sup>20</sup> m <sup>-3</sup>
Plasma temperature	60 to 250 million degree

Table 2.2: *Typical plasma parameters of ASDEX Upgrade*

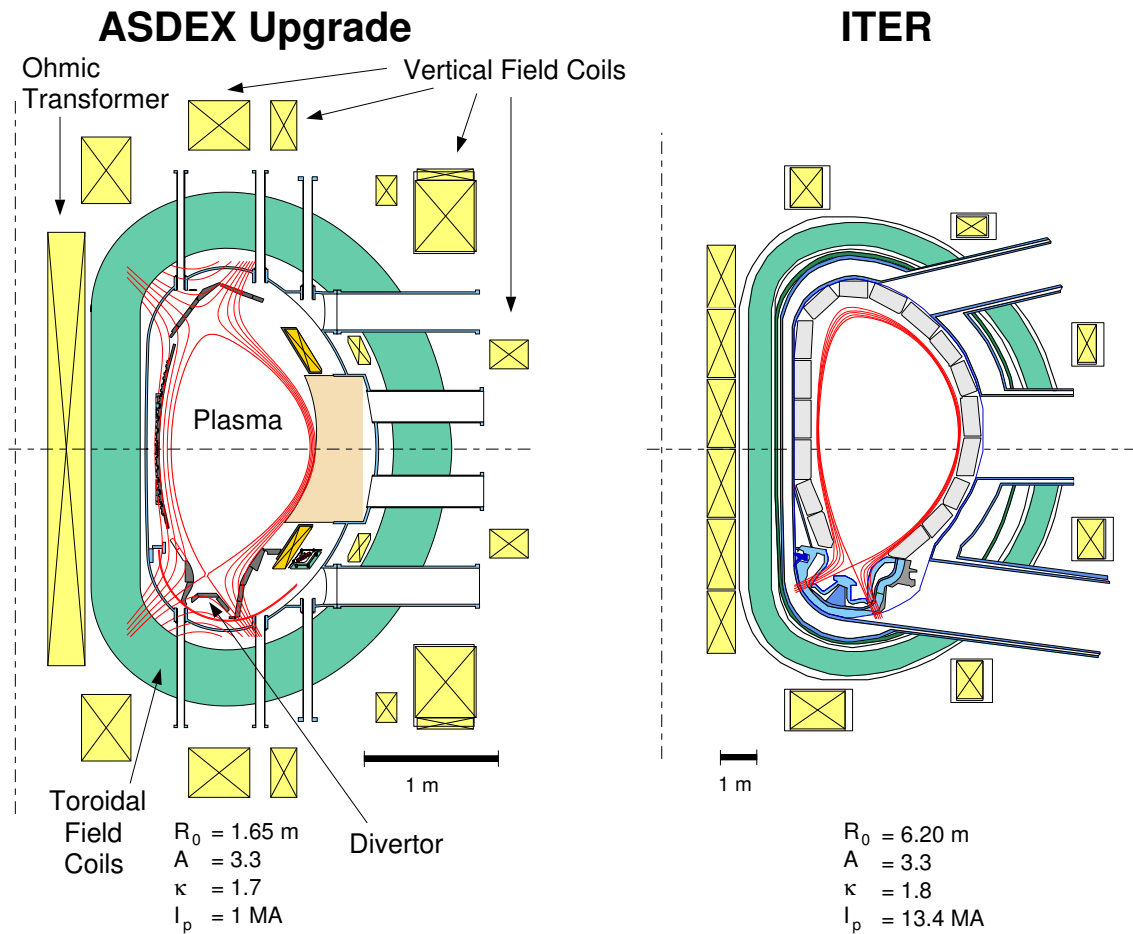


Figure 2.1: Comparison of the poloidal cross sections of ASDEX Upgrade and ITER.

Current research emphasis includes investigating the physics of advanced tokamak regimes and testing of alternative first wall materials, such as tungsten [13]. Advanced tokamak scenarios include internal transport barriers and improved H-mode scenarios. These advanced scenarios are of key interest in fusion research since they may lead to enhanced plasma performance, long hybrid operation and even possibly steady state operation. The investigation of alternate wall materials is of particular importance since future tokamaks, such as ITER, might not use carbon as a first wall material. Carbon is subject to strong chemical erosion and can entrap tritium in deposited layers. Hence, ASDEX Upgrade has entered a multistep program toward a carbon-free machine by slowly replacing its carbon with tungsten.

For studying such physics issues, ASDEX Upgrade is equipped with an extensive set of diagnostics. A wide variety of measurements, such as electron density and ion and electron temperatures, are routinely measured on ASDEX with state-of-the-art systems. These diagnostics are continually being improved while new diagnostics are also being developed. For example, the majority of the results presented in this thesis are obtained from the newly developed Doppler reflectometry diagnostic. In addition to the various diagnostics, three types of

heating systems on ASDEX Upgrade allow a greater variety of experiments to be performed. These heating systems are briefly described in the following section.

## 2.2 Plasma Heating Systems

Current flowing in the plasma produces ohmic heat due to finite resistivity. However, this heat is not sufficient for heating the plasma to fusion relevant temperatures. Consequently, three auxiliary heating systems are employed on ASDEX Upgrade. They are neutral beam, ion cyclotron and electron cyclotron heating. These systems supply a maximum of 30MW heating power. Their positions around the tokamak with several other diagnostics are shown in figure 2.2.

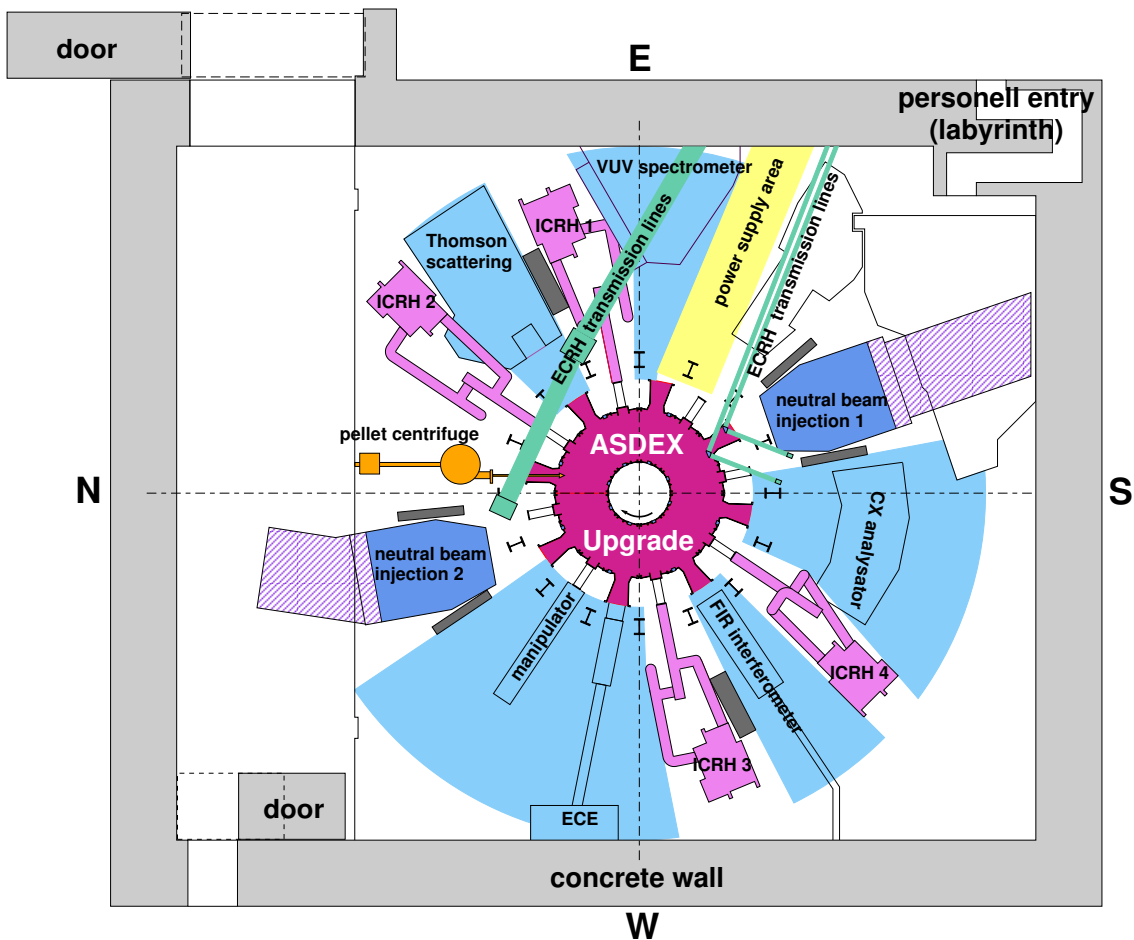


Figure 2.2: Schematic of the ASDEX Upgrade experimental hall, showing the positions of the heating systems and several plasma diagnostics.

The neutral beam injector (NBI) heating system consists of two injectors, each of which can launch 10MW of power into the plasma [14, 15]. A beam of ionized deuterium is produced

and accelerated in an electric field. By propagating through a neutralizer chamber filled with neutral deuterium gas, the fast particles become neutralized by charge exchange reactions. They then undergo further charge exchange reactions upon entering the plasma, resulting in a population of fast ions. The plasma heating is then produced by collisions of the fast ions with the thermal particles. This heating method is responsible for the toroidal momentum input in a plasma, which drives the plasma toroidal rotation,  $v_\phi$ .

The other two heating systems, known as Electron Cyclotron Resonance Heating (ECRH) and Ion Cyclotron Resonance Heating (ICRH), are based on a wave heating method. They launch electromagnetic waves into the plasma with frequencies in the range of the electron (140GHz) and ion (30-120MHz) cyclotron frequencies respectively.

The ICRH heating system consists of four generators, each capable of launching 2MW of power into the tokamak vessel via four antennae in the vacuum chamber [16]. The ICRH power is absorbed in the plasma by either ions or electrons. Where the frequency matches the local ion cyclotron resonance frequency, direct absorption by ions occurs. If however there is no strong ion absorption and the phase velocity of the wave is near the thermal velocity of the electrons, direct absorption by electrons takes place. This heating power is suitable for experiments studying fast particles as well as the effects on plasmas without momentum input (normally provided by NBI heating).

ECRH heating power, on the other hand, is ideal for studies related to electron heat transport via heat waves. This heating power is currently generated by four diode-type gyrotrons operated at 140GHz frequency, corresponding to the second harmonic electron cyclotron resonance at 2.5T [13]. A maximum of 2MW per 2s pulse length is achievable with the system.

## 2.3 Plasma Configuration

The tokamak machine was designed such that plasma configuration could be altered. The shape and position of the plasma is controlled by a set of vertical field coils. By increasing or decreasing the strength of the various vertical magnetic fields produced by these coils, the plasma may be moved up or down, in or out, as well as create field nulls, i.e. X-points at the top and bottom of the plasma donut. In addition, the polarity of the toroidal magnetic field and the toroidal current (i.e. the poloidal magnetic field) may be reversed. This then changes the magnetic field line helicity of the plasma as well as the co or counter direction of the NBI with respect to the main plasma current, since the toroidal injection angles of the NBI sources are fixed on ASDEX Upgrade. A change in the plasma configuration can have dramatic effects on plasma performance and therefore these aspects need to be addressed in tokamak research.

### 2.3.1 Plasma Shape

The most common plasma shape is the Lower Single Null (LSN) shape, where the plasma, in a poloidal cross section, is round at the top and forms an X-point at the bottom divertor position (see figure 2.3). This X-point defines a boundary magnetic surface called the separatrix. At

the X-point, the poloidal field is zero. A safety factor  $q$  describes the geometry of the field lines in a tokamak and is defined by

$$q = \frac{m}{n} = \frac{\text{number of toroidal circulations}}{\text{number of poloidal circulations}} \quad (2.1)$$

For example, a  $q = 2/1$  magnetic surface has closed field lines after two toroidal and one poloidal windings. At the separatrix, the safety factor  $q$  goes to infinity. Outside the separatrix is a region defined as the Scrape Off Layer (SOL). Particles and energy from the main plasma migrate across the field lines to the SOL where they flow down to the divertor and become neutralized at the target plates. Hence, strong heat flow and particle fluxes are expected at the plates since the magnetic field lines intersect the plasma vessel at these points. In order to study plasma performance in the various plasma shapes, a tokamak needs to be specially designed to withstand the excessive erosion which can occur at these points. ASDEX Upgrade has divertor plates at the top and bottom of the vacuum vessel and hence most plasma shapes may be tested, thus enabling a wide variety of plasma experiments to be undertaken and the associated physics to be studied. It will later become evident that the three regions of a plasma (i.e. plasma core, edge and SOL) are usually treated separately. This is because the physics in each of these regions are unique and the behavior in all three is very different.

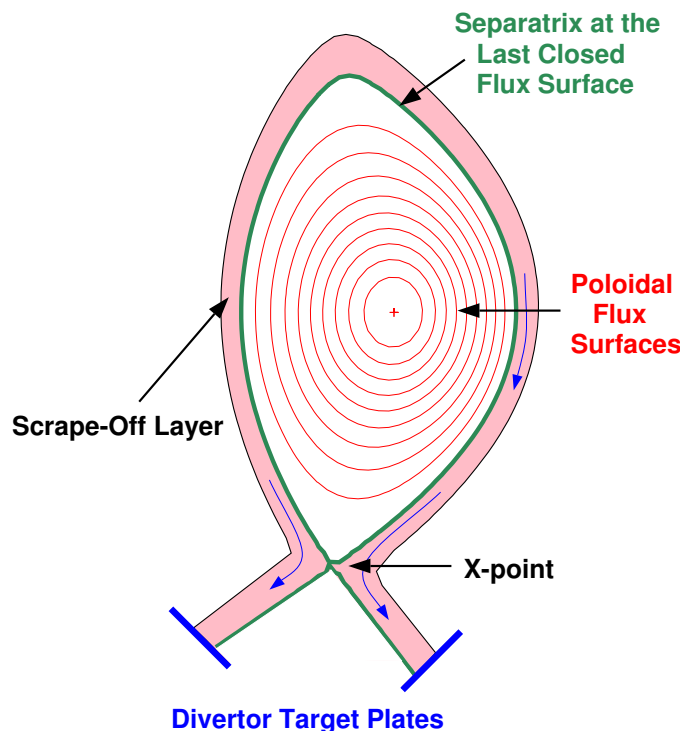


Figure 2.3: A plasma poloidal cross section illustrating the poloidal flux surfaces and the flow of particles in the SOL to the divertor plates. The separatrix is defined as the boundary of the last closed flux surface and the SOL is the region outside the separatrix.

Generally, the lowest non-circular moments defining the plasma poloidal cross sectional shape

are elongation ( $\kappa$ ) and upper ( $\delta_{upper}$ ) and lower ( $\delta_{lower}$ ) triangularity. For example, a typical LSN discharge would have a small  $\delta_{upper}$  and a large  $\delta_{lower}$ . By moving the plasma in the  $z$  direction (i.e. up or down), the vertical field coil strengths in the plasma are changed and two other plasma shapes, namely the Double Null (DN) and Upper Single Null (USN) shapes, may be created. All three shapes are shown in figure 2.4 with several poloidal flux surfaces in proportion to the tokamak vessel. The DN configuration forms two X-points, one at the top and one at the bottom. Table 2.3 lists the three plasma shapes (shown in figure 2.4) in discharge # 19415 and the triangularities typical of these shapes.

Discharge #19415

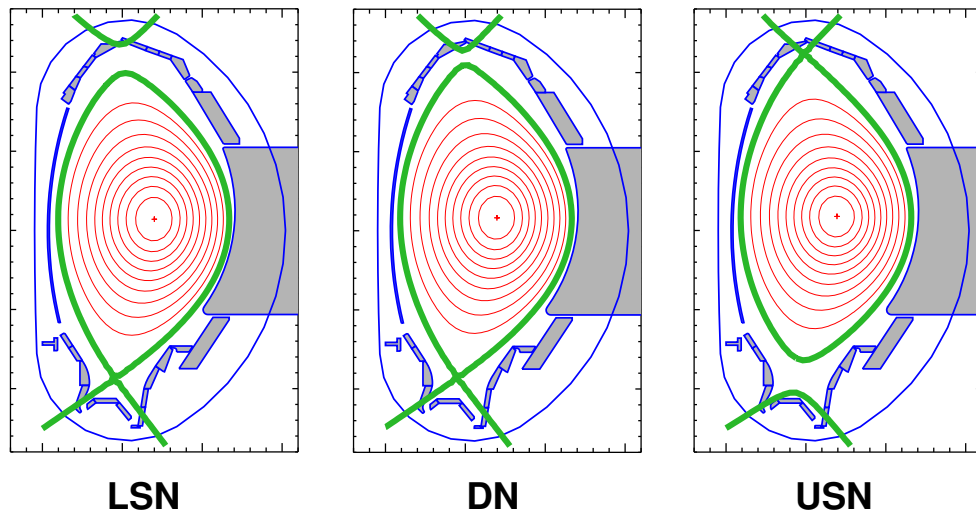


Figure 2.4: The various plasma shapes achievable on ASDEX Upgrade.

Plasma Shape	Time (s)	$\delta_{upper}$	$\delta_{lower}$
LSN	3.0	0.205	0.334
DN	4.4	0.220	0.333
USN	5.8	0.269	0.265

Table 2.3: The various plasma shapes in discharge # 19415 with their upper and lower triangularities. The most common plasma shape used on ASDEX Upgrade is LSN.

### 2.3.2 Magnetic Field Line Helicity and Co-/Counter- NBI Injection

On ASDEX Upgrade, the standard discharge configuration has a negative toroidal magnetic field ( $-B_\phi$ ) and a positive plasma current ( $+I_p$ ). Here positive is defined as toroidally counter-clockwise and negative clockwise when viewed from above. The  $+I_p$  creates a poloidal magnetic field  $B_\theta$  directed downward on the outbound side of the tokamak. This combines with

the  $-B_\phi$  to create a left-handed helicity of the total  $B$  field. However, both the direction of  $B_\phi$  as well as  $I_p$  may reverse directions such that four configurations are possible. The four possibilities are sketched in figure 2.5. Of the four possible configurations, the  $-B_\phi, +I_p$  is preferred on ASDEX Upgrade for LSN discharges for several reasons.

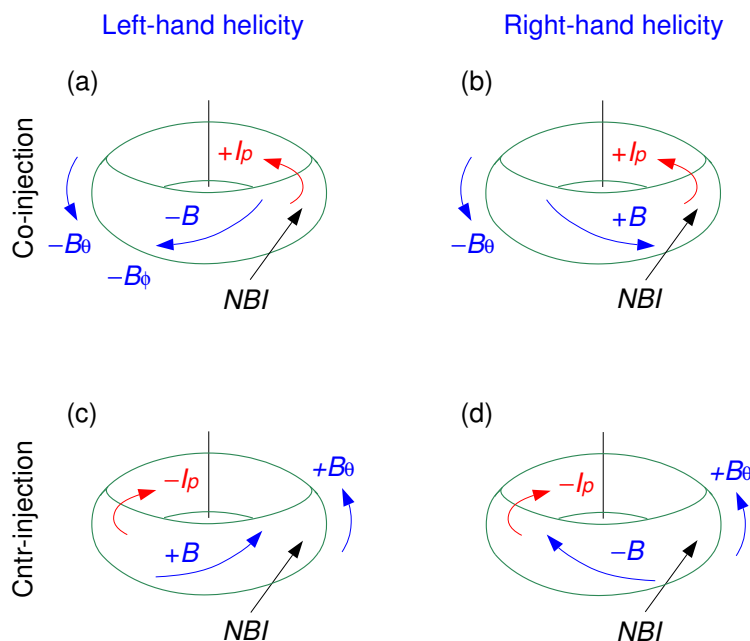


Figure 2.5: The four possible combinations of plasma toroidal field and poloidal current.

First, the two NBI injector boxes are fixed with a predominant counter clockwise toroidal injection angle. For  $+I_p$ , the toroidally induced rotation from the NBI beams is with the current (called co-injection). For  $-I_p$ , the beams are counter-injecting. When the NBI is counter-current injected, high first orbit losses are observed. In this case, the ion gyro-orbits are shifted inwards in the plasma (due to the gradient in the magnetic field  $B$  which is stronger in the plasma core than at the edge), resulting in the ion  $\mathbf{B} \times \nabla B$  drift pointing upwards. On the other hand, in an NBI co-injected plasma, the ion gyro-orbits are shifted outwards from the plasma, leading to the ion  $\mathbf{B} \times \nabla B$  drift pointing downwards. Physical sputtering, high localized thermal loads and less efficient plasma heating are all consequences of the first orbit losses detected in counter-current NBI injected discharges.

The other determining factor is the sign of the toroidal magnetic field since it determines the magnetic field line helicity. The lower divertor on ASDEX Upgrade is specially designed for discharges with a left-handed magnetic field line helicity. In this case, the magnetic field lines strike the tilted divertor tiles with a small incident angle, thereby avoiding strong local heat loading. In contrast, for discharges with right handed field line helicity, such as in  $-B_\phi, -I_p$  (figure 2.5d) and  $+B_\phi, +I_p$  (figure 2.5b) configurations, the magnetic field lines strike the divertor tiles, particularly the edges, with near perpendicular angles, causing strong local heat fluxes there.

Nevertheless, ASDEX Upgrade is still able to perform both right-handed helical configurations with the use of USN shaped plasmas. This is because the upper divertor target tiles are non-tilted so that the magnetic field line inclination angle on the targets is independent of the applied magnetic field line helicity. This makes the upper divertor particularly useful since all four plasma configurations may be performed in an USN discharge. However, it should be noted that less auxiliary heating may be applied to the upper divertor due to its more sensitive tungsten coating [17] and reduced power handling capabilities.

## 2.4 Plasma Scenarios

Small-scale turbulence in a confined plasma causes radial transport of particles and energy. In several plasma scenarios, a suppression in turbulence amplitude is detected in a certain plasma volume correlated with a reduction in particle and heat diffusivity. The restricted location in a plasma in which this occurs is called a transport barrier. There exist both edge and internal transport barriers and much research has been devoted to the study of such barriers. Since the results presented in this thesis are concentrated on the plasma edge, this section will describe several plasma scenarios where edge transport barriers have been observed.

### 2.4.1 Low Confinement versus High Confinement Discharges

The Low to High confinement mode (L-H) transition is one of the most famous bifurcation phenomena in confined plasmas. Under the constant supply of energy, the density and temperature profiles change dramatically at the transition. Figure 2.6 shows the time evolution of typical plasma parameters during an L-H transition. The discharge begins with pure ohmic heating from the induced  $I_p$ . At 1.9s, additional heating in the form of 2.1MW of NBI is applied. The plasma electron density and temperature rise but the overall confinement of the plasma is poor. This is called the low-confinement mode (L-mode). However, if the additional heating is above some threshold, the confinement spontaneously improves by a factor of two or so. This phase is called the high-confinement mode (H-mode).

In figure 2.6, the top time trace shows the heating power while the second trace shows the  $D_\alpha$  line radiation intensity in the divertor measured by a spectrometer. The L-H transition is identified at the point when the  $D_\alpha$  line emission drops and is then followed by spikes. These spikes indicate the edge localized modes (ELMs) which are a characteristic of H-modes. ELMs are repetitive edge MHD instabilities and will be described in the next section. The third time trace shows how the core electron density (measured by the DCN interferometer) and core electron temperature (from the ECE diagnostic) rise at the L-H transition. The last time trace shows the plasma stored energy and the  $H_{98}$  scaling factor; both being indications of the plasma confinement. The H-factor is given by

$$H = \frac{\tau_E}{\tau_{E,scaling}} \quad (2.2)$$

where  $\tau_E$  is the measured energy confinement time and  $\tau_{E,scaling}$  is an energy confinement from a scaling law. In this thesis, the  $H_{98}$  factor is used for comparing confinement in the various discharges. It is calculated using the ITER scaling law [18]. The time trace shows the  $H_{98}$  factor increasing from roughly 0.6 in L-mode to 1.0 in H-mode. Similarly, the plasma stored energy also increases at the L-H transition, indicating the improvement in confinement.

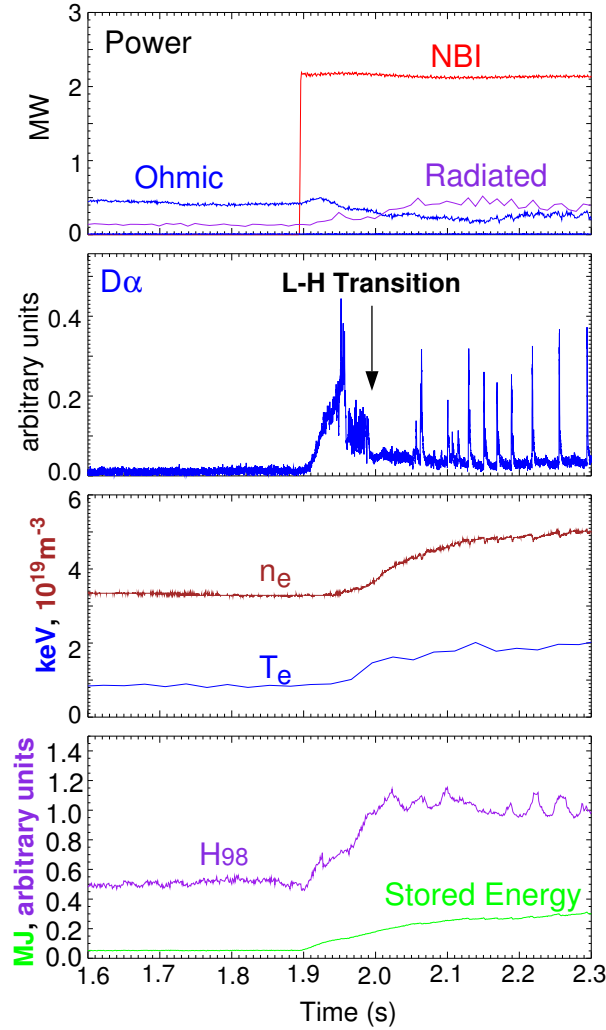
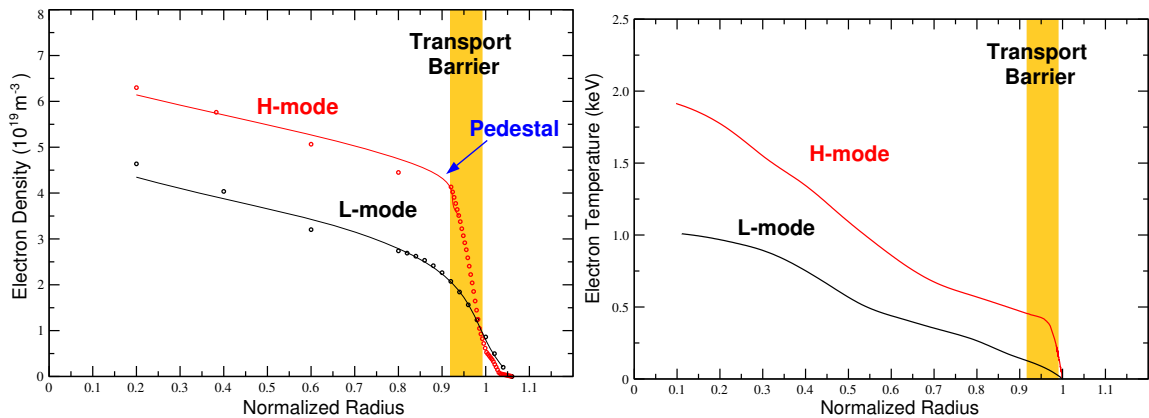


Figure 2.6: Time traces of common plasma parameters measured in discharge # 17439 during the transition from L to H-mode. The first shows the heating power, second the deuterium alpha trace, third the core electron density and temperature and lastly, the plasma stored energy and  $H_{98}$  factor.

The changes occurring in the electron density and temperature are clear in the radial profiles in figure 2.7. Here  $T_e$  and  $n_e$  are plotted versus normalized poloidal flux radius ( $\rho_{pol}$ ), which is defined by

$$\rho_{pol} = \sqrt{\frac{\Psi - \Psi_a}{\Psi_s - \Psi_a}} \quad (2.3)$$

where  $\Psi$  is the poloidal flux and the subscripts  $s$  and  $a$  denote the separatrix and the magnetic axis respectively. The normalized radius is a common choice for plotting many quantities, like pressure and density, since these quantities are constant on the poloidal flux surfaces. For such a definition, the separatrix at the last closed poloidal flux surface will always be at  $\rho_{pol} = 1$ .



(a) Electron density profiles from core Thomson scattering, profile reflectometry, DCN and CO2 diagnostics.

(b) Electron temperature profiles from Thomson scattering diagnostic.

Figure 2.7: Electron density and temperature profiles measured in the L-mode (1.9s) and H-mode (2.2s) phases in discharge # 17439. The H-mode profiles form a so called 'pedestal' at the plasma edge in H-mode.

At the L-H transition, the amplitude of the turbulence decreases abruptly at the plasma edge inside the LCFS and a spontaneous edge transport barrier is created. Its effect may be seen in Figure 2.7. In H-mode, a significant steepening of the density gradient at the plasma boundary is observed. At around  $\rho_{pol} \approx 0.9$ , the H-mode density profile rolls over, forming a knee-point in the profile known as the 'pedestal'. A similar effect is seen in the electron temperature profiles. The temperature just inside the transport barrier is significantly higher in H-mode. Inside the transport barrier, the density gradient length  $n/\nabla n$  and temperature gradient length  $T/\nabla T$  remain the same as in L-mode (called profile stiffness). Thus, the result of the H-mode pedestal is to raise the core  $n_e$  and  $T_e$  and hence the fusion performance.

#### 2.4.1.1 Edge Localized Modes (ELMs)

One side effect of the enhanced edge pressure gradients in H-mode is the formation of a relaxation MHD instability, called an edge localized mode (ELM). After the transition to H-mode, the edge density and temperature rise crossing a threshold and triggering a fast growing MHD event leading to a sudden loss of confinement at the edge with corresponding out-flux of particles and heat. Increasing recycling particle flux and increasing ionization arise in the divertor

due to the heat loss. This can be detected in the divertor as a temporal spike in the  $D_\alpha$  line radiation intensity. The sudden particle and heat loss result in a temporary flattening in the steep edge density and temperature profiles [19], reducing the  $\nabla P$  below the critical MHD threshold. After an ELM collapse, the radial heat and particle transport from within the plasma core restores the plasma pressure on a time scale of a few ms until the next ELM event occurs. This cycle may repeat itself numerous times in one plasma discharge. The positive aspect of ELMs is that undesirable impurities are ejected and stationary H-mode plasmas are achieved. The disadvantage, however, is the fast energy loss which could cause considerable damage to the divertor material. Consequently, ELMs with small losses associated with high frequency are preferred over low frequency large ELMs.

Further information on the characteristics of ELMs on ASDEX Upgrade can be found in reference [20].

### 2.4.2 Improved H-mode

In addition to the normal H-mode, there are other modes of enhanced confinement. The improved H-mode, first observed in the late nineties [21, 22], is a candidate for an *advanced tokamak* scenario. Advanced scenarios have by definition very good confinement and MHD stability properties [23]. The confinement is measured by the H-factor, where  $H_{98}$  factors greater than 1 mean an improvement with respect to standard H-modes. A measure of how efficiently the magnetic field is being used is given by normalized beta,  $\beta_N$ . It is defined by

$$\beta_N = \langle \beta \rangle \frac{aB}{I_p} \quad (2.4)$$

where  $\langle \beta \rangle$  is the volume average of the plasma over magnetic pressure ( $2\mu_0 p/B^2$ ) and  $a$  the plasma minor radius. In order for a scenario to be denoted advanced, the product  $\beta_N H$  must be higher than that of a standard H-mode. For comparison, improved H-modes on ASDEX Upgrade have factors of  $\beta_N H_{98}$  greater than 3.5 while standard H-modes have factors around 2.5. There is a limit as to how high  $\beta_N$  can be in a plasma discharge. The limitation arises from sawteeth instabilities in the plasma which trigger neoclassical tearing modes NTM (called neoclassical since it cannot be explained by classical transport theory). NTMs are responsible for reducing  $\beta_N$  and are therefore undesirable. The improved H-mode, being sawteeth free, can as such achieve a higher  $\beta_N$  limit in comparison to standard H-modes.

The improved H-mode achieves its high performance by a delicate control of the plasma current and electric field profiles in the discharge. Both edge transport barriers and internal transport barriers can appear in improved H-modes. This scenario is still in the exploratory stage.

### 2.4.3 Quiescent H-mode

Another highly confined plasma scenario was discovered on the DIII-D tokamak in 2002 [24]. It is called the quiescent H-mode (QH-mode) due to its lack of ELMs. The advantages of this scenario are clear; all the undesirable ELM effects, like erosion in the divertor, are no longer

of consequence. Quiescent H-mode discharges have also recently been obtained on ASDEX Upgrade [25, 26]. Figure 2.8 shows the time evolution of the plasma heating and  $D_\alpha$  radiation intensity of one such discharge. Note that the QH-phase between 2.0s and 3.5s is ELM-free.

One feature of the QH-mode is the occurrence of a large amplitude MHD mode located around the pedestal region, called an Edge Harmonic Oscillation (EHO). The EHO appears to replace the controlling effect of the ELMs on the edge density. In comparison with standard H-modes, higher confinement is observed in QH-modes by an increase in the H-factor. The higher confinement is detected on ASDEX Upgrade by the Doppler reflectometer. These measurements are presented in chapters 6 and 7.

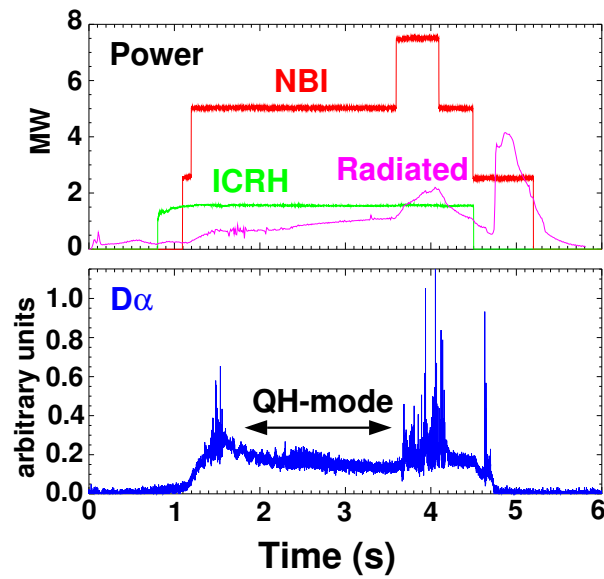


Figure 2.8: Time traces of the heating power and  $D_\alpha$  radiation measured in quiescent H-mode discharge # 16111.



# Chapter 3

## Plasma Turbulence

Doppler reflectometry is a diagnostic which provides experimental measurements of the turbulent properties of the plasma, such as the radial correlation lengths of the turbulence  $L_r$ , as well as parameters which are linked to the suppression of turbulence, like the radial electric field  $E_r$  and its associated shear  $dE_r/dr$ . This chapter reviews the present theoretical models and experimental results of plasma turbulence and the mechanisms for its suppression.

### 3.1 Anomalous Transport

Plasmas were initially thought to be quiescent so that transport would occur according to classical diffusion, where particles are lost only by Coulomb collisions with other particles. However, measured particle and energy transport in tokamaks are generally enhanced beyond the level determined by collisions. Observations show that in reality plasmas are not quiescent but rather have fluctuations in all their parameters, such as in the density  $\tilde{n}$ , temperature  $\tilde{T}$ , potential  $\tilde{\Phi}$  and the magnetic field  $\tilde{B}$ . These fluctuations, which give rise to an incoherent type of motion called turbulence, are believed to be the chief cause of *anomalous transport*. *Anomalous transport*, although not fully understood, is known to strongly affect the performance of fusion devices and is among the most important outstanding problems in plasma physics.

There are two types of fluctuations which may cause transport: electrostatic and magnetic fluctuations. In the case of electrostatic perturbations, the cross-field velocity is governed by the  $\mathbf{E} \times \mathbf{B}$  drift velocity, where the electric field  $\mathbf{E} = -\nabla\Phi$ . In the second case, when magnetic field perturbations exist, magnetic islands are formed in a plasma so that radial diffusion along a field line around the island now occurs at a much higher rate than across the field lines. The larger the islands are, the greater the resulting diffusion. Both types of turbulence have been observed on tokamaks but it is not entirely clear which of the two is responsible for transport. Section 3.2 presents the various types of turbulence present in tokamak machines. The following section 3.3 describes the experimental efforts in searching for firm proof of the connection between turbulence and *anomalous transport*. Considerable progress has also been made on the theoretical front, as high performance computing allows large scale numerical simulations of transport and strong turbulence to be performed. Some of the theoretical findings, especially

concerning the mechanism of turbulence suppression, will be presented in section 3.4. In both experiment and theory, an observed correlation between the amplitude of the turbulence and the confinement properties of the plasma offer confirmation of their relationship.

## 3.2 Properties of Plasma Turbulence

A variety of turbulence exists in a plasma due to the inhomogeneities in a plasma. Turbulence is driven by these inhomogeneities in the form of gradients. The most dominant gradients in a plasma are found in the density ( $\nabla n$ ), temperature ( $\nabla T$ ), pressure ( $\nabla P$ ) and current density ( $\nabla J$ ). Figure 3.1 illustrates the various instabilities present in the various regions of a plasma. It is evident that instabilities and their driving forces are unique in each of these plasma regimes: SOL, edge and core.

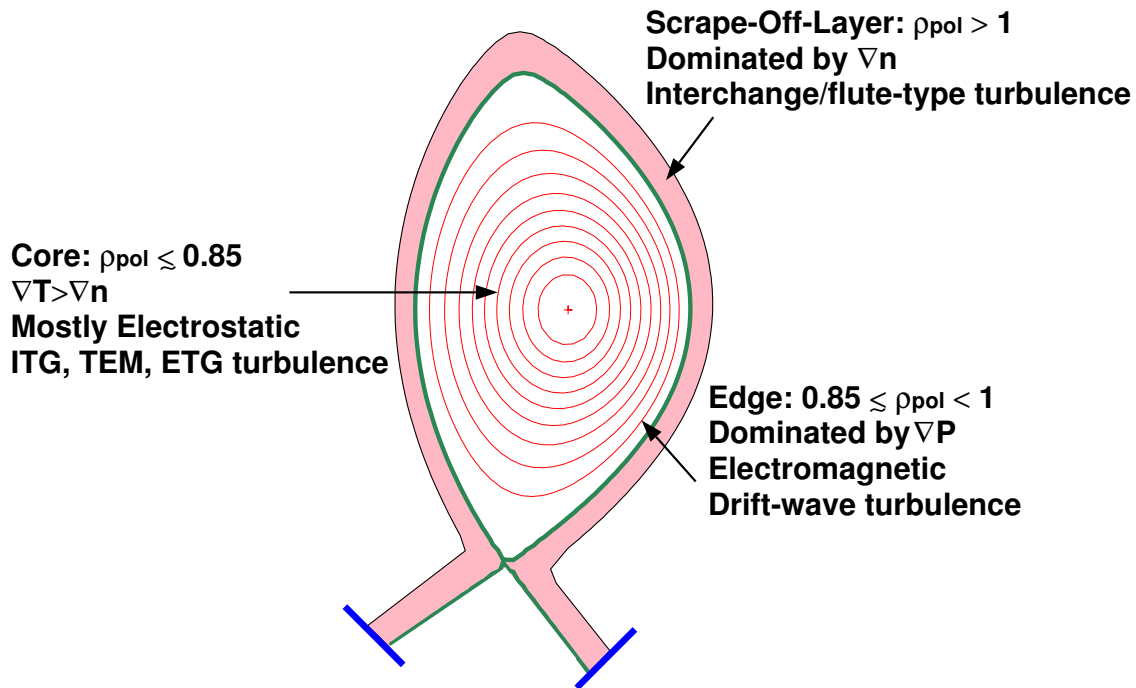


Figure 3.1: A poloidal cross-section showing the various micro-instabilities present in a tokamak plasma.

In the SOL exist mainly interchange, flute-type turbulence. Flute modes are low-frequency electrostatic oscillations stretched along the magnetic field ( $k_{\parallel} = 0$ ) and become unstable due to the combined effects of the density gradient and the magnetic field line curvature. The edge region of a plasma is mainly dominated by electromagnetic drift-wave turbulence driven by the strong pressure gradients in that region. Since the physics in the edge region of a plasma also effects the core physics, drift instabilities are considered to be the principal cause of

plasma turbulence. In the plasma core, the turbulence is mainly electrostatic. The temperature gradient becomes more significant than the density gradient, leading to ITG (ion temperature gradient) and ETG (electron temperature gradient) modes of turbulence. Trapped particle modes also exist here and in particular, TEM (trapped electron mode) turbulence is believed to play a key role. An important point to note is that several types of turbulent modes can exist simultaneously in both time and place.

The various types of turbulence may be categorized by their unique properties. They have different scale lengths; for example ITG modes have scale lengths of the ion Larmor radius (i.e. long wavelength) whereas ETG modes scale with the Larmor radius of electrons (i.e. short wavelength). The poloidal wavenumbers  $k_\theta$  for several turbulent modes are shown in figure 3.2. The figure shows typical fluctuation spectra obtained from a collective scattering experiment [27]. ITG, drift-wave and TEM modes have relatively low poloidal wavenumbers, which are generally more accessible for diagnostics. ETG, however, occurs at a much higher poloidal wavenumber ( $k_\theta > 10\text{cm}^{-1}$ ). Current efforts are being made to develop diagnostics capable of measuring high-k, short-wavelength turbulence.

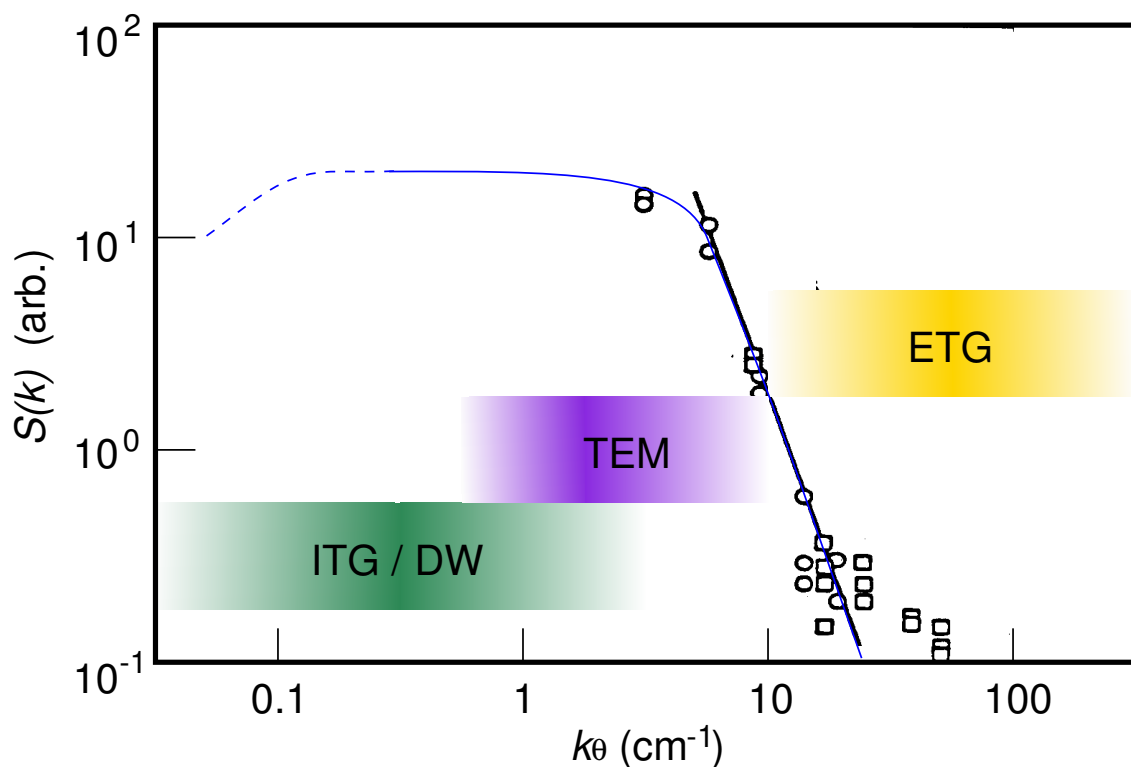


Figure 3.2: The range of poloidal wavenumbers covered by ITG, drift-waves, TEM and ETG modes of turbulence.

Another important property of the turbulence is its fluctuation amplitude level which is an indication of the turbulence strength. The parameter of particular relevance is the relative rms fluctuation level, for example  $\tilde{n}/n$ .

The turbulence also has a spatial extent, and may be thought of as eddies or blobs which travel perpendicular to the magnetic field and are either stretched in the radial or poloidal direction. As a result, radial and poloidal correlation lengths may be used to define the spatial size of a turbulent eddy.

### 3.3 Turbulence Measurements in Tokamaks

The connection between micro-instabilities and transport has been a strong motivation for the development of diagnostics to measure fluctuations in tokamaks. Below is a list of typical fluctuation diagnostics and the parameters which they measure.

Diagnostic	Type of Fluctuations
Magnetic coils & probes	magnetic
Langmuir probes	density, electric field, potential
Soft X-ray detectors	plasma emission: temperature, density, effective charge
Microwave scattering	electron density
Laser scattering	electron density
Reflectometry	electron density
Beam emission spectroscopy (BES)	electron density
Heavy ion beam probe (HIBP)	electron density, potential
Electron cyclotron emission (ECE)	electron temperature
Thomson scattering	electron temperature

Table 3.1: *The diagnostics specializing in the measurement of turbulent plasma fluctuations. Most are for plasma edge measurements due to easier accessibility.*

Fluctuation measurements tend to concentrate on the plasma edge due to easier accessibility as well as greater theoretical interest, especially after the discovery of H-mode. The fluctuations in density ( $\tilde{n}$ ), electrostatic potential ( $\tilde{\Phi}$ ), magnetic field ( $\tilde{B}$ ) and temperature ( $\tilde{T}$ ) are all relevant to confinement. Many features of the fluctuations in tokamaks are nearly universal and some will be reviewed here.

The relative amplitude of density fluctuations ( $\tilde{n}/n$ ) can be measured by Langmuir probes, BES and HIBP diagnostics, all of which can be easily calibrated. On the other hand, scattering and reflectometry systems can offer only approximate values of this measurement. In several fusion devices, the relative amplitude  $\tilde{n}/n$  was observed to increase towards the edge and peak just inside or on the LCFS. For example, in TFTR, 0.1-1% was measured in the core and 5-10% at the plasma edge [28]. In TEXT, edge  $\tilde{n}/n$  was found to be around 10-20 %, reaching up to 50 % in the SOL [29]. Similar behaviour was observed in Alcator A and Alcator C [30] and in DIII-D [31].

The magnetic, temperature and potential fluctuations are significantly more difficult to measure because of the diagnostic techniques employed. The magnetic coils used for measuring

$\tilde{B}$  are heat sensitive and thus can only be used at the plasma edge. Typical measurements of magnetic field fluctuations give  $\tilde{B}/B \approx 10^{-5} - 10^{-4}$  [32]. Similarly, the diagnostics for temperature fluctuation measurements, namely Thomson scattering and correlation ECE, have their limitations. The Thomson scattering diagnostic is spatial and/or temporal limited whereas the ECE diagnostic measures the rms value of the temperature fluctuations but not its spectrum. Furthermore, the diagnostics for potential fluctuations are expensive and the analysis is complicated. Hence, the database for density fluctuation measurements is considerably larger than all other fluctuation measurements.

Besides traditional fluctuation diagnostics, there has been effort to develop new and more diversified diagnostic techniques for other types of turbulence measurements. One such example is the correlation Doppler reflectometer, from which the radial correlation lengths of the turbulence may be obtained. This new technique has recently been applied on ASDEX Upgrade and is a major part of this thesis work. (The results may be found in chapter 8). Radial correlation lengths have also been determined on other fusion machines using different diagnostics. In TFTR, values of 2-3cm at the edge and 1-2 cm in the core were derived from BES data [33]. At JET, core radial correlation lengths in the range 2-20mm were measured by a correlation reflectometer [34]. A correlation reflectometer was also employed on DIII-D, which reported radial correlation lengths in the range 1-5mm [35]. The lower range of the JET and DIII-D radial lengths correspond to Ohmic and H-mode plasmas while the upper range was measured in L-mode plasmas. Recent measurements on DIII-D show radial correlation lengths small at the plasma edge ( $\approx 0.5$ cm) and increasing into the plasma core, up to 4cm [36]. There are however a range of methods for obtaining radial correlation lengths [37], which makes a comparison of the radial correlation length measurements from the various machines difficult.

## 3.4 Turbulence Suppression

The confinement of a plasma is a key factor in determining the efficiency of a fusion reactor. The better the confinement, the smaller the reactor needs to be. This would reduce development costs and lead to a more economically attractive fusion reactor. Therefore, understanding the mechanisms of turbulence suppression in a plasma and discovering techniques to control turbulence are needed for developing magnetic fusion. This section examines the mechanisms of turbulence suppression in confined plasmas using existent theories and experimental results.

### 3.4.1 The Radial Electric Field

The radial electric field in a plasma is not zero as one might have expected in an electrically neutral plasma, where the average charge density is zero. By Maxwell's equations, an electric field arises as the plasma moves in a magnetic field. This non-negligible electric field creates a fluid like motion known as the  $E \times B$  drift given by

$$\mathbf{v}_{E \times B} = \frac{\mathbf{E} \times \mathbf{B}}{B^2} \quad (3.1)$$

In the past, little attention was paid to the plasma radial electric field since no major effects of  $E_r$  on plasma confinement was observed. However, when the transition from low-confinement mode (L-mode) to high-confinement mode (H-mode) was found on ASDEX in the 1980's [12], a spontaneous bifurcation of  $E_r$  was used as a theoretical model for explaining the improved confinement.

The radial electric field can be deduced from the radial force balance for any plasma species  $j$

$$E_r = -\frac{1}{n_j e_j} \frac{dp_j}{dr} + v_{\theta j} B_\phi - v_{\phi j} B_\theta \quad (3.2)$$

where  $e_j$ ,  $p_j$ ,  $n_j$ ,  $v_{\theta j}$  and  $v_{\phi j}$  are the charge, pressure, density and poloidal and toroidal velocities of species  $j$ . Equation 3.2 shows a relationship between  $E_r$  and the cross field heat and particle transport ( $\nabla p_j$ ), cross field angular momentum transport ( $v_{\phi j}$ ) and poloidal flow ( $v_{\theta j}$ ). The electric field is usually determined by spectroscopic measurement of the rotation of impurities. Using this technique on several machines such as in DIII-D [38], JFT-2M [39] and ASDEX [40], a sudden change in  $E_r$  at the plasma periphery in an L-H transition was seen. The significant change in  $E_r$  right at the L-H transition was detected before the density and temperature profiles changed, indicating that the initial change in  $E_r$  is not caused by the improved confinement [38, 41, 42]. However, the  $E_r$  may change further with the development of the profiles [38, 43, 44, 45]. This sequence is what one would expect from a model in which the change in  $E_r$  stabilizes turbulent fluctuations, which then leads to a change in the particle and heat fluxes [41].

By experimentally inducing an external radial electric field in the plasmas of CCT [46] and TEXTOR [47] fusion devices, H-modes could be triggered. These experiments, which produce H-modes by plasma biasing, have shown that after the bias is applied,  $E_r$  evolves to a certain point where bifurcation occurs and the H-mode develops. This supports the casual role of  $E_r$ . There are two important mechanisms in the formation of  $E_r$ :

- 1) Damping term which is viscosity in plasma rotations (i.e. strongly damped in the poloidal direction)
- 2) Driving force to rotate plasmas toroidally or poloidally

Of the driving force, two types are considered: one is the force due to neutral beam injection and the other is the non-ambipolar flux due to electron or ion diffusion across the magnetic field.

In tokamak fundamental transport equations, all the direct radial electric field effects cancel and only the derivatives of  $E_r$  enter into the equations [48]. Thus, it is not yet known which quantity ( $E_r$  or its first derivative  $\partial E_r / \partial r$ ) is more decisive for transport and turbulence suppression.

### 3.4.2 The Radial Electric Field Shear

There is accumulating evidence that sheared  $E \times B$  rotation is the mechanism most likely responsible for micro-turbulence suppression and confinement enhancement. The mechanism has the universality to explain the formation of edge and core transport barriers (ETBs and

ITBs) in plasmas. The  $E \times B$  flow shear reduces the plasma turbulence by nonlinear decorrelation and linear stabilization of turbulent eddies. In nonlinear turbulence decorrelation theory [8, 49], the  $E \times B$  velocity shear decorrelates the turbulent fluctuations, decreases the radial correlation lengths and fluctuation amplitudes and changes the phase between density and velocity fluctuations, thereby resulting in a reduction in radial transport. In linear stabilization theory [50, 51, 52], the velocity shear can couple unstable modes to stable modes leading to transport reduction.

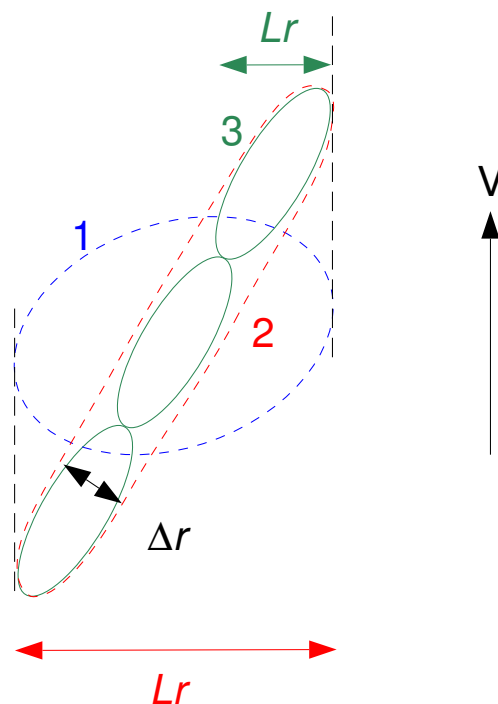


Figure 3.3: *The effect of a sheared  $v_{E \times B}$  on a turbulent eddy. The shear breaks apart the turbulent eddy, leading to smaller radial correlation lengths,  $L_r$ .*

The effect of nonlinear decorrelation is illustrated in figure 3.3. The figure shows a sketch of a turbulent eddy with a geometry labeled 1, giving a specific radial correlation length,  $L_r$ . In the presence of an  $E \times B$  velocity shear, the eddy becomes elongated (labeled 2) and eventually if the shear is strong enough, broken up (labeled 3). The resulting eddies now have smaller radial correlation lengths in comparison with the original eddy.

Figure 3.4 gives an illustration of numerical simulation of turbulence decorrelation [53]. Electromagnetic turbulence is generated by a gyrofluid model and  $E \times B$  flow shear is imposed on the turbulence. With increasing shear, the structures in ion temperature  $T_i$  are first deformed and then broken up.

Equation 3.1 shows a link between shear in the  $E \times B$  velocity and shear in the radial electric field  $\partial E_r / \partial r$ . Therefore, if the  $E \times B$  velocity shear is indeed responsible for turbulence suppression, the  $\partial E_r / \partial r$  may be considered as fundamental in quenching turbulence. This has been examined both on the experimental and theoretical front. Experiments show that at

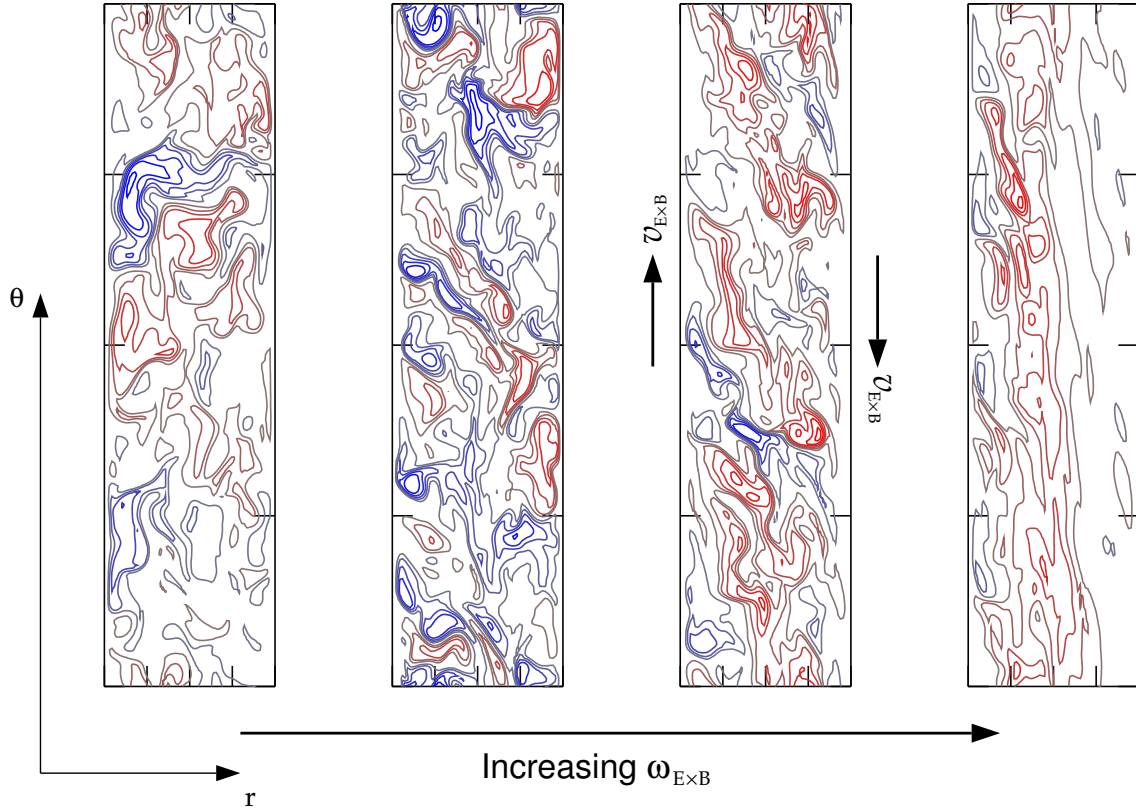


Figure 3.4: *The effect of a sheared  $v_{E \times B}$  on plasma turbulence [53]. Increasing the shear  $\omega_{E \times B}$  tears apart the turbulent eddies, leading to transport reduction.*

the L-H transition, an electric field shear develops in a localized region near the plasma edge [41, 42, 54, 55]. These experiments also show how in the same edge region, the turbulent density fluctuations decreased. There was also evidence of a coinciding decrease in particle and energy transport detected by an increase in the local gradients [39, 42, 54, 56]. Not only a spatial correlation between increased  $E_r$  shear, decreased density fluctuations and improved transport was observed, but also a temporal correlation [41].

### 3.4.2.1 BDT Model

From the theoretical point of view, the Biglari, Diamond and Terry model developed in the early 1990's has been the most oft-cited model including  $E_r$  shear effects. The BDT model shows concisely how electric field shear can nonlinearly stabilize a broad class of general, flute-like turbulent modes in the plasma. The criterion for shear decorrelation to be important is when the shearing rate exceeds the decorrelation time. This can be written as

$$\left| \frac{\nabla E_r}{B_\phi} \right| > \frac{\Delta \omega_t}{k_\theta L_r} \quad (3.3)$$

where  $B_\phi$  is the toroidal magnetic field,  $\Delta\omega_t$  is the turbulent decorrelation frequency,  $L_r$  is the radial correlation length and  $k_\theta$  is the poloidal wavenumber of the turbulence. Note how turbulence stabilization is independent of the sign of  $\nabla E_r$ .

In addition, the BDT model accounts for the different behavior at the large and small major radius sides of the plasma. Due to the tokamak's toroidal geometry, variation in  $E_r$  shear exists. This can be seen by the equation for the shearing rate given by

$$\left| \frac{\nabla E_r}{B_\phi} \right| = \frac{(RB_\theta)^2}{|B_\phi|} \left| \frac{d^2\Phi}{d\psi^2} \right| \quad (3.4)$$

where  $\Phi$  is the electrostatic potential,  $\psi$  the poloidal flux function,  $B_\theta$  the poloidal magnetic field and  $R$  the major radius. Assuming that the electrostatic potential ( $d^2\Phi/d\psi^2$ ) is constant on a flux surface, the electric field shear term varies as  $(RB_\theta)^2/B_\phi$ . This quantity is significantly smaller on the inner side of the plasma than the outer.



# Chapter 4

## Doppler Reflectometer Diagnostic

In this chapter, the theoretical foundations of microwave reflectometry will be described, with particular emphasis placed on Doppler reflectometry. Doppler reflectometry is a radar technique which uses back-scattered reflection of electromagnetic waves by a plasma cutoff to measure plasma rotation. Important aspects relevant to Doppler reflectometry such as microwave propagation and reflection in plasma will be discussed here. A description of the present Doppler reflectometer system installed on the ASDEX Upgrade Tokamak is also included.

### 4.1 Theory of Doppler Reflectometry

#### 4.1.1 Fundamental Wave Theory

Consider a simple traveling plane wave moving in the  $x$  direction and expressed by the equation:

$$A(x, t) = A_0 \exp[i(kx - \omega t)] \quad (4.1)$$

where  $A_0$  is the amplitude,  $k = 2\pi/\lambda$  is the wavenumber and  $\omega = 2\pi f$  the angular frequency of the wave. The rate of propagation of a point of constant phase on the wave is known as the phase velocity, denoted  $v_{ph}$ . The phase velocity of the wave is given by equation 4.2, which satisfies the condition  $(d/dt)(kx - \omega t) = 0$ .

$$v_{ph} = \frac{dx}{dt} = \frac{\omega}{k} \quad (4.2)$$

However, such a simple wave carries no information. In order to propagate information in a wave, a modulation in the frequency and/or amplitude of the wave is needed. This modulation forms an envelope which is known as a wave packet. A wave packet is a superposition of sinusoidal oscillations with different frequencies  $\omega$  and wavelengths  $\lambda$ . The velocity of the wave packet itself is called the group velocity and is given by equation 4.3.

$$v_{gr} = \frac{\partial \omega}{\partial k} \quad (4.3)$$

Figure 4.1 illustrates the phase and group velocity of a signal consisting of two superimposed sine waves with slightly different frequencies and wavelengths. The group and phase velocities can be quite different and should not be confused with one another. Typically, the group velocity is taken as representative of the signal's speed.

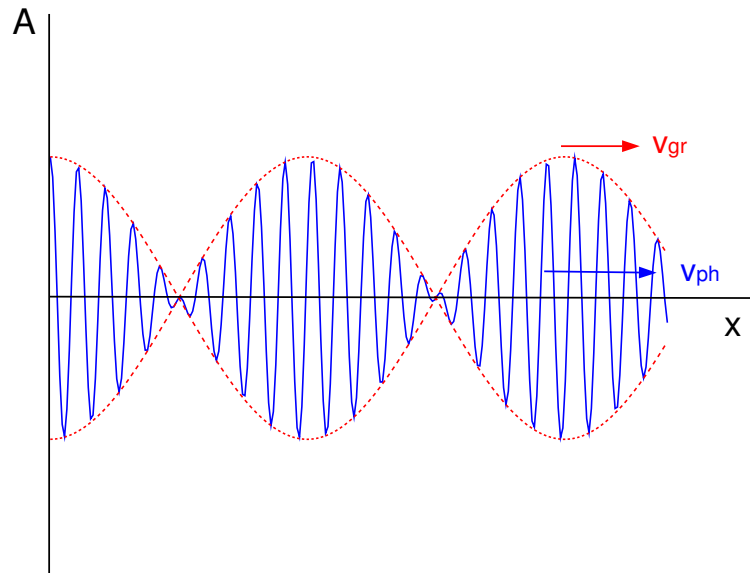


Figure 4.1: Wave packets moving at  $v_{gr}$  with wavelets moving through them at  $v_{ph}$ .

How the angular frequency  $\omega$  relates to the wave number  $k$  is known as the dispersion relation. All the information about the propagation of a wave is contained in this relation. For example, parameters such as  $v_{ph}$ ,  $v_{gr}$ , propagation region, reflection points, resonance points and wave growth or damping can be readily seen from the dispersion relation. If  $\omega(k)$  is directly proportional to  $k$  (as in the case of ion acoustic waves), then the group velocity is equal to the phase velocity. If this is not the case, the envelope of the wave will become distorted as it propagates. This phenomenon is known as dispersion and occurs when waves of different wavelengths initially move together in phase and then drift apart as the wave packet propagates, making the packet broader in both space and time.

Another important property of an electromagnetic wave, which is not contained in the dispersion relation, is its polarization. An electromagnetic wave has both an oscillating electric and magnetic component perpendicular to each other. The polarization state of the wave is defined by the orientation and phase of the E-field vector of a wave. There are three types of polarization possible: linear, circular and elliptical depending on the amplitude and phase of the wave.

### 4.1.2 Microwave Propagation in a Plasma

Microwaves are electromagnetic waves traveling at the speed of light,  $c$  with a frequency in the range of 1 to 300 GHz. Their propagation in plasma is governed by Maxwell's equations

of which the two relevant ones are given by

$$\nabla \times \mathbf{E} = -\frac{\partial \mathbf{B}}{\partial t} \quad (4.4)$$

$$c^2 \nabla \times \mathbf{B} = \frac{\mathbf{j}}{\epsilon_0} + \frac{\partial \mathbf{E}}{\partial t} \quad (4.5)$$

where  $\mathbf{E}$  is the electric field,  $\mathbf{B}$  the magnetic field,  $\mathbf{j}$  the vector current density, and  $\epsilon_0$  the permittivity of free space [57]. The time derivative of equation 4.5 is

$$c^2 \nabla \times \frac{\partial \mathbf{B}}{\partial t} = \frac{1}{\epsilon_0} \frac{\partial \mathbf{j}}{\partial t} + \frac{\partial^2 \mathbf{E}}{\partial t^2} \quad (4.6)$$

while the curl of equation 4.4 is

$$\nabla \times (\nabla \times \mathbf{E}) = \nabla(\nabla \cdot \mathbf{E}) - \nabla^2 \mathbf{E} = -\nabla \times \frac{\partial \mathbf{B}}{\partial t} \quad (4.7)$$

By assuming an electromagnetic wave of the form  $E \approx \exp[i(kr - \omega t)]$  and combining equations 4.6 and 4.7, one obtains the linear wave equation

$$\nabla(\nabla \cdot \mathbf{E}) - \nabla^2 \mathbf{E} = \frac{i\omega}{\epsilon_0 c^2} \mathbf{j} + \frac{\omega^2}{c^2} \mathbf{E} \quad (4.8)$$

Since microwaves have high frequencies, ions may be considered as fixed so that the current  $\mathbf{j}$  comes entirely from electron motions.

$$\mathbf{j} = -n_0(x) e \mathbf{v}_e \quad (4.9)$$

The electron velocity  $\mathbf{v}_e$  is derived from the equation of motion

$$\frac{\partial \mathbf{v}_e}{\partial t} = -\frac{e}{m} (\mathbf{E} + \mathbf{v}_e \times \mathbf{B}_0) \quad (4.10)$$

where  $\mathbf{B}_0$  is the magnetic field present in the plasma. White shows that the linear wave equation 4.8 may be solved for its x, y and z components [58]:

$$(k_y^2 - k_0^2 + \kappa^2) E_x + ik_y \frac{\partial E_y}{\partial x} - \frac{i\omega_c}{\omega} \kappa^2 E_y = 0 \quad (4.11)$$

$$ik_y \frac{\partial E_x}{\partial x} + \frac{i\omega_c}{\omega} \kappa^2 E_x - \frac{\partial^2 E_y}{\partial x^2} + (\kappa^2 - k_0^2) E_y = 0 \quad (4.12)$$

$$\frac{\partial^2 E_z}{\partial x^2} + k_0^2 \left( 1 - \frac{\omega_p^2}{\omega^2} - \frac{k_y^2}{k_0^2} \right) E_z = 0 \quad (4.13)$$

where

$$k_0 = \omega/c, \quad (4.14)$$

$$\kappa^2(x) = k_o^2 \frac{\omega_p^2}{\omega^2 - \omega_c^2}, \quad (4.15)$$

$$\omega_p^2 = \frac{n_o e^2}{\epsilon_o m}, \quad (4.16)$$

and

$$\omega_c = \frac{eB_o}{m}. \quad (4.17)$$

$\omega_p$  and  $\omega_c$  are defined as the plasma frequency and the electron cyclotron frequency respectively [57],[58]. Note that equations 4.11 to 4.13 are for the case when a wave enters the plasma obliquely in the plane perpendicular to  $B_o$  ( $k_z = 0$ ). This case will be further described here since it describes more accurately the situation in Doppler reflectometry where the incident microwave is purposely launched into the plasma at a non-zero tilt angle.

#### 4.1.2.1 The Ordinary Mode

Equation 4.13 is the wave equation for the ordinary mode at oblique incidence. Here, the electromagnetic wave propagates at an angle  $\theta_o$  in the x direction. The radial electric field  $\mathbf{E}$  is parallel to the magnetic field  $\mathbf{B}_o$  so that  $\mathbf{E} = E_z \hat{z}$  and  $\mathbf{B}_o = B_o \hat{z}$ . From Snell's law,  $k_y = k \sin \theta$  is constant and so  $k_y = k_o \sin \theta_o$ . Equation 4.13 can thus be written as

$$\frac{\partial^2 E_z}{\partial x^2} + k_o^2 \left( 1 - \frac{\omega_p^2}{\omega^2} - \sin^2 \theta_o \right) E_z = 0 \quad (4.18)$$

The index of refraction,  $\epsilon$ , can be seen from equation 4.18 and is expressed as

$$\epsilon = 1 - \frac{\omega_p^2}{\omega^2} - \sin^2 \theta_o \quad (4.19)$$

A cutoff occurs when  $\epsilon$  is equal to zero whereas resonance occurs when  $\epsilon$  is equal to infinity. As a wave propagates through a plasma in regions where  $\omega_p$  and  $\omega_c$  are changing, it will encounter resonances and cutoffs. Typically, a wave is reflected at a cutoff and absorbed at a resonance. Hence, setting equation 4.19 to zero and solving for  $\omega$ , one obtains the condition for cutoff in O-mode:

$$\omega = \omega_p / \cos \theta_o \quad (4.20)$$

For normal incidence, the  $\sin^2 \theta$  term in equation 4.18 vanishes and cutoff occurs at  $\omega_p = \omega$ . This means that for oblique incidence, cutoff occurs at a lower value than  $\omega_p$ .

#### 4.1.2.2 The Extraordinary Mode

For the ordinary mode, the magnetic field is neglected since the electron motion is unaffected by  $\mathbf{B}_o$ . However, when  $\mathbf{E}$  is perpendicular to  $\mathbf{B}_o$ , the electric field has both an x and y component ( $\mathbf{E} = E_x \hat{x} + E_y \hat{y}$ ). As a result, the electron motion is affected by the magnetic field. A wave with  $\mathbf{E} \perp \mathbf{B}$  is an extraordinary wave and is governed by equations 4.11 and 4.12. These

equations can be solved for  $E_y$  by eliminating  $E_x$  and simplifying using a parameterization factor  $s \equiv k_{ox}$  [58].

$$\frac{d^2 E_y}{ds^2} + p(s) \frac{dE_y}{ds} + q(s) E_y = 0 \quad (4.21)$$

where

$$p(s) = \frac{d}{ds} (\omega_p)^2 \frac{\sin^2 \theta_o}{(\omega^2 - \omega_h^2) \left( \cos^2 \theta_o - \frac{\omega_p^2}{\omega^2 - \omega_c^2} \right)} \quad (4.22)$$

$$q(s) = 1 - \frac{\omega_p^2}{\omega^2} \frac{\omega^2 - \omega_p^2}{\omega^2 - \omega_h^2} - \sin^2 \theta_o - \frac{d}{ds} (\omega_p)^2 \frac{\omega_c}{\omega} \frac{\sin \theta_o \cos^2 \theta_o}{(\omega^2 - \omega_h^2) \left( \cos^2 \theta_o - \frac{\omega_p^2}{\omega^2 - \omega_c^2} \right)} \quad (4.23)$$

The index of refraction is now

$$\varepsilon = 1 - \frac{\omega_p^2}{\omega^2} \frac{\omega^2 - \omega_p^2}{\omega^2 - \omega_h^2} - \sin^2 \theta_o \quad (4.24)$$

Setting equation 4.24 to zero, one obtains two solutions for cutoff in X-mode

$$\omega_R = \frac{1}{2} \left[ \omega_c + \left( \omega_c^2 + 4 \frac{\omega_p^2}{\cos \theta} \right)^{1/2} \right] \quad (4.25)$$

$$\omega_L = \frac{1}{2} \left[ -\omega_c + \left( \omega_c^2 + 4 \frac{\omega_p^2}{\cos \theta} \right)^{1/2} \right] \quad (4.26)$$

The cutoff frequencies  $\omega_R$  and  $\omega_L$  are known as the right-hand and left-hand cutoffs respectively. Note that  $\omega_R$  is greater or equal to the plasma frequency,  $\omega_p$ . Thus, cutoff occurs at a lower density in the extraordinary mode. As a result, the extraordinary mode is generally used for studying the low density plasma edge.

### 4.1.3 Principle of Doppler Reflectometry

Although only recently used to diagnose tokamak plasmas, Doppler reflectometry techniques have already been applied for many years in other fields. For example, radar experiments with tilted antennas have been made in the ionosphere for measuring the properties of electron density fluctuations [59].

The principle of Doppler reflectometry can be most simply explained by considering a reflection grating containing a small sinusoidal corrugation and moving in vacuum [10]. This grating can be assumed as a simple model of the density perturbations in the plasma with wavenumber  $k_{\perp}$ . In Doppler reflectometry, a microwave beam is launched from a transmitting antenna into the plasma at a finite tilt angle  $\theta_{ilt}$  with respect to the normal to the cutoff surface, see figure 4.2. The incident beam is both reflected and Bragg scattered at a cutoff layer in the plasma. The position of the cutoff (i.e. point of reflection in the plasma) has already been described

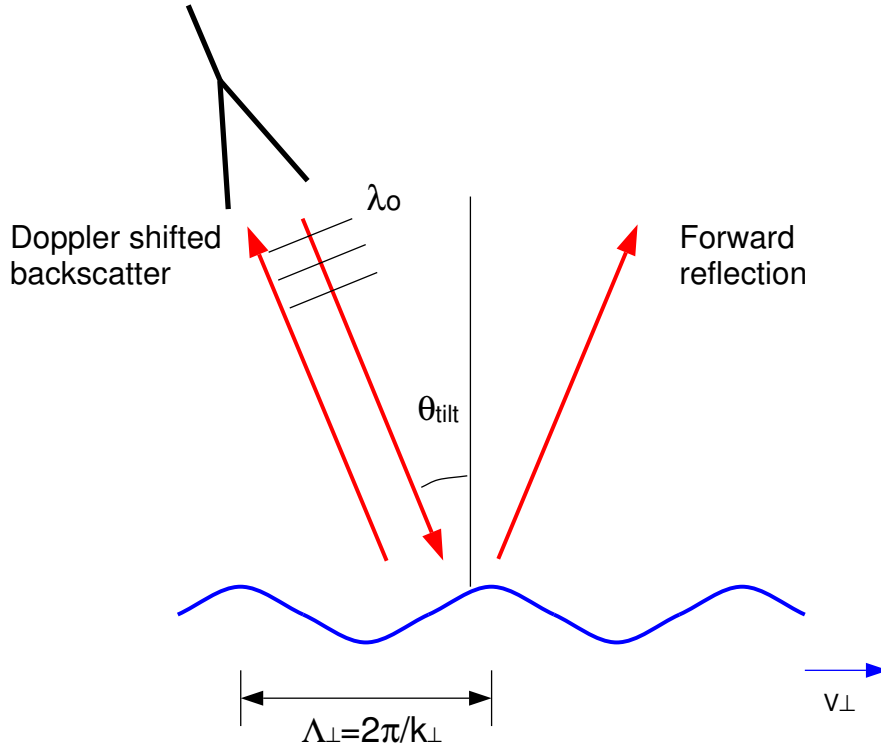


Figure 4.2: The principle of Doppler reflectometry. A monostatic antenna system is assumed and density fluctuations in the plasma are thought of as sinusoidal perturbations.

in the previous section for both O-mode and X-mode propagation of the microwave beam. The backscattered reflected signal is then detected by a nearby antenna or in the case of a monostatic system, the same launching antenna. Assuming a monostatic system (the receiving antenna is anyways generally placed very close by to the transmitting antenna), the geometry selects the diffraction pattern of order  $m = -1$ . As a result, the Bragg diffraction equation gives the condition

$$k_{\perp} = 2k_0 \sin \theta_{\text{tilt}} \quad (4.27)$$

where  $k_0 = 2\pi/\lambda_0$  is the probing wavenumber. Equation 4.27 shows that by varying the tilt angle, the Doppler reflectometer selects plasma density perturbations with finite wavenumber  $k_{\perp}$  in the cutoff layer by the Bragg condition. Therefore, the diagnostic provides access to the  $k$  spectrum of the turbulence. This is different from *conventional* reflectometry that launches microwaves normal to the cutoff layer surface (i.e.  $\theta_{\text{tilt}} = 0$ ) thereby receiving only the  $m = 0$  order signal.

If the reflection grating (i.e. fluctuating plasma) moves with velocity  $u_{\perp}$ , a Doppler shift  $\omega_D$  is detected in the received microwave signal [9, 10]. It is given by

$$\omega_D = \vec{u} \cdot \vec{k} \quad (4.28)$$

For density fluctuations in tokamak plasmas, the wavenumber of the turbulence  $k$  is assumed

to be perpendicular to the magnetic field  $B$  (i.e.  $k_{\perp}$  dominates over  $k_{\parallel}$ , see section 3.2). Thus, the Doppler shift results only from the velocity component of the perturbations *perpendicular* to the magnetic field. Equation 4.29 gives the Doppler shifted frequency determined from the combination of equations 4.27 and 4.28.

$$f_D = u_{\perp} \left( \frac{2}{\lambda_0} \right) \sin \theta_{\text{tilt}} \quad (4.29)$$

#### 4.1.4 Reflectometer Signals : Homodyne versus Heterodyne Detection

Reflectometers consist of a microwave source, transmission lines and a detection system. The circuit shown in figure 4.3 shows the simplest reflectometer circuit. The microwave source used is typically a solid state oscillator (i.e. Gunn diode) with a frequency range dependent on the applied voltage and semiconductor structure. Transmission lines are generally low-loss oversized waveguides since the microwave source and detection system are usually located at a great distance from the plasma. In figure 4.3, a wave with constant amplitude and angular frequency  $\omega_0$  is launched into the plasma and reflected back as well as scattered. The signal received by the antenna is:  $s(t) = A(t) \cos[\omega_0 t + \phi(t)]$  where the amplitude  $A$  and phase  $\phi$  vary slowly with time compared to  $1/\omega_0$ . The frequency  $\Delta\omega = d\phi(t)/dt$  can be interpreted as the instantaneous Doppler shift of the received wave [60]. Both  $A$  and  $\phi$  contain a stochastic component that carries information on the statistical properties of the density fluctuations present in the plasma. The signal  $s$  is then mixed with  $\omega_0$  and finally low pass filtered.

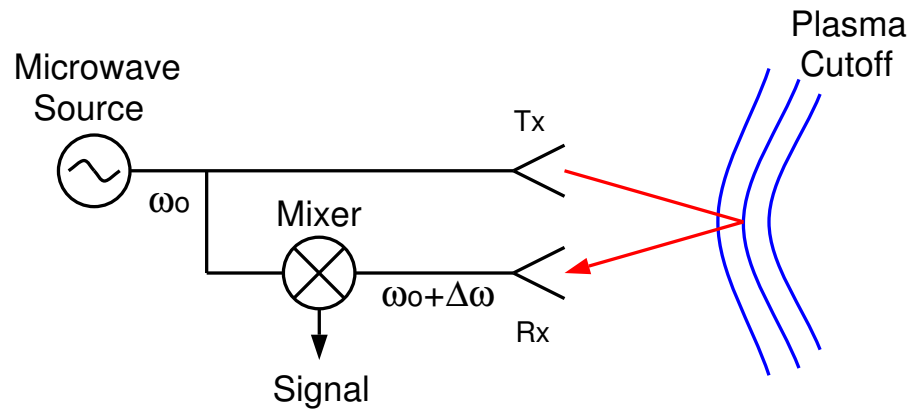


Figure 4.3: Circuit diagram of a homodyne reflectometer.

The advantage of such a homodyne detection system is that it is simple and cheap but it also has several drawbacks. Since the received signal is mixed with the same reference frequency  $\omega_0$ , the down-converted output is at zero frequency. As a result, the system has poor sensitivity as the mixer has an inherent  $1/f$  noise. A further disadvantage of the system is a loss in the sign of  $\Delta\omega$ . In order to recover such information, a heterodyne detection system, as shown in figure 4.4, is needed.

In heterodyne detection, a local oscillator (LO) is used with a different frequency ( $\omega_1$ ) for down-shifting the frequencies of the received and reference signals. Hence, the mixer output is no longer at zero frequency and the sensitivity and dynamic range of the detection system improve. Not shown in figure 4.4 is a Phase Locked Loop (PLL) system containing a stable crystal controlled oscillator. This oscillator helps to remove frequency jitters and drifts in the microwave source and to keep the reference frequency  $|\omega_o - \omega_1|$  constant.

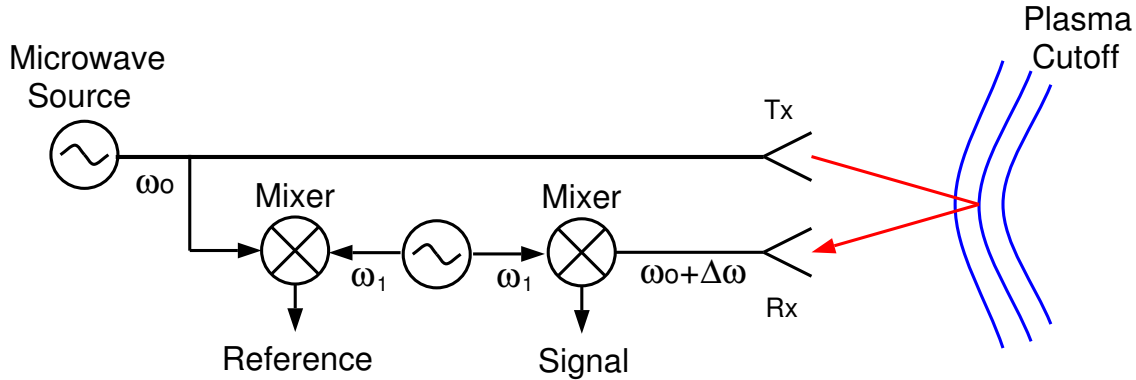


Figure 4.4: Circuit diagram of a heterodyne reflectometer.

Heterodyne detection is subject to fluctuations in the amplitude and phase. For full information on the spectral characteristics of the received signals, quadrature detection is required. The reference and received signals enter a so called IQ detector, illustrated in figure 4.5.

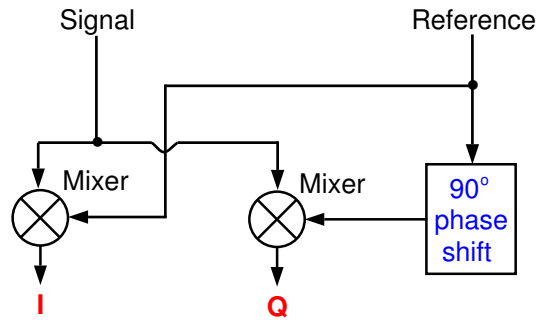


Figure 4.5: Circuit diagram of an IQ detector.

The IQ detector mixes the reference signal with the received signal to obtain the In-phase signal ( $I$ ) where

$$I = A \cos \phi \quad (4.30)$$

By shifting the reference signal by  $90^\circ$  and mixing it with the received signal, the Quadrature signal ( $Q$ ) can also be provided by the IQ detector. It is defined as

$$Q = A \sin \phi \quad (4.31)$$

From equations 4.30 and 4.31, it is evident that a heterodyne detection system can provide both  $I$  and  $Q$  signals as well as amplitude  $A = (I^2 + Q^2)^{1/2}$  and phase  $\phi = \arctan(Q/I)$  information. So although it is more complex and expensive than homodyne detection, heterodyne detection is often used because of its capability to provide the sign of the phase variations.

## 4.2 Doppler Reflectometer Diagnostic in ASDEX Upgrade

The earlier sections of this chapter covered the fundamental theory of Doppler reflectometry. The focus of this section will now be the Doppler reflectometry hardware and data acquisition system used for obtaining the experimental measurements presented in this thesis.

### 4.2.1 Hardware Components

Around 1999, a Doppler reflectometer diagnostic system was designed and built for operation on the ASDEX Upgrade tokamak as part of a PhD project [61].

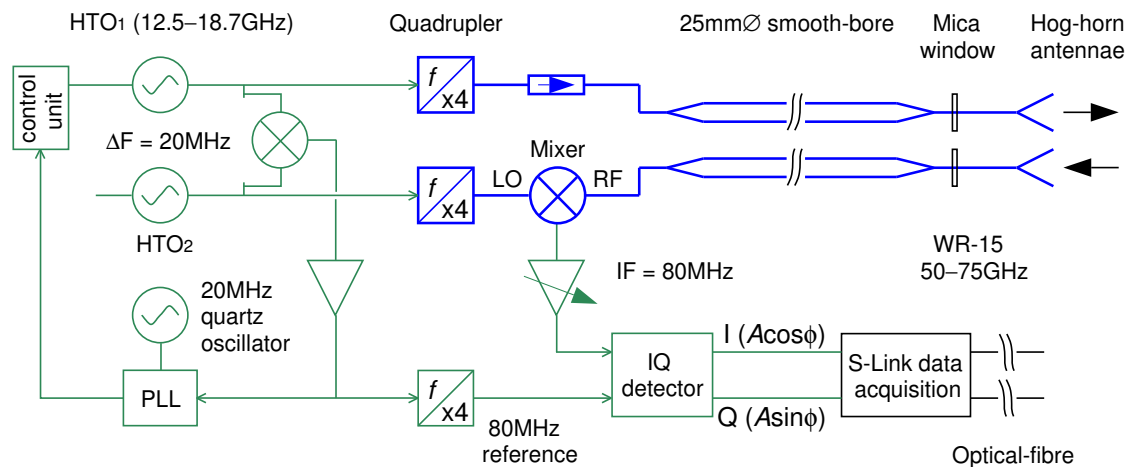


Figure 4.6: Circuit diagram of a V-band heterodyne microwave Doppler reflectometer.

The current system consists of two identical heterodyne V-band Doppler reflectometers; V-band meaning that they launch microwaves in the frequency range 50 to 75GHz. The reflectometers have steppable launch frequencies with selectable X or O-mode polarization. A schematic of the components in a V-band reflectometer is shown in figure 4.6. The circuit diagram consists of microwave and waveguide components (shown by thick lines) and radio frequency (RF) and electronic components (shown by lighter lines). The circuit shows a sender and local oscillator as being two 12.5-18.75GHz solid state hyper-abrupt varactor tuned oscillators (HTOs). The oscillators are phase locked via a PLL (Phase Locked Loop). The PLL maintains a fixed frequency difference of 20MHz between the two HTO frequencies. It ensures a stable signal by requiring that the two HTO frequencies remain in synchronisation. The frequencies of the HTOs are then brought to the V-Band range (50 to 75GHz) with the

use of active frequency quadruplers. Approximately 10mW of microwave power is launched from the V-band reflectometer. The received signal is then down-converted to an intermediate frequency (IF) of 80MHz with the use of a waveguide mixer followed by In-phase and Quadrature (IQ) detection. The IQ detector outputs the I and Q signals, which are respectively the real and imaginary part of the complex signal.

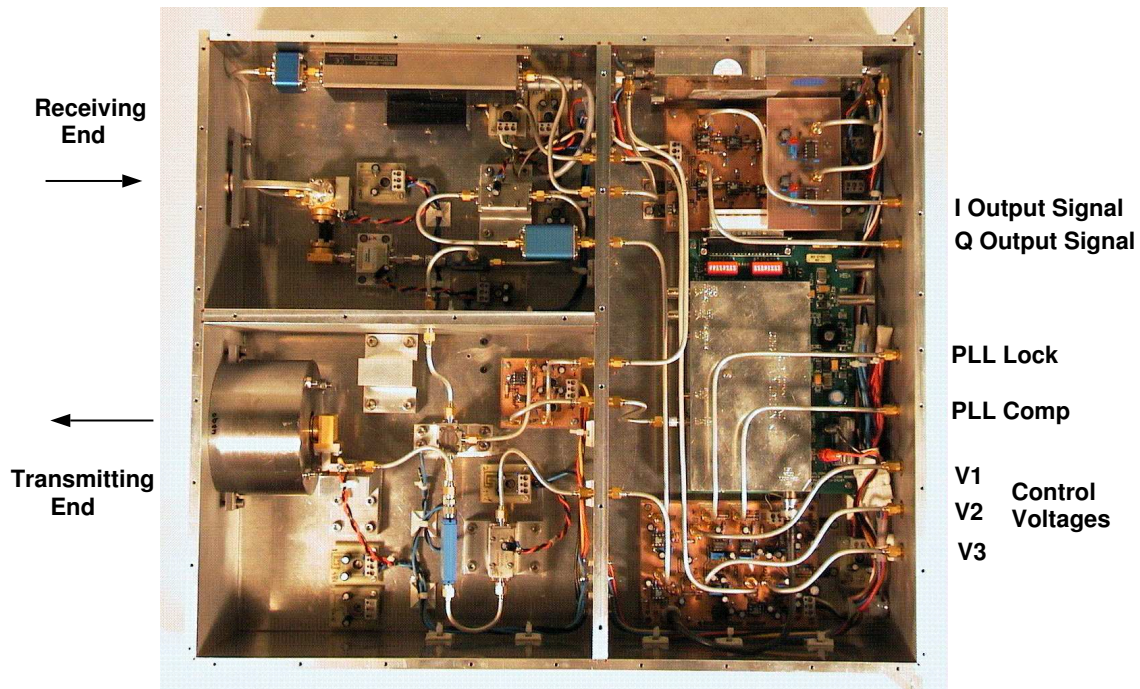


Figure 4.7: Picture of the microwave components in a V-band heterodyne microwave Doppler reflectometer. Note the microwave transmitting and receiving parts are separated.

Figure 4.7 presents a photograph of one of the V-band Doppler reflectometers. Note how the microwave transmitting and receiving parts are separated. This is to prevent interference between the microwave signals. Each of the three separated sections of the reflectometer have their own power and ground connections. Also visible in the photograph are the V1, V2, V3 control voltage inputs along with the I and Q reflectometer signal outputs.

There are currently two sets of antenna pairs used; one for O-mode and one for X-mode polarization. A pair is needed since one is the launch and the other the receive antenna. The antennae are connected to the reflectometer channels with the use of two different types of waveguide transmission lines. 25mm diameter smooth bore oversized circular waveguide transmission lines are used to carry the microwave signals from the reflectometer channels positioned outside the tokamak vessel (about 3m above the plasma edge) to the tokamak port. Due to limitations in space, a series of mitre bends in the transmission lines are needed. Mitre bends unfortunately increase the signal loss, although normally they are efficient in changing the direction of the microwave power. Shortly before the tokamak port (i.e. vacuum window), the transmission lines convert from circular to fundamental WR-15 rectangular waveguide,

again to minimize the space required. (Note that the Doppler reflectometer system has to share its port with several other diagnostics). The rectangular waveguide transmission lines continue in-vessel to the antennae after passing through the vacuum window which is a  $25\mu\text{m}$  thick mica sheet sandwiched between o-ring sealed waveguide flanges. Mica sheets are chemically inert, dielectric, flexible and insulating. They are optimal for vacuum windows since they are stable when exposed to electricity, moisture, light and extreme temperatures.

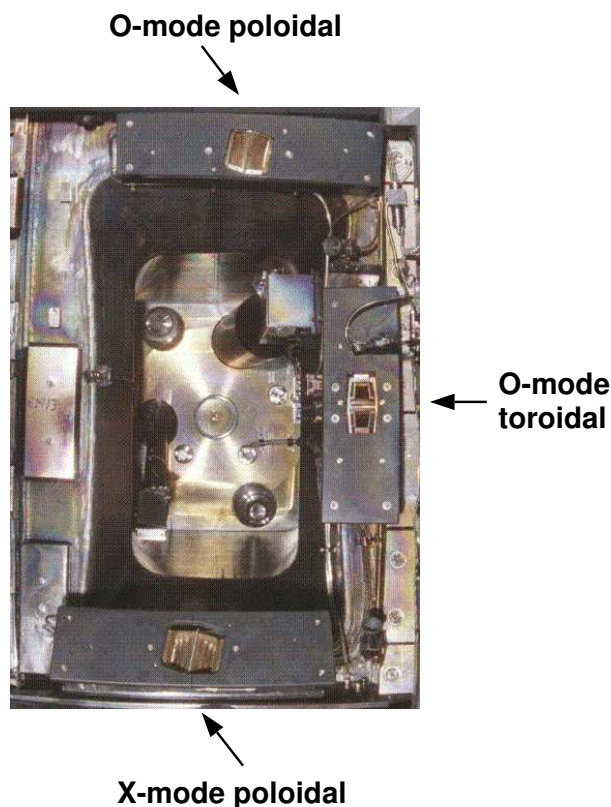


Figure 4.8: A photograph of sector 13 of ASDEX Upgrade showing the O-mode and X-mode antenna pairs.

i.e. the receive and transmitting antennae may be treated as one. The resolution of the diffraction orders depends on the width of the spectral peaks which scale directly with the wavenumber sensitivity of the diagnostic, which in turn depends inversely on the antenna spot radius. The spot sizes of the antennae are usually 2cm or more.

For more detailed information on the hardware system and its development, the reader is referred to reference [61].

### 4.2.2 Data Control and Acquisition

The components in the Doppler V-band reflectometers function on analog control. The reflectometers require an analog control voltage and output analog I and Q signals. The measured

The antennae pairs are situated in sector 13 of the ASDEX Upgrade tokamak and can be seen in figure 4.8. They are positioned on the low field side with deliberate fixed tilt angles, primarily in the poloidal direction. The O-mode pair of antennae is situated above the plasma magnetic axis and points downwards ( $\theta = -31^\circ$ ) whereas the X-mode pair is below the magnetic axis and points upwards ( $\theta = +42.5^\circ$ ). In order that the antennae tilt angles are in the perpendicular direction, the antennae are skewed  $10^\circ$  in the toroidal direction to roughly align with the magnetic field line inclination at the plasma edge. The antennae fixed tilt angles are optimized for separating out the  $m = -1$  Doppler peak from the  $m = 0$  direct reflected peak.

Figure 4.9 shows a sketch of the O-mode antenna pair and its orientation. It consists of back to back pyramidal hog-horns with elliptic focusing mirrors. The geometry was designed at the University of Stuttgart to ensure maximum antenna pattern overlap [61]. The system may be considered monostatic;

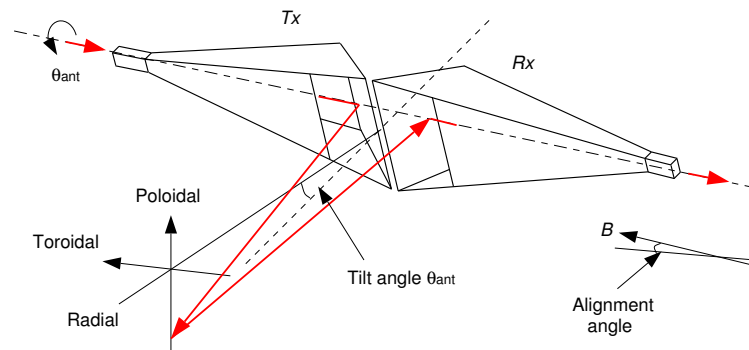


Figure 4.9: Schematic of O-mode hog-horn antenna pair.

I and Q signals are first analog filtered at 7 MHz to prevent aliasing and then digitized by an analog/digital (ADC) converter in the control unit. The control unit is also responsible for converting the control voltages for the reflectometers from digital to analog (DAC). The choice of a particular ADC and DAC is typically dependent on cost, accuracy, speed and the number of bits (dynamic range). The dynamic range of the Doppler system depends on the IF gain, which lies in the range of 20 to 50 dB. As a result, the typical signal to noise ratio is better than 40 dB.

A 12 bit S-LINK data acquisition system [62] with an MDSplus server/client interface is used for data acquisition. The S-LINK system collects data at a rate of 20 MHz for up to 7 to 10 seconds. (Discharges on ASDEX Upgrade last up to a maximum of 10 seconds.)

Further details on the data control and acquisition system may be found in reference [61].

### 4.3 Development of a new Correlation Doppler Reflectometer System

For this study, two identical V-Band reflectometer channels are connected to the same antenna pair by a combination of waveguide switches and directional couplers such that the reflectometers can be run either both in O or both in X mode configuration. This system launches two microwave beams simultaneously into the plasma from the same tilted hog-horn antenna, thereby making correlation measurements possible. A sketch of the correlation system can be seen in figure 4.10. A waveguide switch is a device for sending energy into one of two or more channels [63]. The switches used here are rotating tap switches operated by mechanical means. The switch contains a waveguide with a bend whereby on rotating the switch, successive arms may be connected (see figure 4.11). The switches are used to direct the microwave power to either the O-mode or X-mode antenna pairs. The correlation Doppler reflectometer system was commissioned and operated on the ASDEX Upgrade tokamak as part of this thesis work.

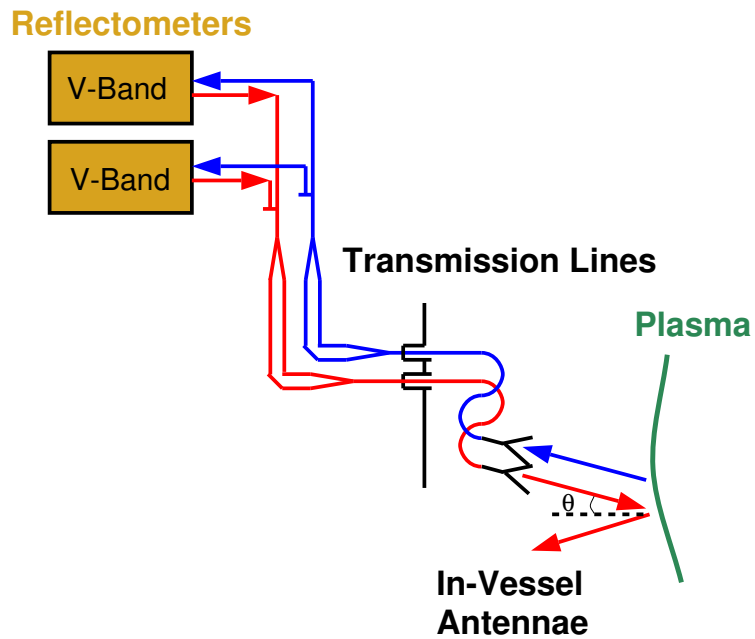


Figure 4.10: Sketch of the correlation Doppler reflectometer system. The red lines indicate the transmitting path while the blue indicate the receiving path. The microwave is launched at a finite tilt angle  $\theta$  with respect to the normal to the plasma cutoff surface.

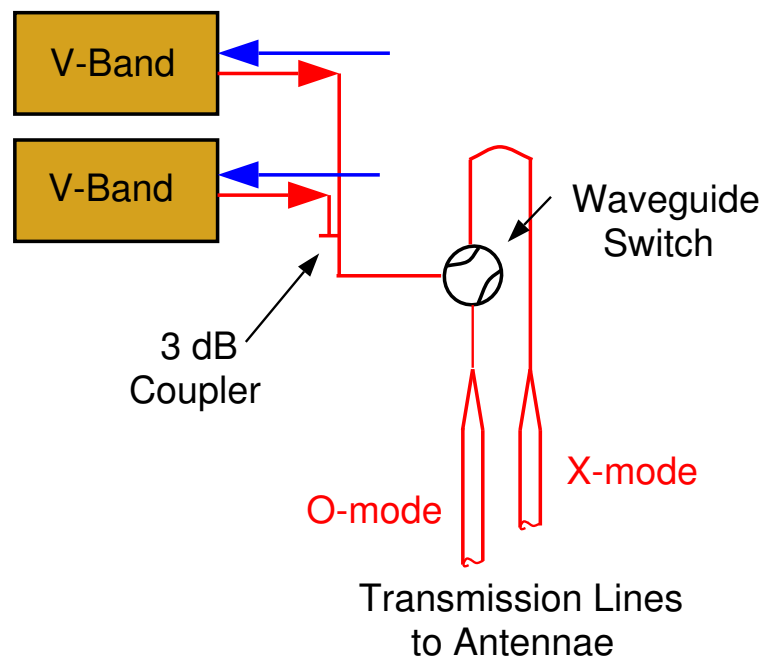


Figure 4.11: Close-up view of the waveguide switch and 3dB coupler used for connecting two V-band reflectometers to the same antenna pair. There is also a waveguide switch and 3dB coupler on the receiving end of the reflectometers which is not shown.



# Chapter 5

## Measurement Technique & Data Analysis

Since the use of Doppler techniques in fusion-oriented plasmas is new (the first Doppler reflectometer to be used for experimental tokamak studies was designed in 1999), the measurement capabilities of such a system are relatively unknown territory. This chapter will describe the possible measurements with such a Doppler system derived from theory. These measurements include the perpendicular rotation ( $u_{\perp}$ ) of the turbulence, the radial electric field ( $E_r$ ) and its associated shear ( $dE_r/dr$ ), and the radial correlation lengths of the turbulence ( $L_r$ ). From equation 4.29, three parameters are seen as essential for evaluating Doppler reflectometry data. These are: the wavenumber of the probing microwave ( $k_o$ ), the geometric tilt angle between the plasma flux surface normal and the incident microwave beam ( $\theta_{tilt}$ ) and the Doppler shift in the received signal ( $f_D$ ). A fourth parameter, namely the radial position of reflection in the plasma ( $r$ ), is also very important since it determines the positions in the plasma where the Doppler measurements have been made. Section 5.1 describes how experimental plasma cutoff layers are determined in order to obtain the radial position of the Doppler measurement and the geometric tilt angle of the incident microwave beam. Then, the method of obtaining the Doppler frequency shift and some of its challenges, particularly caused by ELMs, are explained in section 5.2. In sections 5.3 and 5.4, the possible measurements with a single-channel and dual-channel (i.e. correlation) Doppler reflectometer are discussed along with the technique and data analysis methods used. The following chapters will present the experimental results.

### 5.1 Reflection Cutoff Layers

As previously mentioned, an essential parameter in evaluating Doppler reflectometry data is the position of reflection (i.e. cutoff layer) in the plasma. The point of reflection provides the location where the Doppler measurement has been made. This is of key importance in the evaluation of Doppler data, in particular when interested in radial profiles (i.e. Doppler data as a function of plasma radius). Generally, the radial cutoff layer positions are evaluated from the density profile (when using O- or X-mode polarization) and the magnetic field profile (when using X-mode polarization). [See equations 4.20, 4.25 and 4.26]. The magnetic field

$B$  is provided from reconstruction of the magnetic equilibrium, in this case using function parameterization based on magnetic coil measurements outside the plasma [64] whereas the  $n_e$  profile is provided by other diagnostics as described below.

### 5.1.1 Electron Density Profiles

Several diagnostics currently exist on ASDEX Upgrade for measuring plasma electron density profiles. While some are specially designed for edge measurements, others measure far into the core. Since no diagnostic alone can give full reliable coverage of the plasma, a combination of all available density diagnostics is used to obtain the best possible density profile at a certain time in the discharge. Table 5.1 lists the diagnostics on ASDEX Upgrade used for electron density measurements.

Density Diagnostic	Plasma Coverage
CO <sub>2</sub>	core and edge (line integrated)
DCN	core and edge (line integrated)
Lithium Beam	edge
Thomson Scattering	core or edge
Reflectometry	edge

Table 5.1: *Various density diagnostics and their plasma coverage on ASDEX Upgrade.*

Each of these diagnostics are briefly described in turn.

1-2) The CO<sub>2</sub> and DCN diagnostics take advantage of a widely used laser interferometry technique. At ASDEX Upgrade, a Mach Zehnder interferometer is used along with a DCN laser to measure the line integrated electron densities along five lines of sight (three being horizontal and the other two at an angle). The CO<sub>2</sub> system uses rather a shorter wavelength CO<sub>2</sub> laser and measures the density line integrals along three vertical lines of sight. In order to obtain density profiles from these diagnostics, the line integrated data requires deconvolution algorithms. Although the line integrals are very accurate, they provide too little information, especially at the plasma edge where gradients are steep. Smoothing the profiles at the edge result in poor density profiles and hence, these diagnostics are generally used only as an additional consistency check of the overall density profile.

3) The lithium beam diagnostic is based on lithium beam impact excitation spectroscopy (Li-IXS) [65]. In this technique, neutral lithium atoms are injected into the plasma with an energy of 15-100keV and emitted Li I radiation is observed. The light emission profiles are then modeled with a set of coupled linear differential equations to obtain the electron density profile at the plasma edge.

4) The Thomson scattering diagnostics are based on scattering of light introduced from lasers penetrating in the plasma. The scattered power is directly proportional to the electron density and hence, the electron density may be obtained at each location where the laser light is scattered. The Thomson system on ASDEX Upgrade has undergone several upgrades during

the years [66]. The main used Thomson system is known as the Vertical Thomson Scattering VTS system, named after the direction of its lasers. The VTS system can provide both core and edge measurements, although not simultaneously due to the rearrangement of the lasers necessary.

5) In *conventional* reflectometry, a microwave beam is launched into the plasma with near perpendicular wave incidence and is reflected at a cutoff [67]. The probing frequency determines the electron density at the cutoff layer while the cutoff position is determined from the phase difference between the signal reflected from the plasma and the incident signal.

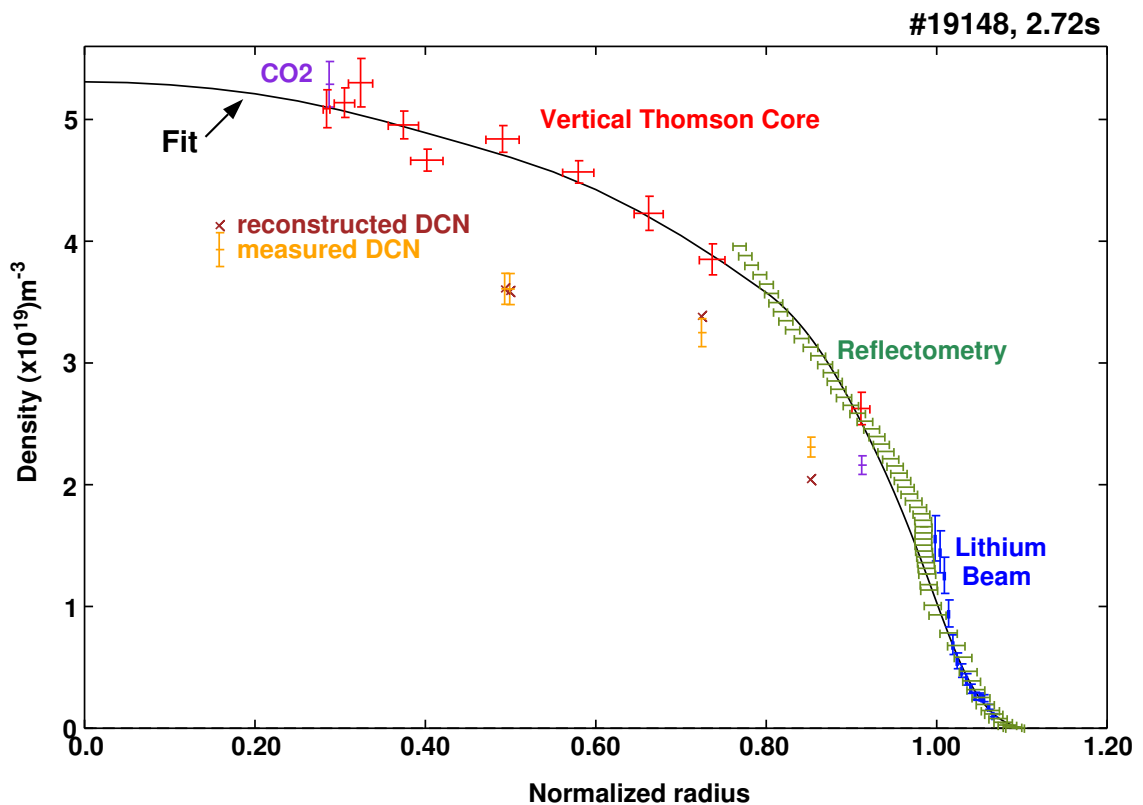


Figure 5.1: The density profile for discharge #19148 during the L-mode phase at 2.72s.

An example density profile obtained from a combination of these diagnostics can be seen in figure 5.1. The profile is measured during the L-mode phase of an Upper Single Null discharge. Typically, densities for ASDEX Upgrade discharges range between  $3$  to  $10 \times 10^{19} m^{-3}$ . A fitting program exists, which reads in all available experimental density data and performs an iterative fit to the data. The fit assumes constant density on the plasma flux surfaces and tries to minimize the curvature of the profile under the constraint of the measured densities and their errors. The fit is shown as a solid curve in figure 5.1 and is plotted versus the normalized radius ( $\rho_{pol}$ ). Note the good agreement between lithium beam and reflectometry at the plasma edge. For accurate edge measurements, lithium beam and Thomson scattering edge data is generally used. On the other hand, for core measurements, the Thomson scattering core data

is preferred. Also shown in figure 5.1 are the measured and reconstructed line integrals of the DCN and  $\text{CO}_2$  interferometer over the normalized radius of the flux surface which tangents the interferometer line of sight. Since these are line integrals, the points do not lie on the curve of the density profile, but nevertheless, it can be seen that the fitted profile also reconstructs the line integrals quite well.

### 5.1.2 Poloidal Cross Sections of the Radial Cutoff Layers

From the density profile and the magnetic field of a discharge, the cutoff layer positions may be determined for each microwave probing frequency by the equations for O-mode and X-mode cutoffs already given in chapter 4.

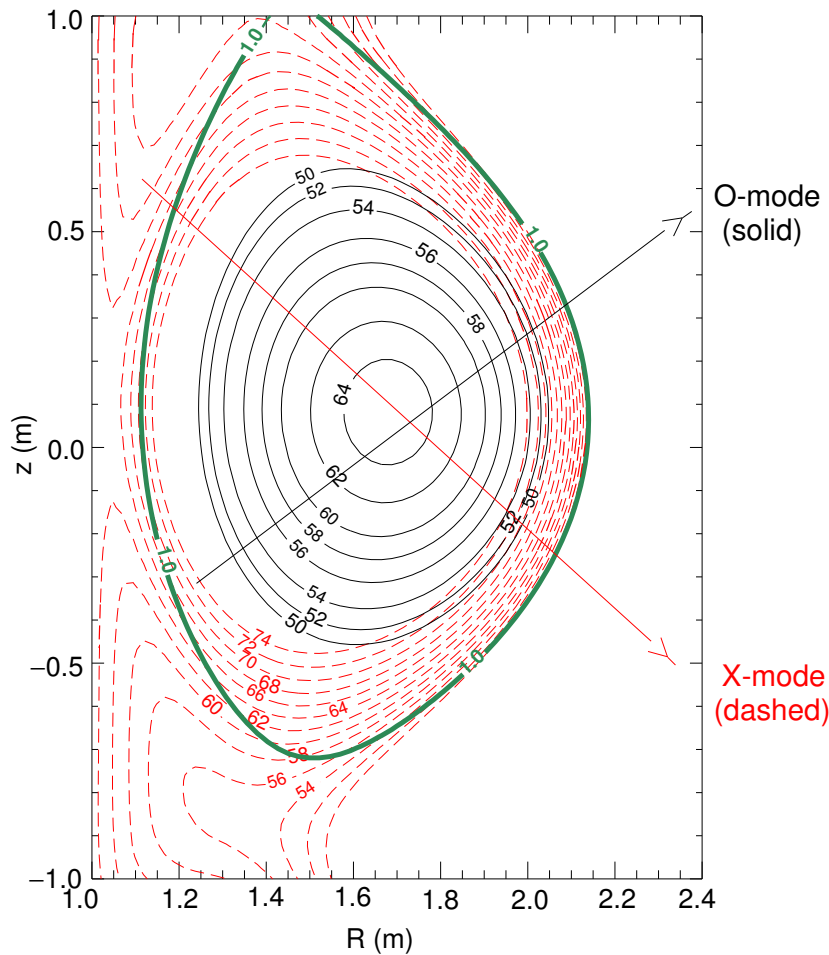


Figure 5.2: Contours of cutoff layers in the V-band frequency range (50-74GHz) for discharge #19148 at 2.72s. O-mode and X-mode antennas are shown along with their LOS in the plasma. The separatrix is marked as a solid green curve.

Figure 5.2 illustrates contours of the cutoff layers for discharge #19148 mapped onto the poloidal cross section of the plasma for several probing frequencies in the V-band range. The

density profile shown in figure 5.1 was used for these calculations. The cross section is plotted versus the major radius  $R$ . The thick solid curve outlines the separatrix at normalized radius 1.0. Here, it is evident that the plasma is in Upper Single Null configuration. Also seen in the figure is the O-mode and X-mode antennas situated relative to the plasma as well as their lines of sight (LOS) into the plasma. The dashed curves represent the cutoff layers for microwave propagation in X-mode configuration while the solid curves show the O-mode cutoff layers. The O-mode cutoff layers follow the plasma flux surfaces while the X-mode cutoffs, due to the  $B$  field dependence, do not. As quite often the case for Doppler measurements on ASDEX Upgrade (where the density ranges from 3 to  $10 \times 10^{19} \text{m}^{-3}$  and the magnetic field lies typically around 2T), the X-mode configuration is used for edge measurements and the O-mode for mid-core to core measurements. The radial position of the cutoff  $r$  is taken as the point of intersection between the antenna LOS and the cutoff layer while the geometric tilt angle is the angle formed between these two. In the plasma core, where the cutoff layers become more circular, the tilt angles can range from  $5^\circ$  to  $30^\circ$ .

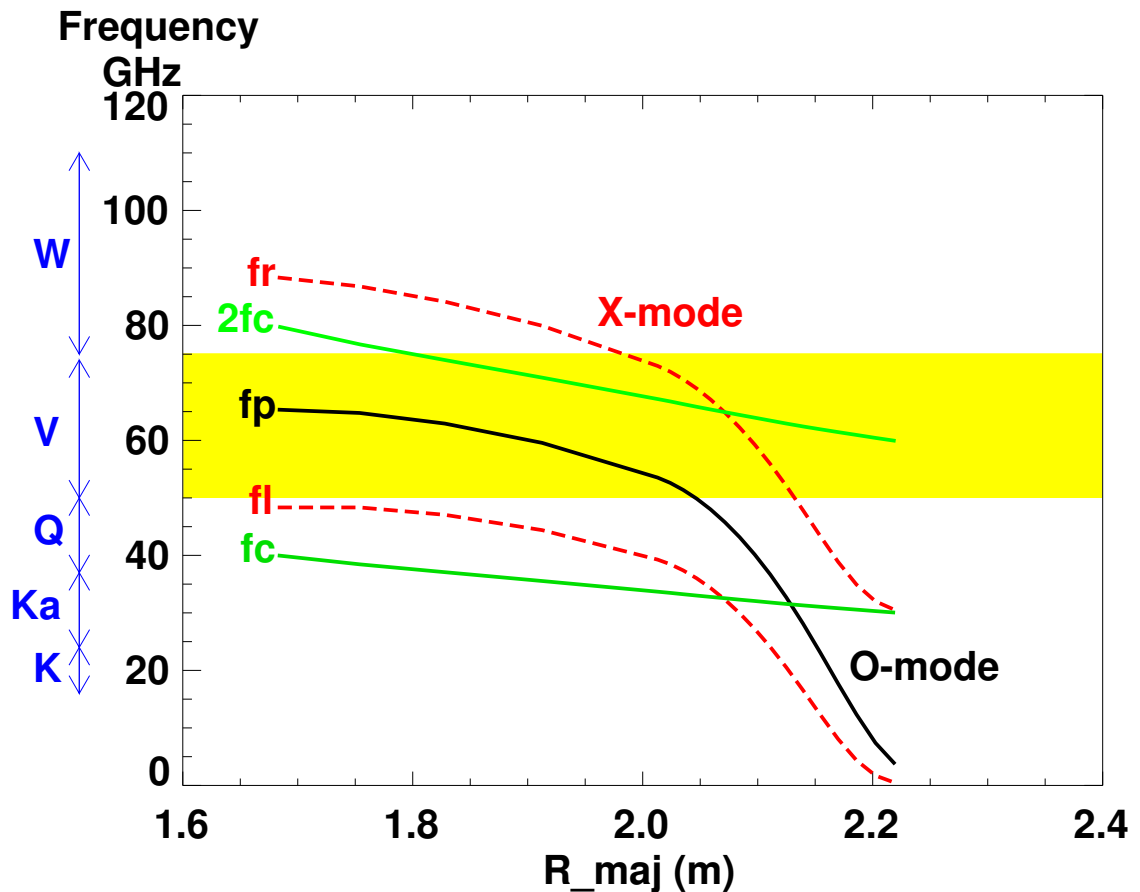


Figure 5.3: Radial profiles of O-mode ( $f_p$ ) and X-mode ( $f_r$ ) cutoff frequencies along with the electron cyclotron ( $f_c$ ) and left-hand ( $f_l$ ) frequencies for discharge #19148.

Figure 5.3 is another way of illustrating the O-mode and X-mode cutoff layers in discharge

# 19148. Here, the cyclotron  $f_c$ , plasma  $f_p$ , right hand  $f_r$  and left hand  $f_l$  frequencies are plotted as a function of the major radius,  $R$ . The limits of the V-band are seen more visibly in this figure. Generally, only the right-hand cutoff frequency, also known as the upper hybrid frequency, is seen in the V-band range and the left-hand (lower) cutoff may be neglected. From the cutoff equations,  $f_r$  and  $f_p$  model the X-mode and O-mode cutoff layers accurately (omitting the small change the  $\cos\theta$  term makes in equations 4.20, 4.25 and 4.26). As in figure 5.2, the X-mode cutoffs occur at the plasma edge and the O-mode cutoffs occur in the core region with some overlap between the two. The cyclotron frequency (or usually its resonance  $2f_c$ ) may increase into the V-Band range and block the plasma or right-hand cutoff frequencies. If this occurs, no Doppler shifts are observed because there is no plasma cutoff. The probing microwave beam is absorbed by the cyclotron frequency.

### 5.1.3 Beam Tracing with TORBEAM

The radial cutoff position, necessary for evaluating Doppler measurements, is determined from poloidal cross sections similar to figure 5.2. Recall that this position is the location in the plasma where the antenna LOS intersects with the plasma cutoff layer surface calculated for a particular microwave probing frequency. However, this method assumes that the launched microwave beam follows the antenna LOS in the plasma. It does not account for microwave beam refractive effects, which may be very strong in the plasma core. As a result, ray tracing calculations have been performed for several core measurements presented in this thesis to correct for the radial cutoff position.

TORBEAM is a beam-tracing code developed at ASDEX Upgrade mainly for numerical calculations of Electron Cyclotron Resonance Heating (ECRH) and Current Drive. It calculates the propagation and absorption of a Gaussian wave beam in a tokamak plasma [68]. It differs from conventional ray tracing codes in that it takes into account effects of diffraction. The code requires the launching conditions of the beam (i.e. frequency of the microwave beam, position of the launching antenna and the injection angle) along with the experimental (or theoretical) electron density, electron temperature and magnetic equilibria profiles of the discharge. As a result, the code may also be applied for modeling the trajectories of microwave beams launched from the Doppler reflectometer into ASDEX Upgrade plasmas. An example is shown in figure 5.4 for a Lower Single Null discharge.

The example shows the trajectories of the beam axis calculated by TORBEAM as thick curves for three different microwave beams launched in O-mode configuration with frequencies (50, 60 and 65GHz). The O-mode antenna LOS and its corresponding poloidal cutoff layers are shown for comparison. Note how the beam-traces and O-mode antenna LOS initially agree at the antenna position but then the beam-traces deflect within the plasma before reaching the appropriate cutoff layer. The further the beam penetrates into the core (i.e. the higher the microwave probing frequency), the greater the difference between deflection and cutoff layer. Since the X-mode cutoff layers are typically at the plasma edge (shown by the dashed curves), beam refraction effects are minimal and beam-tracing is not required. However, in the O-mode example, it is apparent that the radial position of microwave reflection may change

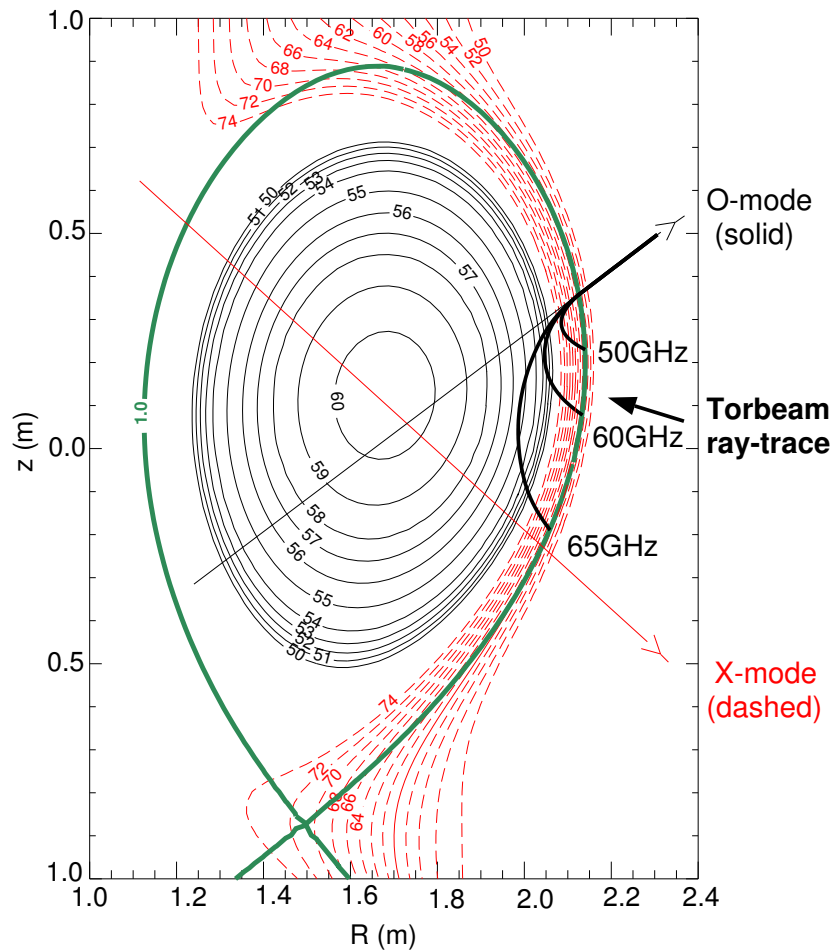


Figure 5.4: *O*-mode microwave beam trajectories calculated by TORBEAM during an *L*-mode phase (discharge # 18739 at 1.9s). The microwave frequencies are: 50, 60 and 65 GHz.

drastically when one compares the major radius,  $R$ , obtained from the antenna LOS intersection with the cutoff layer and the  $R$  obtained from the ray tracing result. In ray tracing results,  $R$  is taken as the radial position where the ray trace just bends over (i.e. the minimum radial position). For example, in figure 5.4, a microwave beam with 60GHz frequency undergoes cutoff at  $R = 2.05\text{m}$  using TORBEAM beam-tracing and  $R = 1.78\text{m}$  using the antenna LOS intersection method. This example clearly illustrates the drastic difference between the two methods and indeed makes the interpretation of Doppler core measurements more challenging. Nevertheless, it has been observed that these large deviations exist only when the plasma has high density gradients. When such discharges are encountered, TORBEAM beam-tracing is applied, otherwise the simpler geometrical LOS intersection method is utilized.

Although refractive effects are important to account for in the determination of the radial cutoff position, its role has been found to be negligible in the determination of the geometric tilt angle,  $\theta_{\text{tilt}}$  [10]. Consider a density profile broken up into a series of thin stratified layers each containing a different index of refraction. As the microwave enters each layer, it is refracted

by a certain tilt angle depending on the particular index of refraction and experiences a change in wavelength. The change in the wavelength is observed to compensate for the change in the tilt angle. Therefore, the geometric tilt angle can be taken as the angle formed between the antenna LOS and normal to the plasma flux surface.

## 5.2 Obtaining the Doppler Shifted Frequency, $f_D$

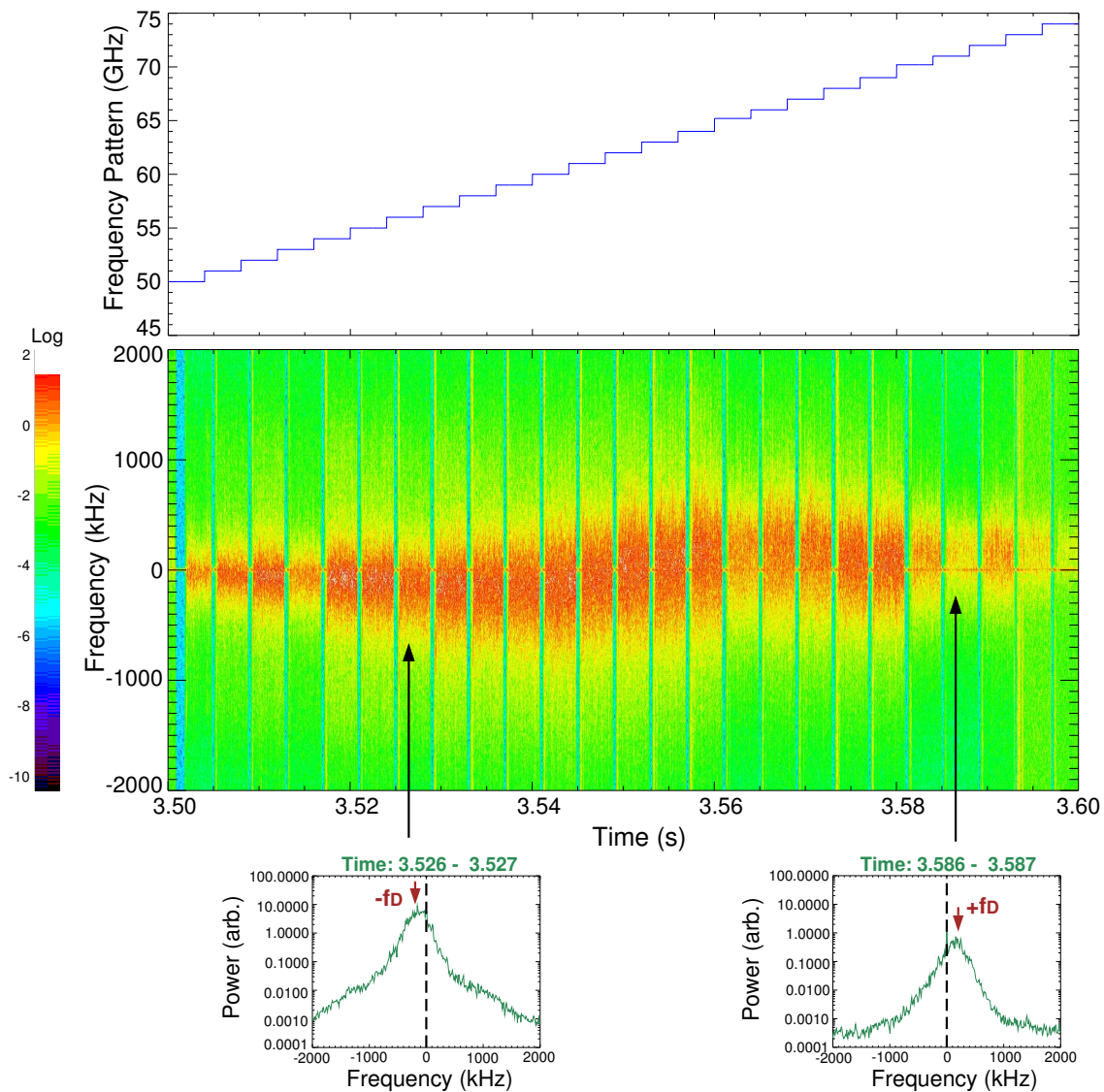


Figure 5.5: Frequency spectrum showing the raw Doppler reflectometer data along with the frequency pattern used to collect the data in X-mode. The data is shown for an L-mode USN discharge # 19413 at time = 3.5s to 3.6s.

Section 5.1 explained how radial cutoff positions and tilt angles are obtained for each dis-

charge and each microwave probing frequency. One other key piece of information missing for Doppler measurement analysis is the Doppler shift,  $f_D$ . Figure 5.5 illustrates an example of a typical microwave frequency launch pattern and the resulting frequency spectrum of the Doppler reflectometer raw data. In this particular example, the microwaves are launched in 1GHz frequency steps from 50 to 74GHz in 100ms. The frequency spectrum shows the zero frequency carrier signal as well as Doppler shifts either up or down shifted in frequency depending on the rotation direction. The Doppler shift is also observed in the complex amplitude signal  $Aexp(i\phi)$  spectrum. Two such spectra are shown at the bottom of figure 5.5. Typically, there is a narrow spike at zero frequency corresponding to the carrier wave intensity. Sometimes the  $m=0$  direct reflection component is also observed at zero frequency as a broader, lower amplitude peak [9]. The  $m=-1$  peak is the Doppler shifted peak which is of most interest. When the shift is large, it can be extracted by eye but when it is small, a fit routine is needed. In this case, the peak frequency is obtained by an algorithm which first removes the carrier peak, splits the spectrum into its symmetric and asymmetric components and then fits a double Gaussian to the asymmetric component using a Least-squares minimization [61].

### 5.2.1 Measurement Difficulties in H-mode

At the plasma edge, the Doppler shifts in H-mode are difficult to measure for several reasons. The first is that in H-mode, the better confinement means a reduction in turbulence. If the turbulence is too low, the microwave launched from the Doppler reflectometer has nothing to back scatter from and the received Doppler shifts are zero or very small. As well, when strong ELMs exist in the H-mode phase, the Doppler reflectometer signal is deterred as shown in figure 5.6. The ELMs appear as spikes in the Doppler reflectometry spectrum at the same time points as recorded by the  $D_\alpha$  line radiation intensity. The Doppler shifts in this spectrum are collected in an H-mode phase at the plasma edge where they are expected to be large and negative ( $\approx -1200\text{kHz}$ ). However, the spectrogram shows that the Doppler shifts are zero or very small right after an ELM and only after a short recovery time do they recover their expected large negative shift. There are two possible explanations for this effect. It has been observed that after the onset of an ELM, the plasma can transiently return to L-mode [69, 70]. The plasma may then return to H-mode after a short recovery time (usually around 1-2ms) or remain in L-mode, depending on the amount of plasma heating supplied in the discharge. Since the Doppler shifts are smaller in L-modes, this may explain why right after an ELM the Doppler shifts drop to lower values. A second possibility is that the quick back transition to L-mode right after an ELM changes the density profile. This could lead to a change in the cutoff position and would mean that the Doppler signal measured may not be in the vicinity of the pedestal, where the highest shifts are observed, but rather at another position in the plasma where lower shifts are predicted.

As a consequence, the Doppler reflectometry data used for analysis of H-modes is always taken in between ELMs. Generally, the shifts are most easily obtained near the L-H transition, where so-called *transition ELMs* exist. These ELMs are small, spiky and relatively unstable, making for ideal conditions for Doppler shift detection.

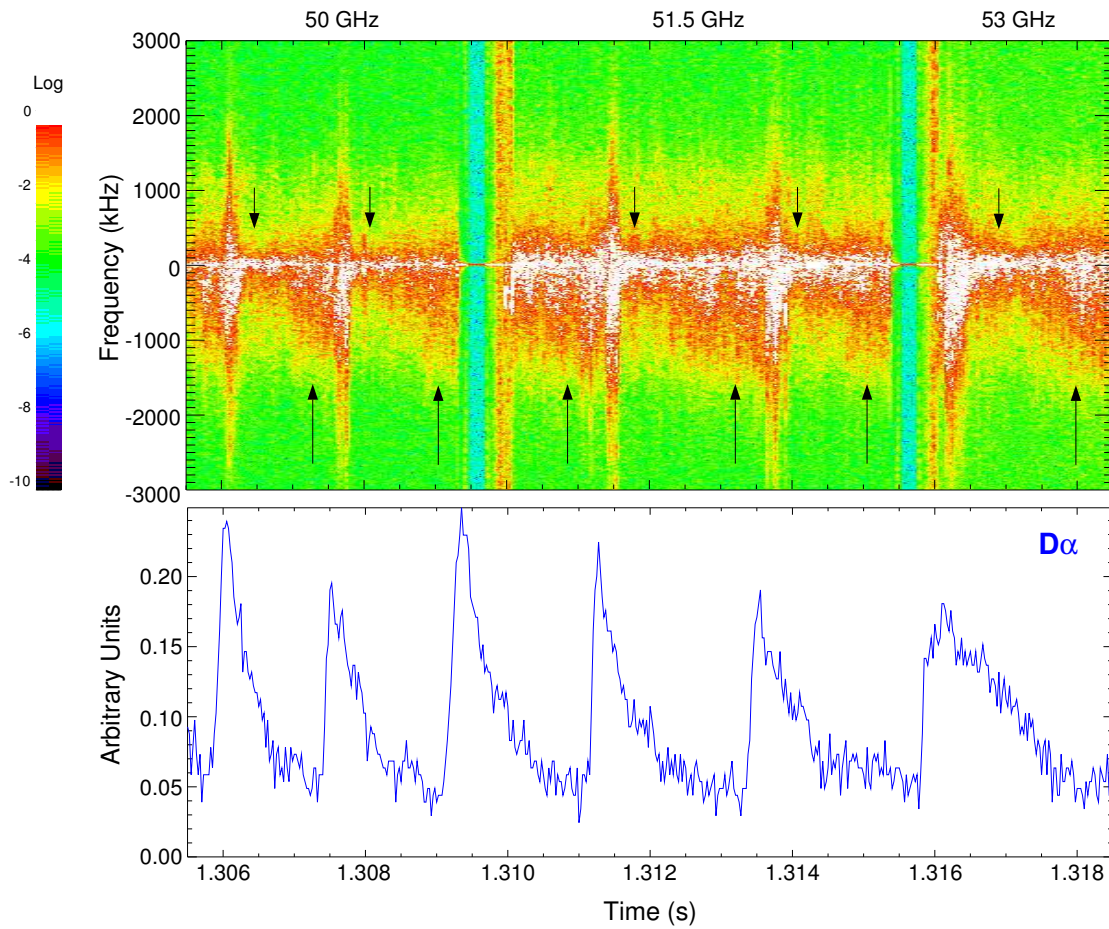


Figure 5.6: A close-up of the frequency spectrum collected during the H-mode LSN discharge # 16783. The ELMs appear on the spectrum as sharp spikes. The short arrows pointing downwards indicate the zero (or very slightly negative) Doppler shifts right after the ELM while the larger arrows pointing upwards mark the recovered negative Doppler shift.

### 5.3 Single Channel Doppler Reflectometer

A single channel Doppler reflectometer permits the measurement of several important plasma parameters such as the perpendicular rotation of the turbulence in the plasma. From the rotation measurement, the much sought after parameter in tokamak studies, namely the radial electric field, may be deduced. How these parameters are obtained from the Doppler signals will be described here.

### 5.3.1 Calculation of the Perpendicular Rotation of the Turbulence

From the  $m=-1$  Doppler shift in the received microwave signal, one obtains the perpendicular rotation of the turbulence in the plasma ( $u_{\perp}$ ). The velocity is given by

$$u_{\perp} = f_D \lambda_o / (2 \sin \theta_{tilt}) \quad (5.1)$$

where  $f_D$  is the Doppler shift,  $\lambda_o$  is the wavelength of the incident microwave and  $\theta_{tilt}$  is the geometric tilt angle. (See section 4.1.3 for the derivation of equation 5.1.) By stepping the frequency of the probing microwave through the V-band range from 50 to 74GHz, Doppler shift spectra are obtained for each frequency. Using equation 5.1 to calculate  $u_{\perp}$  from the measured Doppler shifts and converting the microwave probing frequencies to radial cutoff positions, a rotation profile versus radius, such as in figure 5.7, may be constructed. Normally, the frequency is swept in 1GHz steps every 4ms to ensure that the rotation profile contains a sufficient number of data points in a short period of time (a complete profile is measured every 100ms). Note the rotation is plotted as a function of the normalized radius. For the majority of the results presented in this thesis, the normalized radius is used as opposed to the major radius since  $\rho_{pol}$  offers a consistent way of comparing discharges with various shapes.

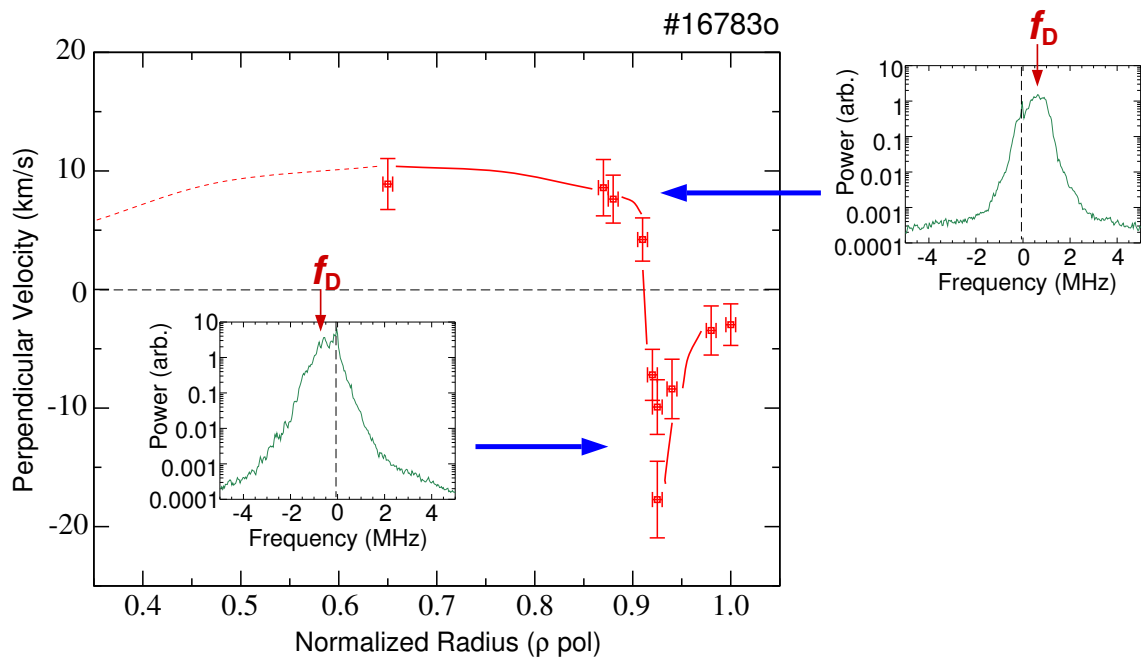


Figure 5.7: Rotation profile in an H-mode discharge from Doppler reflectometry measurements.

### 5.3.2 Calculation of the $E \times B$ velocity and the Radial Electric Field

The velocity  $u_{\perp}$  contains two components:

$$u_{\perp} = v_{E \times B} + v_{ph} \quad (5.2)$$

$v_{E \times B}$  is the velocity of the gyrocentre relative to the lab frame whereas  $v_{ph}$  is the phase velocity of the density fluctuation or turbulence moving in the plasma frame ( $E = 0$ ). Unfortunately, there is no direct measurement of either of these two components and thus, it is difficult to separate the two.

The  $E \times B$  velocity can be calculated from the radial force balance equation for a particular plasma species (i.e. ion, electron or impurity).

$$v_{E \times B} = v_{\phi} \frac{B_{\theta}}{B} - v_{\theta} \frac{B_{\phi}}{B} - \frac{\nabla P}{qnB} \quad (5.3)$$

As seen by equation 5.3, the  $E \times B$  velocity is composed of toroidal  $v_{\phi}$ , poloidal  $v_{\theta}$  and diamagnetic  $v^*$  velocity terms. On ASDEX Upgrade, the toroidal velocity is routinely measured by the charge exchange recombination spectroscopy (CXRS) diagnostic. The diamagnetic velocity may also be determined since  $\nabla P (= n\nabla T + \nabla nT)$ ,  $q$ ,  $n$  and  $B$  are all available measurements. The poloidal velocity, however, is not an easily available measurement, particularly at the plasma edge where a plasma 'spin up' is expected. At the moment, the CXRS diagnostic can only provide poloidal velocities in the plasma core (0.3 to 0.6 normalized radius). Here, the poloidal velocity is very small, approximately  $1 - 5 \text{ km/s}$ . The error bars in this measurement typically exceed the measurement itself and therefore, the interpretation is difficult. Moreover, the plasma edge where poloidal rotation is thought to be important is not even seen by the CXRS diagnostic. As a result, the  $E \times B$  velocity is very difficult to obtain from the force balance equation with the current diagnostics on ASDEX Upgrade.

The intrinsic phase velocity of the turbulence,  $v_{ph}$ , is also a challenge to measure although there are strong indications that it may be negligible in comparison with  $v_{E \times B}$ . Assuming the Doppler reflectometer has a tilt angle of approximately  $15^{\circ}$  (normally it ranges anywhere between  $10^{\circ}$  to  $25^{\circ}$ ), it probes fluctuation wavenumbers around  $6 - 8 \text{ cm}^{-1}$ . At the plasma edge, the turbulence is expected to be predominantly drift wave like. Calculations with a drift wave model have shown that the phase velocity at these  $k$  values drop to a fraction of the diamagnetic velocity [71]. Also, comparative measurements of Doppler reflectometer and CXRS velocities on the W7-AS stellarator show that at the plasma edge  $u_{\perp} \approx v_{E \times B}$  during steady-state conditions [10]. Based on these studies,  $v_{ph}$  is assumed negligible and equation 5.2 reduces to  $u_{\perp} \approx v_{E \times B}$ , giving the radial electric field:

$$E_r = -u_{\perp} \times B \quad (5.4)$$

It should also be pointed out that the  $E_r$  measurements as well as all other Doppler measurements presented in this thesis are *local* measurements, i.e. they are measured along the antenna LOS. The plasma potential  $\Phi$  is constant on the flux surface but since flux surface spacing varies poloidally, the radial electric field, which is  $E_r = -\nabla\Phi$ , varies with position. With the current Doppler reflectometer system, it is not possible to study this variation.

## 5.4 Dual Channel Doppler Reflectometer

The correlation Doppler reflectometry system consists of two identical V-Band heterodyne reflectometers. In this technique, the two Doppler reflectometer channels are connected to the same antenna pair so that they launch microwaves with the same line of sight simultaneously into the plasma. The microwaves have different launch frequencies ( $f_1$  and  $f_2$ ) and therefore reflect from different radial positions in the plasma ( $r_1$  and  $r_2$ ), as seen in figure 5.8. Two correlation measurement techniques have been developed; one for  $E_r$  shear measurements and one for  $L_r$  measurements.

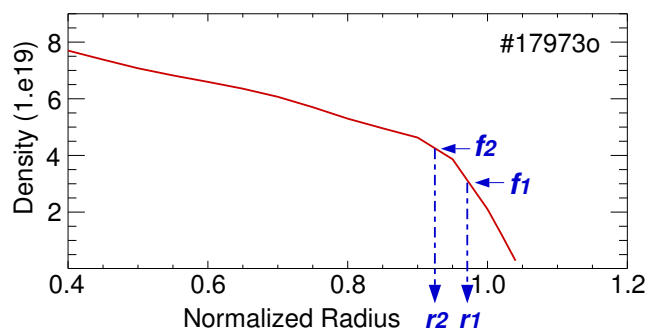


Figure 5.8: Example density profile illustrating the correlation technique where two microwave beams with different frequencies ( $f_1$  and  $f_2$ ) are launched simultaneously into the plasma and reflect at two different radial cutoff positions ( $r_1$  and  $r_2$ ).

### 5.4.1 Calculation of the Radial Electric Field Shear

By repetitively sweeping the launch frequencies of the microwave beams with a constant fixed frequency difference, two simultaneous radial profiles of the perpendicular rotation velocity ( $u_{\perp}$ ) can be constructed from the Doppler frequency shift in the reflectometer signal. The  $E_r$  profiles for each channel are then determined by Equation 5.4. Finally, taking the difference between the two channels'  $E_r$  values measured at the same time divided by their radial separation gives a radial profile of the instantaneous  $E_r$  shear ( $\partial E_r / \partial r$ ). Figure 5.9 shows the steps taken to obtain an  $E_r$  shear profile. Typically, a frequency sweep pattern of 1GHz steps from 50 to 74GHz in 100ms with a fixed 2GHz separation is used.

In principle, if both microwave launch frequencies are kept constant, then  $\Delta f_D$  as a function of time can give information on fast changes in  $\partial E_r / \partial r$  at one radial position. However, in this work,  $f_1$  and  $f_2$  are stepped together to give  $\partial E_r / \partial r$  as a function of time at several radii.

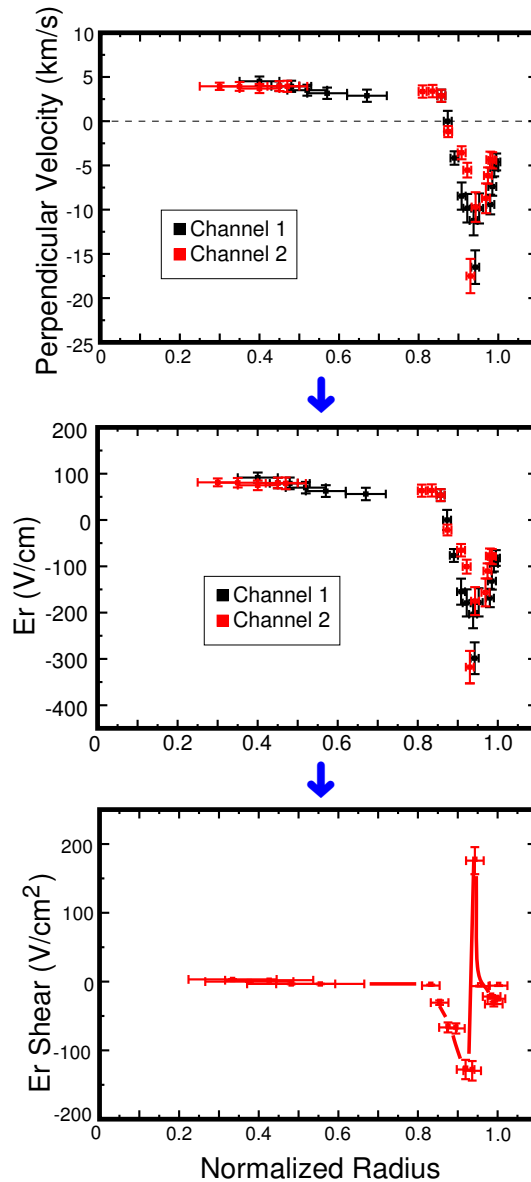


Figure 5.9: Processing steps for obtaining an  $E_r$  shear profile in the H-mode phase of discharge #17973: (1)  $u_{\perp}$  profiles for both Doppler channels (2)  $E_r$  profiles for both Doppler channels (3) instantaneous  $dE_r/dr$  profile.

#### 5.4.2 Calculation of the Radial Correlation Lengths of the Turbulence

Alternatively, keeping the frequency of one reflectometer channel  $f_1$  constant and sweeping the frequency of the second  $f_2$  permits the correlation properties of the turbulence to be measured. Here, a sweep every 50ms with a frequency difference between the two channels starting at 0.1GHz (to avoid any cross talk between the two channels) and increasing logarithmically was found to be sufficient. Cross correlating the two Doppler shifted reflectometer signals gives

the coherence between the two signals as a function of their frequency separation. Again, the  $n_e$  profile is required to translate the frequency separation to a radial separation  $\Delta r$ . The radial separation when the coherence drops to  $1/e$  gives a measure of the spatial correlation of the turbulence (designated the radial correlation length,  $L_r$ ) for the particular  $k_\perp$  studied.

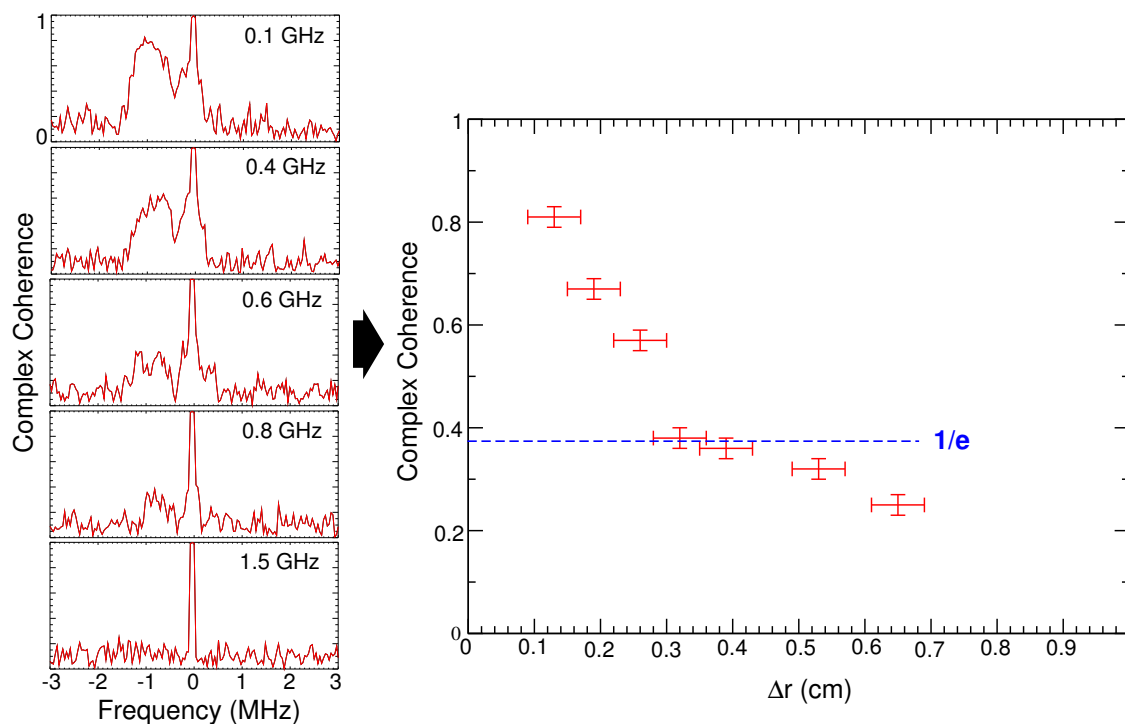


Figure 5.10: The complex coherence calculated as a function of radial separation  $\Delta r$  for USN L-mode discharge # 19148 (2.95-3.00s).

Figure 5.10 shows on the left hand side several coherence spectra obtained by cross correlating complex Doppler reflectometer signals ( $Ae^{i\phi}$ ). The cross correlation is a measure of similarity of two signals. It is given by the cross correlation function [72]:

$$R_{xy}(\tau) = \int_0^t x(t)y(t + \tau)dt \quad (5.5)$$

where  $\tau$  is the time lag between the two signals. The auto correlation functions are given by

$$R_{xx}(\tau) = \int_0^t x(t)x(t + \tau)dt \quad (5.6)$$

$$R_{yy}(\tau) = \int_0^t y(t)y(t + \tau)dt \quad (5.7)$$

From Equations 5.5, 5.6 and 5.7, the correlation coefficient  $\rho_{xy}(\tau)$  may be obtained. It is defined as

$$\rho_{xy}(\tau) = \frac{R_{xy}(\tau)}{(R_{xx}(0)R_{yy}(0))^{1/2}} \quad (5.8)$$

The correlation coefficient measures the degree of linear dependence between  $x(t)$  and  $y(t)$  for lag  $\tau$ . By taking the fast Fourier transform (FFT) of  $\rho_{xy}(\tau)$ , the coherence as a function of frequency  $\gamma(f)$  is obtained. The coherence  $\gamma(f)$  can be calculated by

$$\gamma(f) = \frac{\langle S_{xy}(f) \rangle}{(\langle S_{xx}(f) \rangle \langle S_{yy}(f) \rangle)^{1/2}} \quad (5.9)$$

where  $S_{xy}$ ,  $S_{xx}$  and  $S_{yy}$  are the cross and auto spectra computed from the Fourier transform of the complex signals,  $X(f)$  and  $Y(f)$ . (Note that  $X(f)$  and  $Y(f)$  are the Fourier transforms of the signals  $x(t)$  and  $y(t)$ .) Coherence ranges from zero to one. It is equal to one when the signals are identical. Ideally, the coherence should drop to zero as the signals become more different. Statistically this is not the case as limited signal lengths prevent the coherence from dropping to exactly zero. As one can see from the coherence spectra in figure 5.10, a peak in the coherence is obtained at the same frequency as the Doppler shift. This peak decreases with increasing frequency difference as expected. The peak values are then plotted as a function of radial separation and the  $1/e$  coherence value is designated as the radial correlation length,  $L_r$ .

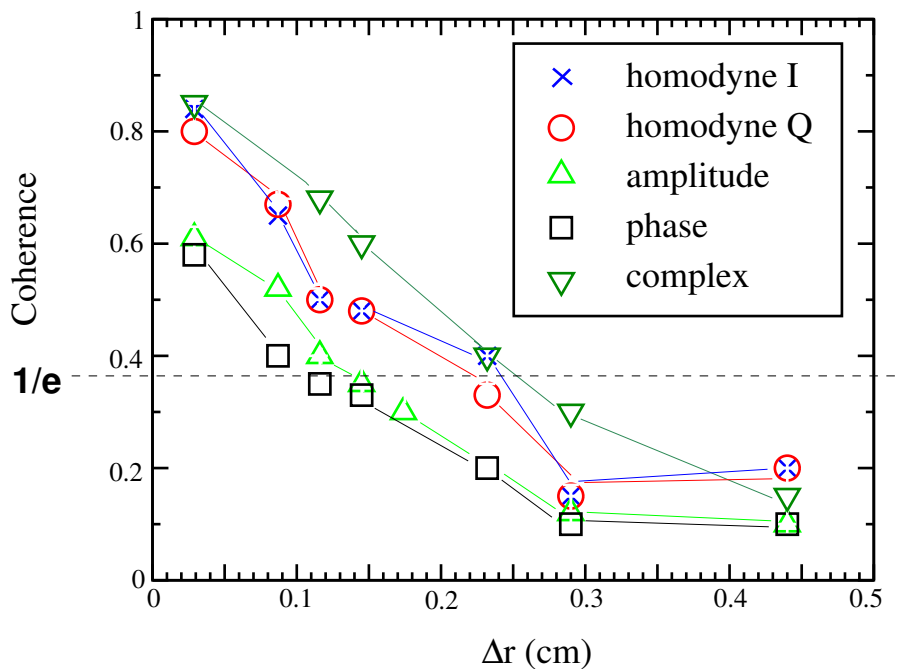


Figure 5.11: Radial coherence curves for a variety of Doppler fluctuation signals measured in  $L$ -mode discharge # 18761.

There is still some debate over the type of reflectometer signal best used to determine radial correlation lengths as well as in how the  $L_r$  lengths are defined [37]. An advantage of the current heterodyne reflectometers is the ability to study how the correlation length depends on the various reflectometer signals correlated. The reflectometer signals tested in this thesis are the homodyne in-phase ( $I = A \cos \phi$ ), homodyne quadrature ( $Q = A \sin \phi$ ), amplitude ( $A$ ), phase

( $\phi$ ) and complex ( $I + iQ = Ae^{i\phi}$ ) signals. The results are shown in figure 5.11 for an L-mode discharge at  $\rho_{pol} \approx 0.98$ . The coherence was obtained by correlating the various Doppler fluctuation signals. For all  $L_r$  measurements on ASDEX Upgrade, the complex and homodyne signals consistently give larger  $L_r$  than the amplitude and phase signals as seen in figure 5.11. Estrada also investigated this subject and found that the homodyne signals performed more reliably than the amplitude and phase signals [73]. This is most likely due to the fact that the homodyne and complex signals include both amplitude and phase information and therefore do not assign too much weight to either parameter, particularly during periods of low reflected power. Due to these findings, all  $L_r$  measurements presented in this thesis were obtained from the complex Doppler reflectometer signals.

## 5.5 Errors in the Doppler Measurement

Several errors in the measurement of  $u_{\perp}$  and  $E_r$  need to be accounted for. The most significant error is in the extraction of the  $m = -1$  Doppler peak frequency. The spectra shown in figure 5.7 are typical examples for extracting the Doppler frequency shifts. Generally the shifted peak is broad and the Doppler frequency  $f_D$  is taken as the frequency at the center of the peak with an error spanning the half width range of the peak. For small Doppler shifts, the error is typically  $\pm 50\text{kHz}$  but when the shifts are large (greater than 2MHz), the error can increase to  $\pm 300\text{kHz}$ .

Another significant error in  $u_{\perp}$  and  $E_r$  measurements is the determination of the radial cutoff position  $\rho_{pol}$ . To reduce this error, the best possible density profile is used for this calculation. Nevertheless, as was seen in section 5.1.3, beam refraction may also change the value of  $\rho_{pol}$  drastically in the plasma core. As a result, the error in  $\rho_{pol}$  is generally set between 0.005 to 0.02 depending on where the measurement is taken (i.e. plasma edge or core) and which density diagnostics are available.

Other contributions to the error in  $u_{\perp}$  and  $E_r$  measurements are those introduced by the tilt angle of the microwave onto the normal plasma flux surface,  $\theta_{tilt}$ . This error is minimal compared to the others discussed above. Typically, tilt angles are around  $20^\circ$  with an error of  $\pm 1^\circ$ .

For correlation measurements, on the other hand, recall that the radial separation between the two Doppler reflectometer channels  $\Delta r$  plays a key role in obtaining  $E_r$  shear and radial correlation lengths  $L_r$ . In this case, the position of the cutoff layer  $r$  is used not only for obtaining the position in the plasma of the Doppler measurement (as in rotation and  $E_r$  measurements) but also for calculating the actual magnitude of the measurement. Both variables  $dE_r/dr$  and  $L_r$  depend heavily on the precise measurement of  $r$ . Small changes in  $r$  may drastically alter the magnitude of these measurements along with its position. Again, a reliable density profile is needed for such measurements and the error in  $r$  is dependent on the quality of the  $n_e$  profile. Typical errors in  $r$  lie between 0.002cm and 0.02cm resulting in errors between 0.004cm and 0.04cm in  $\Delta r$ .

For  $L_r$  measurements, the error in the coherence is dependent on the data length (i.e. number of

fast Fourier transform FFT points and number of averages). Since the number of data points is fixed by the data acquisition, one has a compromise between spectral resolution and statistical error in the coherence. The uncertainty in the coherence is usually taken as  $\pm 0.02$  since this value is typical for the background noise observed on the coherence spectra (see figure 5.10).

# Chapter 6

## Perpendicular Rotation Measurements

This chapter presents several perpendicular rotation ( $u_{\perp}$ ) measurements made for typical ASDEX Upgrade discharges using the Doppler reflectometry diagnostic and the technique described in section 5.3.1. The main purpose will be to show that  $u_{\perp}$  represents the  $E \times B$  velocity and hence the radial electric field may be extracted from Doppler measurements. In section 6.2,  $u_{\perp}$  measurements will be compared with plasma fluid velocity measurements obtained from other diagnostics such as Charge Exchange (CXRS). The following sections will show that at the plasma edge, the magnitude of  $u_{\perp}$  depends heavily on the confinement of the discharge. Examples will also be given to illustrate how the direction (or sign) of the perpendicular rotation depends on the polarity of the plasma toroidal magnetic field  $B_{\phi}$  and plasma current  $I_p$ . A brief summary will conclude all  $u_{\perp}$  results.

### 6.1 The L-H Transition

The L-H (Low to High confinement) transition has been studied extensively since the H-mode was first observed in the ASDEX tokamak in the 1980's [12]. An important issue to address, which is still unanswered, is what causes the transition to the improved confinement observed in H-modes. Theory predicts that a strong plasma rotation at the edge pedestal region may be the cause for the improved confinement. It is believed that turbulent eddies are broken up by a strong poloidal velocity shear, thereby reducing the turbulence and increasing the confinement. Unfortunately many plasma diagnostics are not capable of providing data on the time scale in which the L-H transition occurs. Doppler reflectometry is an exception.

Figure 6.1 shows example  $u_{\perp}$  profiles during the L-mode phase (1.9s) of discharge # 17439 and shortly afterwards in the H-mode phase (2.2s). The frequency pattern was 1GHz steps from 50 to 74GHz in 100ms and data was collected simultaneously in both O and X-mode polarization. The time traces of several plasma parameters in discharge # 17439, where  $B_{\phi} = -2\text{T}$  and  $I_p = +0.8\text{MA}$ , are shown in figure 2.6.

This example shows the high spatial resolution available with the Doppler reflectometer. The red data points indicate the rotation measured in the H-mode phase and the black points are data from the L-mode phase. The  $u_{\perp}$  profiles are plotted versus normalized radius  $\rho_{pol}$ . Note

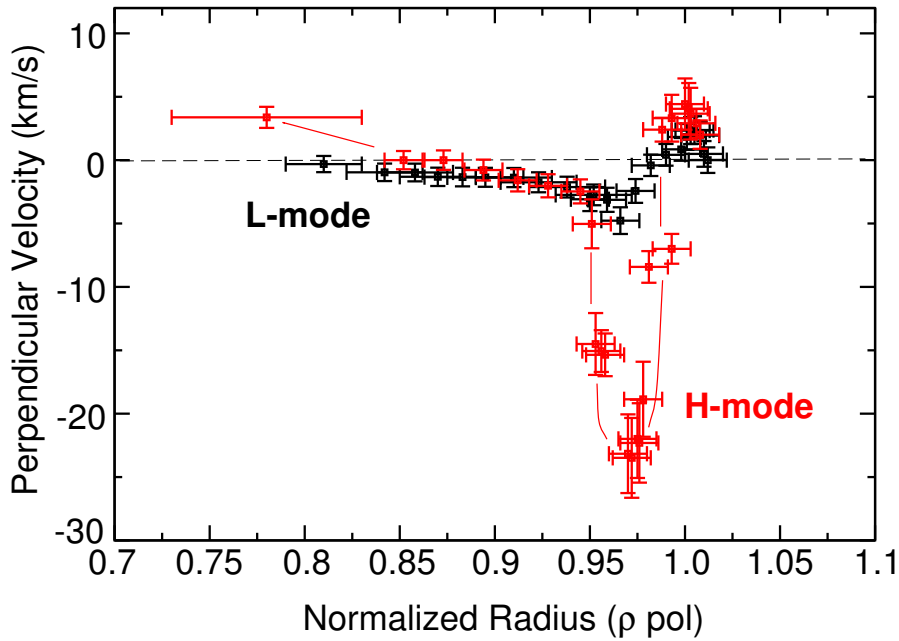


Figure 6.1: *Perpendicular velocity profiles measured using Doppler reflectometry during an L-mode and H-mode phase of discharge # 17439. Both O and X-mode polarization was used, thereby increasing the amount of data collected. Note the deeper well at the plasma edge in the H-mode rotation profile.*

that in the SOL (Scrape Off Layer), where  $\rho_{pol}$  is greater than one, a small positive rotation is measured. Then, at the plasma edge, in the so-called 'pedestal' region of the plasma, both profiles undergo a reversal in rotation direction. However, it is clearly evident that the H-mode rotation reaches a much lower minimum velocity  $[(-23 \pm 3)\text{km/s}]$  as opposed to the minimum rotation detected in L-mode  $[(-5 \pm 1)\text{km/s}]$ . This is a typical result for standard configuration discharges with  $-B_\phi$  and  $+I_p$ . Generally, in such discharges, plasma edge measurements show H-mode rotation wells ranging from -15 to -30km/s while L-mode rotation wells range from -5 to -10km/s. Klänge has used the same Doppler reflectometer diagnostic system on ASDEX Upgrade to monitor the evolution of  $u_\perp$  during the L-H transition [61]. He has observed as a function of time the steady increase in absolute peak value of  $u_\perp$  during the L-H transition.

Two questions arise from this result:

- 1) What causes this large difference in edge rotation between L-modes and H-modes?
- 2) What is the significance of such a high edge rotation?

The first question will be addressed in the following section and the second in section 6.3.

## 6.2 ExB Velocity Components

In order to better understand the  $u_{\perp}$  results obtained in L and H-modes, it is necessary to review equation 5.3:

$$v_{E \times B} = v_{\phi_i} \frac{B_{\theta}}{B} - v_{\theta_i} \frac{B_{\phi}}{B} - \frac{\nabla P_i}{qn_i B} \quad (6.1)$$

for the ion species, where  $v_{\phi_i}$  is the ion toroidal fluid,  $v_{\theta_i}$  the ion poloidal fluid and  $v_i^* = \nabla P_i / qn_i B$  the ion diamagnetic velocity. Assuming that  $u_{\perp} \approx v_{E \times B}$ , one can compare the three  $v_{E \times B}$  components with  $u_{\perp}$  and determine which component(s) play a significant role in the edge pedestal region where the large change in  $u_{\perp}$  is observed.

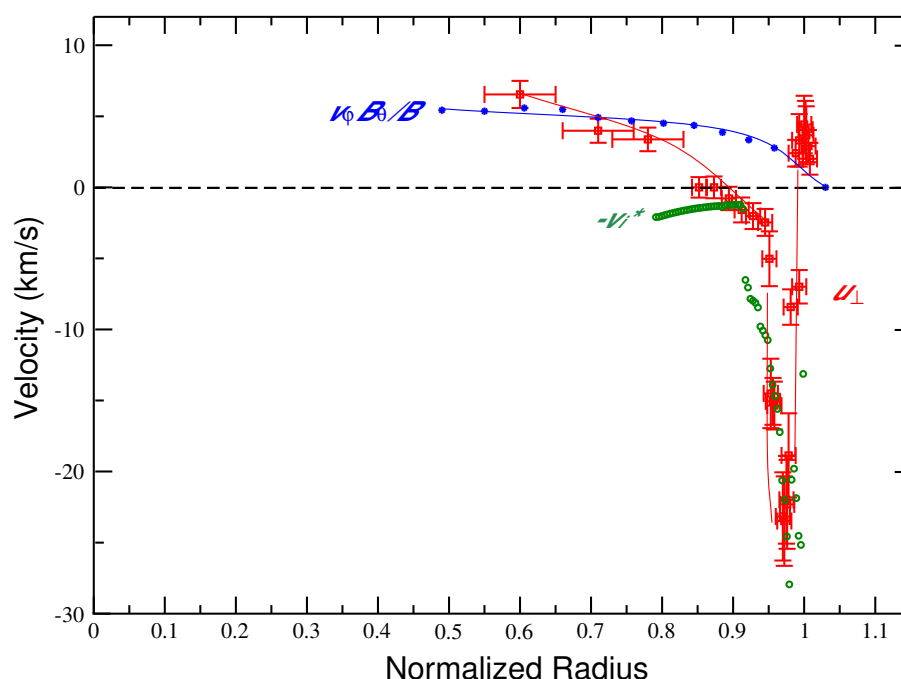


Figure 6.2: Velocity profiles measured at 2.2s in the H-mode phase of discharge # 17439. The  $u_{\perp}$  profile follows  $v_i^*$  at the plasma edge and  $v_{\phi_i} B_{\theta}/B$  in the core.

Figure 6.2 shows for discharge # 17439, the  $u_{\perp}$ ,  $v_{\phi_{imp}} B_{\theta}/B$  and  $v_i^*$  profiles at 2.2s.

### 6.2.1 The Toroidal Impurity Velocity

The blue curve in Figure 6.2 is the toroidal impurity fluid velocity  $v_{\phi_{imp}}$  mapped to the perpendicular frame by the  $B_{\theta}/B$  term. The impurity toroidal velocity is obtained from charge exchange recombination spectroscopy (CXRS), with the  $C_{V\lambda} 529.05\text{nm}$  CX line. It is routinely measured on ASDEX Upgrade by two CXRS systems, CHR [74] and the older system CER [75, 76]. In neoclassical theory, a difference is predicted between the main ion toroidal velocity and the impurity toroidal velocity [77]. Nevertheless, it was found that in ASDEX Upgrade H-mode discharges, the neoclassical correction between main ion and impurity toroidal rotation

velocities is small [78]. Only in discharges where the  $T_i$  profile becomes much steeper, should neoclassical corrections be necessary. Thus, for our purposes, the impurity toroidal velocity measured by CXRS is assumed equivalent to the main ion toroidal velocity and therefore it can be used to represent  $v_{\phi_i}$  in equation 6.1.

The toroidal velocity is usually generated by toroidally oriented neutral beam injection (NBI). It is small at the plasma separatrix and increases into the core steadily, reaching more than 100km/s. Because  $B_\theta$  is zero on axis, the poloidally mapped toroidal velocity plateaus around mid-core and then decreases to zero on axis. Note that in the core plasma region,  $u_\perp$  generally follows the mapped toroidal fluid velocity.

### 6.2.2 The Ion Diamagnetic Velocity

The ion diamagnetic velocity  $v_i^*$  was also calculated for discharge #17439 using the experimental electron density profile shown in figure 2.7 (and assuming that  $n_e \approx n_i$ ) and the experimental ion temperature profile from the charge exchange diagnostic. The pressure  $P_i$  was first calculated using the relation

$$P_i = n_i T_i \approx n_e T_i \quad (6.2)$$

and then its gradient  $\nabla P_i = dP_i/dr$ . Both the pressure and diamagnetic velocity profiles in the L and H-mode phases are presented in figure 6.3.

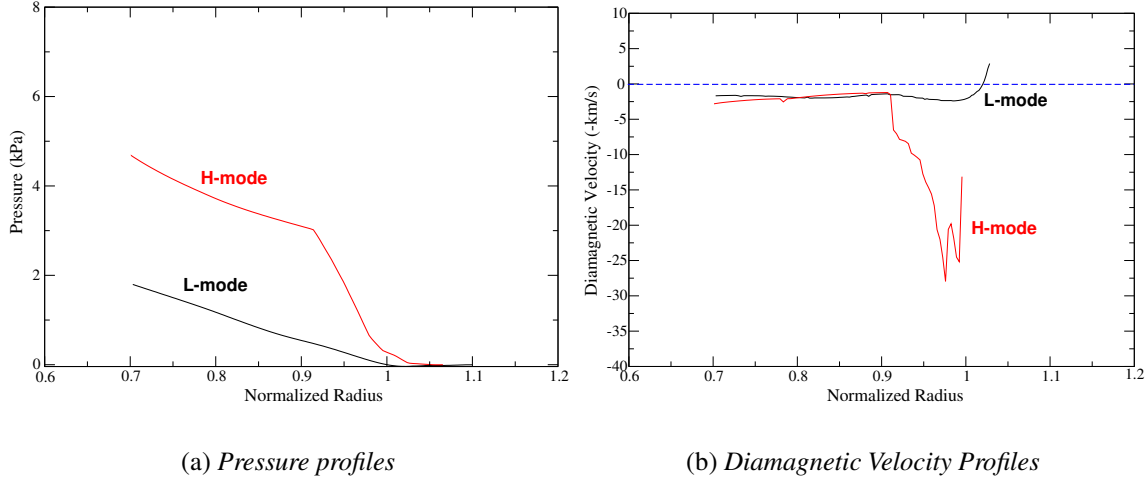


Figure 6.3: Ion diamagnetic velocity profiles calculated using the ion temperature and electron density profiles in L-mode (1.9s) and H-mode (2.2s) phases of discharge # 17439. The H-mode pressure profile experiences a large gradient at the pedestal edge region, resulting in a large diamagnetic velocity in comparison to the L-mode phase.

Similar to the electron density and temperature profiles in H-mode shown in figure 2.7, the H-mode ion pressure profile also shows a steep gradient coinciding with the H-mode pedestal

barrier. As a result, this large pressure gradient causes the diamagnetic velocity to dominate the  $u_{\perp}$  profile at the plasma edge, see figure 6.2. It is also now evident that the large difference in  $u_{\perp}$  at the plasma edge between L-modes and H-modes can be explained by the larger pressure gradient and hence larger diamagnetic velocity in H-modes.

### 6.2.3 The Poloidal Velocity

The poloidal velocity  $v_{\theta}$  is unfortunately not shown in figure 6.2 as this measurement was not made for discharge #17439. Typically, poloidal velocity measurements on ASDEX Upgrade are made with the CXRS diagnostic, using its poloidal lines of sight. Earlier experimental measurements of the poloidal velocity, including their neoclassical corrections, have shown very small poloidal rotation speeds around  $\pm 5$  km/s in the plasma [76]. However, even a small poloidal rotation may contribute greatly to the  $v_{E \times B}$  since  $v_{\theta}$  is multiplied with the large  $\approx 2$  T toroidal magnetic field  $B_{\phi}$ . CXRS measurements on other machines, such as the DIII-D tokamak, have shown that the poloidal velocity is very high, particularly at the plasma edge in H-modes [38]. This high poloidal velocity is sometimes called a 'poloidal spin-up' of the plasma.

In conclusion, the  $u_{\perp}$  profile is dominated by the toroidal velocity in the plasma core whereas at the edge, the poloidal velocity and diamagnetic velocity are more significant. The diamagnetic velocity appears to account for the large edge  $u_{\perp}$  well observed in H-modes.

## 6.3 Dependence on Plasma Confinement

In section 6.1, it was shown that the absolute peak value of  $u_{\perp}$  is greater at the plasma edge in H-mode than in L-mode. Although it is now understood where this higher rotation comes from (i.e. from steep density and temperature gradients), the significance of a higher perpendicular rotation is discussed here. It has been observed with Doppler reflectometry that discharges with very high confinement on ASDEX Upgrade tend to have larger absolute magnitudes of  $u_{\perp}$  at the plasma edge. As a further example,  $u_{\perp}$  was measured in a highly confined quiescent H-mode (QH-mode) discharge #16111, where  $B_{\phi} = +2$  T,  $I_p = -1.0$  MA. The time traces of plasma parameters in this discharge and the behaviour unique to this scenario has previously been discussed in chapter 3.

Figure 6.4 shows the  $u_{\perp}$  QH-mode profile (measured at 3.0s) in green along with the H-mode profile (obtained at 4.0s) in red for comparison. Again, peak values in  $u_{\perp}$  are measured coinciding with the edge pedestal region where  $\rho_{pol} \approx 0.96$ . In QH-mode discharges, the density is typically low (around  $4.5 \times 10^{19} \text{ m}^{-3}$ ) so that X-mode polarization is required for measurements within the plasma. These measurements are concentrated at the plasma edge for this scenario.

The measured peak rotation is  $32 \pm 3$  km/s in the QH-mode phase but only  $18 \pm 2$  km/s in the H-mode phase. So far the largest  $u_{\perp}$  measured has been during a QH-mode discharge. The QH-mode is known for its superior confinement. In DIII-D,  $\beta_N H_{89}$  values of 7 were obtained

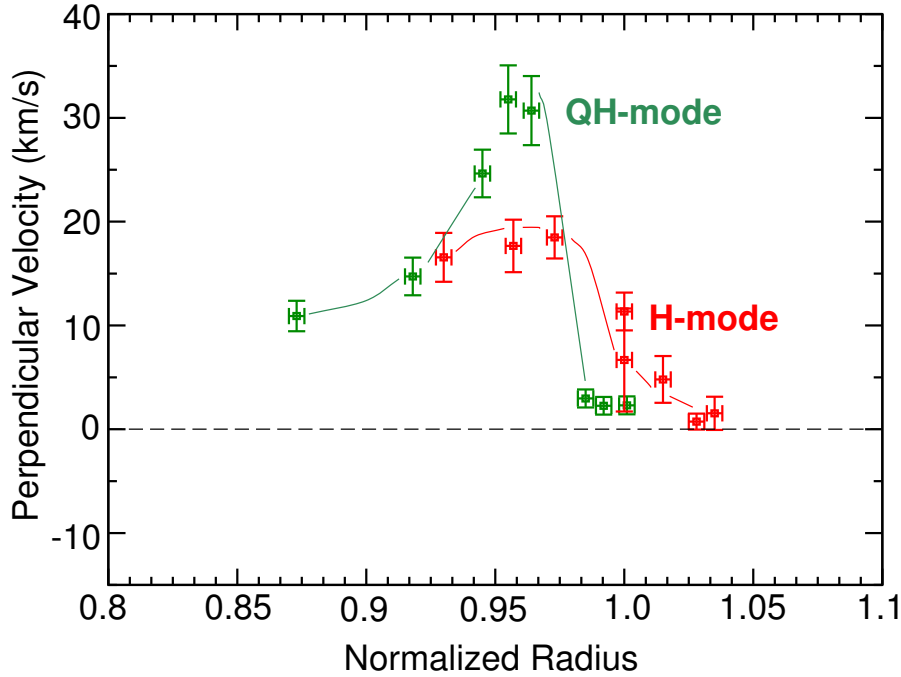


Figure 6.4: *Perpendicular velocity profiles measured in the Quiescent H-mode phase and ELMy H-mode phase of discharge #16111. Cutoff occurs only in the edge region because of the low density of the discharge.*

in QH-modes compared with values of 4 in standard ELMing H-modes [24]. It is believed that this improved confinement is linked to the higher radial electric field ( $E_r$ ) in the QH-mode [24]. Since  $u_{\perp}$  is directly related to the radial electric field (see equation 5.4) a higher perpendicular rotation in this scenario is expected.

In general,  $u_{\perp}$  profiles seem heavily dependent on the confinement of the discharge. A higher rotation normally results in a large  $E \times B$  velocity shear. The sheared flow tears the turbulent eddies in the plasma apart, thereby simultaneously reducing the anomalous transport caused by turbulence and improving confinement [79]. This will be discussed in greater detail along with the  $E_r$  and  $E_r$  shear measurements in the next chapter.

One notable difference in the  $u_{\perp}$  profiles presented at this stage is their difference in sign. Previously, in figure 6.1, the H-mode perpendicular rotation was negative at the plasma edge, but in figure 6.4, it is shown as positive. This reversal in rotation direction is due to the polarity of the plasma toroidal magnetic field and poloidal current, which will now be discussed.

## 6.4 Dependence on Plasma Configuration

Discharge #17439 has a standard ASDEX Upgrade configuration with a negative toroidal magnetic field ( $-B_{\phi}$ ) and a positive plasma current ( $+I_p$ ). However, three other combinations of  $B_{\phi}$  and  $I_p$  polarities are possible on ASDEX Upgrade, as described in section 2.3.2. This offers

a test of whether  $u_{\perp}$  is directly related to the  $E \times B$  velocity since a change in the sign of the magnetic field  $B$  should result in a change in the rotation direction. To observe the effects of the  $B_{\phi}$  and  $I_p$  polarities on the magnitude and direction of  $u_{\perp}$ , Doppler measurements were made in these scenarios.

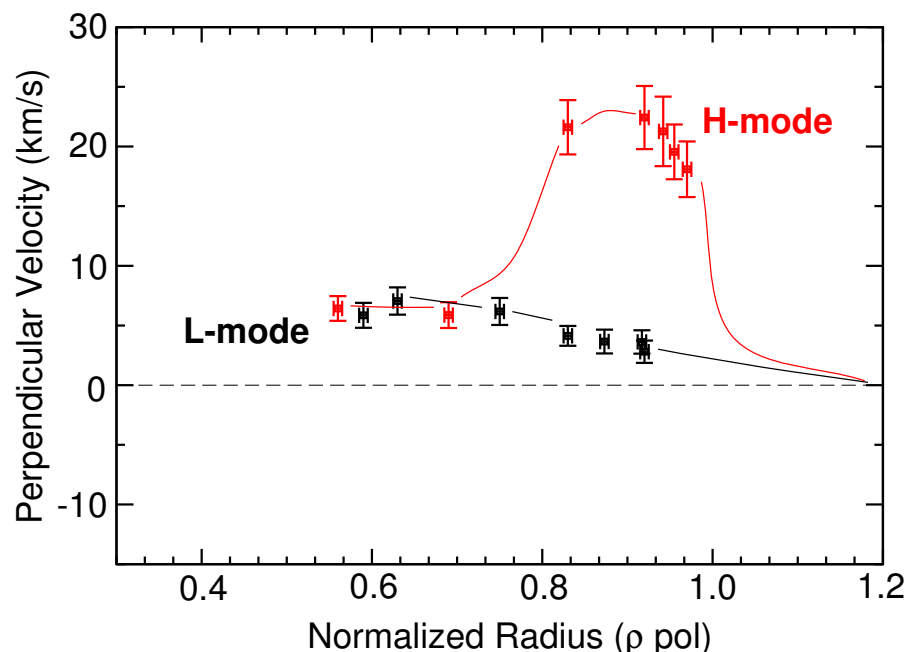


Figure 6.5: Perpendicular velocity profiles measured in discharge #16121 using O-mode polarization. Again, the H-mode rotation is higher at the plasma edge.

$u_{\perp}$  profiles measured in both H-mode and L-mode phases of discharge #16121 ( $B_{\phi} = +2.6\text{T}$ ,  $I_p = -1.0\text{MA}$ ) are illustrated in Figure 6.5. (Note that this discharge has the same  $B_{\phi}$  and  $I_p$  polarities as the quiescent H-mode discharge). In this configuration, both the magnetic field and current have reversed direction such that the magnetic field line helicity is maintained but the NBI is injected in the counter-current direction (counter-NBI). For such a case, the diamagnetic velocity reverses direction, from negative in the standard configuration to positive, due to its dependence on the magnetic field, recall  $v^* = \nabla P / qnB$ . The poloidally mapped toroidal velocity term, on the other hand, is still positive due to the cancellation in sign of  $B_{\theta}/B$ . As a result, the large  $u_{\perp}$  dip at the edge now becomes a peak in this scenario as the positive  $v^*$  adds to the positive toroidal velocity component. In such a scenario,  $u_{\perp}$  will always be positive in the plasma. Due to the addition of  $v^*$  to  $v_{\phi}$ , a broader peak in the rotation is also detected. In comparison, the L-mode profile, indicated by black data points in figure 6.5, experiences no predominant peak in rotation since  $v^*$  is small in L-modes.

Up to now, examples of LSN discharges have been given. However, on ASDEX Upgrade, the two other plasma configurations (i.e.  $-B_{\phi}, -I_p$  and  $+B_{\phi}, +I_p$ ) are typically performed in USN for reasons explained in section 2.3.2. Figure 6.6 shows a  $u_{\perp}$  profile measured in USN discharge #17707 with a negative toroidal magnetic field and a negative poloidal current. The

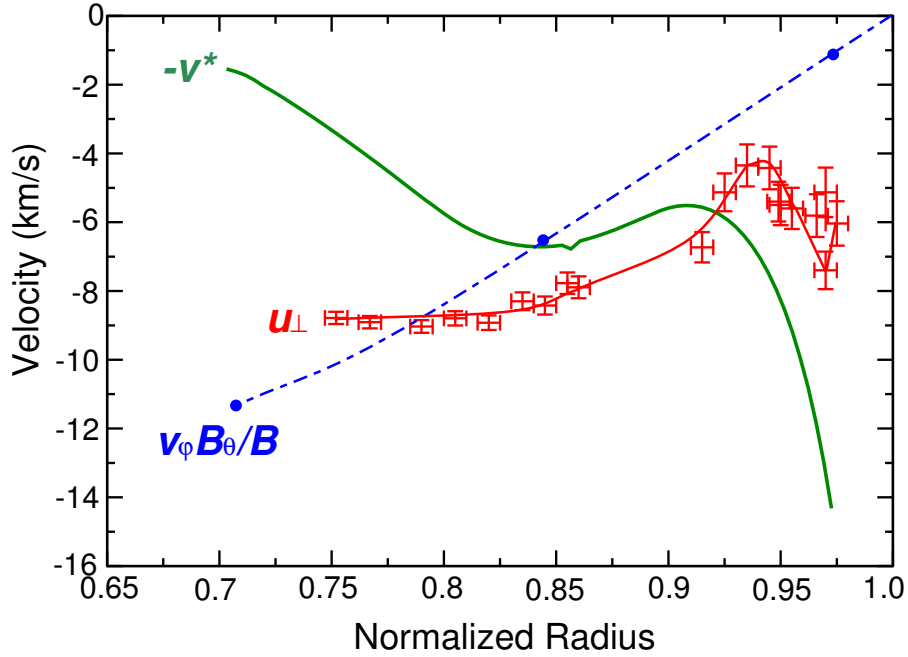


Figure 6.6: *Perpendicular, ion diamagnetic and toroidal impurity velocities measured in a  $-B_\phi, -I_p$  discharge. Both the ion diamagnetic and toroidal impurity velocity mapped on the poloidal plane are negative.*

poloidally mapped toroidal impurity velocity ( $v_{\phi_{imp}} B_\theta/B$ ) and ion diamagnetic velocity ( $v_i^*$ ), measured at time  $t = 2.3s$ , are also shown for this discharge.

For this configuration, the diamagnetic velocity is negative at the plasma edge and approaches zero around mid-core since the density and temperature profiles are flat in the core and the resulting pressure gradient falls to zero. Unlike the previous examples, the toroidal velocity component is now negative in this plasma configuration. As a result, the  $u_\perp$  profile will always be negative in the plasma for this configuration, as shown by the red data points in figure 6.6. Note that at the H-mode pedestal region ( $\rho_{pol} \approx 0.97$ ), a very small well of  $-7.4 \pm 0.5 km/s$  in  $u_\perp$  is detected. LSN H-mode wells were around  $-15$  to  $-30 km/s$ . This behaviour is a characteristic of USN discharges. The magnitudes of  $u_\perp$  in the H-mode edge region of USN discharges are comparable to the magnitudes in the edges of L-mode LSN discharges. A possible reason for this observation may be that USN discharges have poor confinement (similar to LSN L-modes) as opposed to LSN H-modes.

The following section will present an example rotation profile measured in the final and fourth possible tokamak configuration ( $+B_\phi, +I_p$ ).

## 6.5 Dependence on Magnetic Field

Equation 5.4 shows not only a dependence of  $u_{\perp}$  on the radial electric field  $E_r$  but also on the total plasma magnetic field  $B$ . If  $u_{\perp} \approx v_{E \times B}$ , then reversing  $B$  will reverse the direction of  $v_{E \times B}$  which should produce a corresponding reversal in the measured  $u_{\perp}$ . This may be tested on ASDEX Upgrade by comparing discharges with a reverse in only the magnetic field polarity.

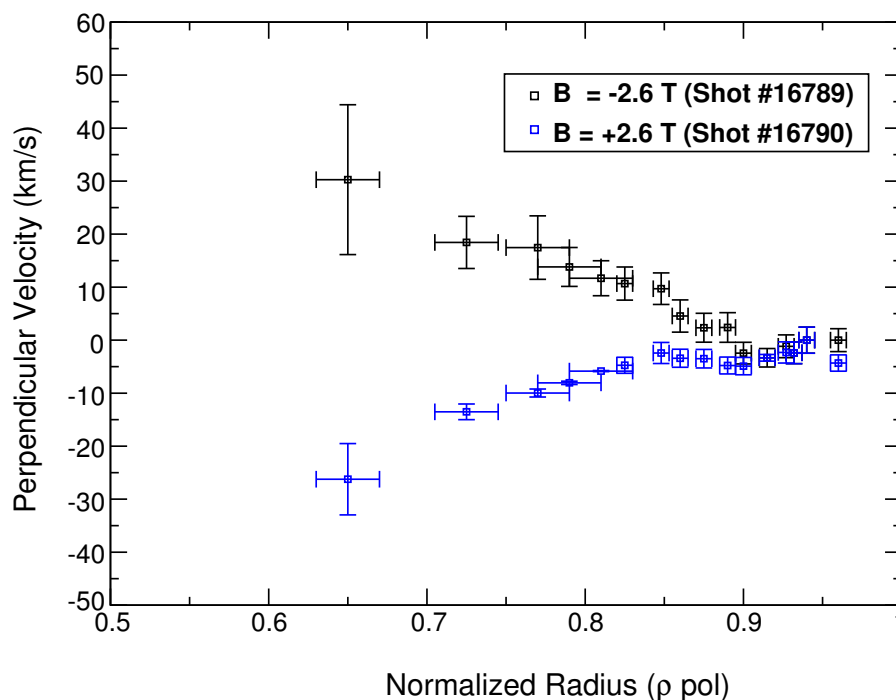


Figure 6.7: *Perpendicular velocity profiles measured during a pair of  $\pm 2.6$ T toroidal magnetic field discharges. The discharges are in USN configuration and the profiles are collected just after an L-H transition.*

Figure 6.7 presents the  $u_{\perp}$  profiles for a pair of closely matched USN discharges, with  $I_p = +0.8$ MA and  $B_{\phi} = \pm 2.6$ T. The profiles are collected just after the L-H transition (2.2s in discharge #16789 and 2.6s in discharge #16790). Similar to the previous USN discharge #17707, the magnitude of  $u_{\perp}$  is small at the plasma edge. This might be again due to the poor confinement in USN discharges in comparison with LSN discharges. As well, the profiles in this particular example were collected close to the L-H transition where the H-mode barrier may not have been fully developed. Nevertheless, as predicted, the  $u_{\perp}$  profiles are dependent on  $B$  since a reversal in  $B_{\phi}$  creates a reversal in the  $u_{\perp}$  profiles. The profiles are almost mirror images of each other.

Table 6.1 summarizes the four possible plasma configurations and the directions of electron diamagnetic, toroidal and perpendicular velocities within the plasma in these configurations. From experiments, there is at present little information available about the plasma poloidal

velocity in order to determine its direction of flow in the plasma.

$B_\phi$	$I_p$	$v^*$	$v_\phi$	$u_\perp$
-	+	-	+	- edge, + core
+	-	+	+	+
-	-	-	-	-
+	+	+	-	+ edge, - core

Table 6.1: *Various Plasma Configurations on ASDEX Upgrade with flow velocity directions. The standard ASDEX Upgrade configuration is a negative toroidal magnetic field and a positive poloidal current.  $u_\perp$  profile measurements would result in a reversal in flow direction for this standard configuration.*

## 6.6 Summary

On ASDEX Upgrade,  $u_\perp$  profiles have been measured using Doppler reflectometry for a variety of plasma scenarios and configurations. Equation 5.4 shows the dependence of  $u_\perp$  on the radial electric field  $E_r$  and on the plasma magnetic field  $B$ . These dependencies were observed in the experimental results, thereby confirming that  $u_\perp \approx v_{E \times B}$ . The results show a strong link between the confinement of a discharge and the magnitude of the perpendicular rotation. The higher the confinement, the higher the absolute peak value of  $u_\perp$  at the plasma edge. Theory predicts that confinement is linked to high  $E_r$  and in particular high  $E_r$  shear. Hence, the trend of increasing confinement with edge  $u_\perp$  values is expected. This trend was seen in the examples comparing poor confined L-modes with high confined H-modes and QH-modes. As well, the dependence of  $u_\perp$  on  $B$  was clearly observed in the example where the toroidal magnetic field was reversed in a closely matched discharge and the resulting  $u_\perp$  profiles were mirror images of each other.

By examining the various components of  $u_\perp$  given by the radial force balance equation for ion species,

$$u_\perp \approx v_{\phi_i} \frac{B_\theta}{B} - v_{\theta_i} \frac{B_\phi}{B} - \frac{\nabla P_i}{qn_i B} \quad (6.3)$$

it was found that at the plasma edge, the diamagnetic velocity dominates. In fact, the steeper gradients in the density and temperature profiles of an H-mode as opposed to an L-mode are the main reasons accounting for the larger  $v^*$  and  $u_\perp$  absolute magnitudes at the plasma edge. Neoclassical theory predicts that the poloidal velocity is also large in the edge region. The  $u_\perp$  profile, on the other hand, follows the poloidally mapped toroidal velocity component in the plasma core.

Changes in  $B_\phi$  and  $I_p$  polarities were also seen to affect the  $u_\perp$  profiles in both magnitude and direction (depending on whether  $v^*$  and  $v_\phi$  are added or subtracted). Generally, however, most discharges on ASDEX are performed in the standard configuration, which has a negative

toroidal magnetic field and a positive poloidal current. In such a configuration, the  $u_{\perp}$  profile undergoes a reversal in direction.

All of the rotation examples illustrated in this chapter were concentrated at the plasma edge. It is possible to also use the Doppler reflectometer for core measurements and examples may be found in reference [9]. However, here the analysis becomes more complicated due to the stronger microwave refractive effects.



# Chapter 7

## The Radial Electric Field and its Associated Shear

The radial electric field in a tokamak has been recognized as an important factor for plasma confinement and anomalous transport. Typically, the radial electric field in a plasma is determined using active charge exchange spectroscopy techniques and the radial force balance equation (equation 3.2). This method has limitations. First, the CXRS technique is dependent on neutral beam injection. This makes radial electric field measurements in purely ICRH or ECRH heated discharges impossible. In addition, the technique usually measures the impurity velocity of say, carbon, which according to neoclassical theory is not necessarily the same as the main deuterium ion velocity. Doppler reflectometry provides an alternative and more direct method of obtaining  $E_r$ . This chapter presents a survey of experimental radial electric field measurements made by Doppler reflectometry in a wide range of plasma scenarios. The results are then compared with the theory presented in chapter 3. In the fundamental transport equations, all direct radial electric field effects cancel and transport effects enter only through the derivatives of  $E_r$  (i.e. its shear). Hence, the radial electric field shear appears to be more important. By using two Doppler reflectometer channels, instantaneous  $E_r$  shear profiles may be obtained. The shear measurements are also compared with two opposing theoretical predictions. Biglari's theory claims that turbulence stabilization occurs for either sign of  $\partial E_r / \partial r$  [8] whereas in Shaing's model, turbulence stabilization occurs primarily for positive  $E_r$  shear [49]. The question as to which shear, positive or negative, is more important in turbulence stabilization will be addressed here.

### 7.1 Measurement of the Radial Electric Field

#### 7.1.1 Dependence on Plasma Confinement

Earlier perpendicular rotation results have indicated a stronger radial electric field at the plasma edge exists in H and QH-modes as opposed to the much lower confined L-modes. (See figures 6.1 and 6.4.) Figure 7.1 illustrates the radial electric field profiles measured in a standard

H-mode phase and an improved H-mode phase using the correlation Doppler reflectometer system. Improved H-modes were described previously in section 2.4.2. These modes have higher confinement with  $H_{98}$  factors around 1.2-1.4 than their standard H-mode counterparts, having  $H_{98}$  factors around 1.0. In the discharge, the data was collected by two Doppler reflectometer channels in O-mode polarization. A frequency difference of 2GHz between the channels was fixed and the frequency was stepped every 1GHz from 50 to 74GHz in 100ms. An enhancement in  $E_r$  is detected at the edge of the improved H-mode phase. A peak value of -480V/cm is measured there while only -306V/cm is measured in the standard H-mode phase. This lower magnitude of  $E_r$  is typical of most standard H-modes on ASDEX Upgrade.

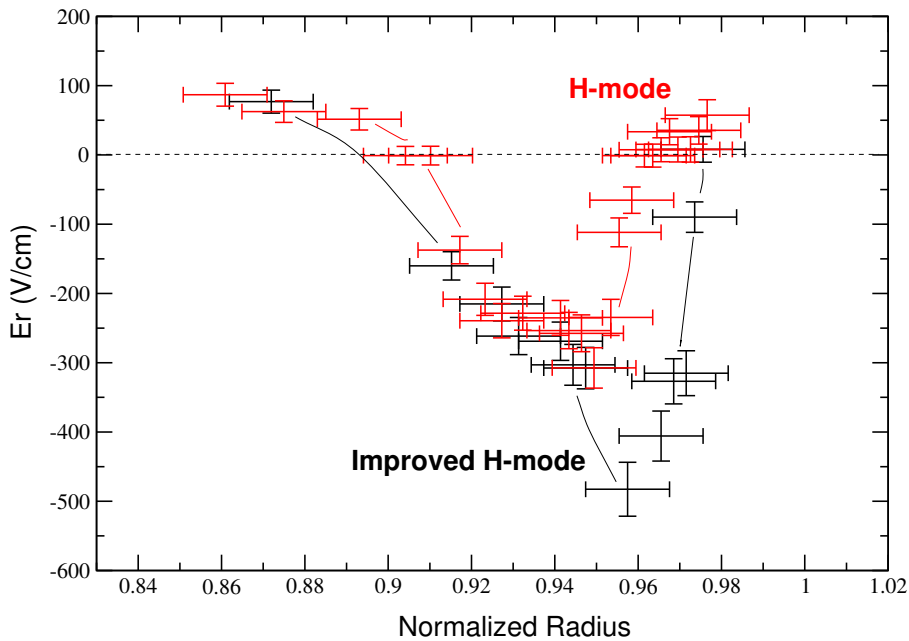
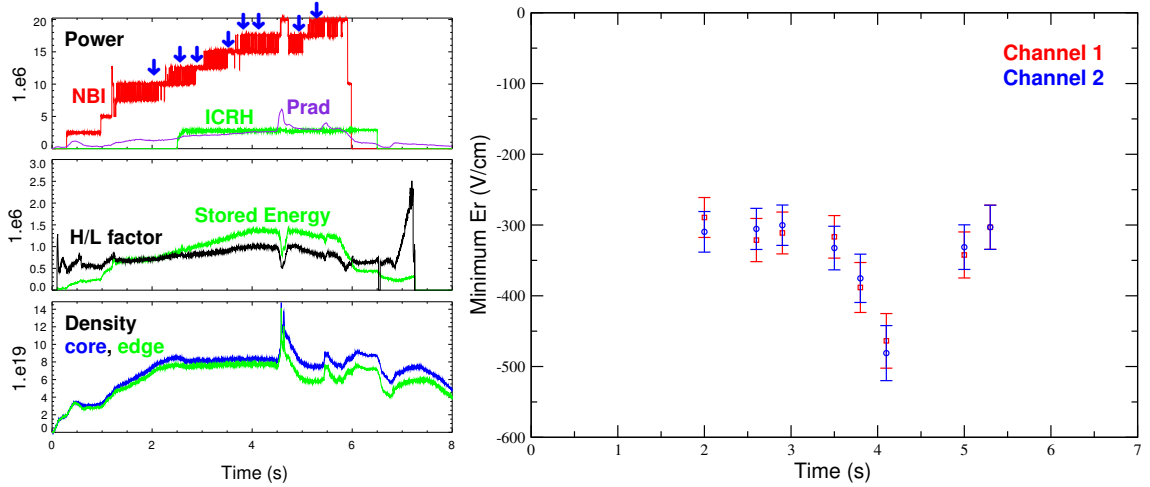


Figure 7.1: Radial electric field profiles measured during a typical H-mode phase (2.9s) and an Improved H-Mode phase (4.1s) in discharge # 19112. An enhanced  $E_r$  is measured in the Improved H-mode.

In this particular discharge, the electron density (from which the radial positions are derived) was available from DCN line interferometry and core Thomson scattering diagnostics. Neither of these diagnostics are specialized in edge density measurements and hence the radial resolution at the edge is poor. This may be a reason why the  $E_r$  wells in the two phases in figure 7.1 do not perfectly align. Nevertheless, the observation that the depth of the  $E_r$  well increases with an enhancement in plasma confinement is still valid.

Figure 7.2 shows on the left-hand side, the time traces of plasma heating power, confinement and density in discharge # 19112. Discharge # 19112 is an exceptional improved H-mode in that it was run at high density and very high heating power. Most improved H-modes are performed at densities  $\approx 4 - 5 \times 10^{19} m^{-3}$  for which O-mode polarization only gives core coverage and X-mode polarization covers only the plasma SOL.



(a) The time traces of plasma parameters in discharge # 19112.

(b) The evolution of the minimum edge  $E_r$  in an improved H-mode discharge.

Figure 7.2: The transition to lower  $E_r$  corresponds with an improvement in plasma confinement. The lowest  $E_r$  is measured during the improved H-mode phase.

The right-hand side of figure 7.2 shows the minimum values in edge  $E_r$  as a function of time in the discharge. The values correspond to roughly  $\rho_{pol} \approx 0.95$  and are obtained at times indicated by blue arrows in the time traces. Until 3.5s in the discharge,  $E_r$  is relatively stable and then a drop in  $E_r$  occurs. The  $E_r$  peak value decreases to -480V/cm, linked to an increase in confinement ( $H_{98}$ ) and plasma stored energy as seen in the time traces. Eventually the stored energy and confinement drop to their lower levels and likewise, the peak  $E_r$  also returns to its previous higher values of around -300 V/cm. Interestingly, the absolute magnitude of the edge  $E_r$  does not seem appear sensitive to the amount of NBI power. Its dependence on heating power will be described in the next section.

The experimental data indicate that the depth of the  $E_r$  well at the plasma edge increases with improved plasma confinement. This can be seen in figure 7.3 which shows for a variety of LSN discharges on ASDEX Upgrade the measured minimum  $E_r$  values at approximately  $0.96 \rho_{pol}$ , coinciding with the pedestal position. This data was acquired using the Doppler reflectometer and is plotted versus the H/L scaling factor,  $H_{98}$ . The scaling factor gives a good indication of the overall plasma confinement since it includes all effects related to confinement such as the plasma stored energy. Ohmic and L-modes have low H/L factors around 0.4 to 0.6. At this poor confinement, the depth of  $E_r$  is stable at about -50V/cm. At  $0.65 H_{98}$ , a bifurcation in  $E_r$  occurs as its depth drops rapidly to values ranging between -250 and -350V/cm. These greater depths are found purely in H-mode discharges. Another decrease in  $E_r$ , although less dramatic, is observed at  $0.95 H_{98}$ , marking the transition between H-modes and the higher confined improved H-modes.

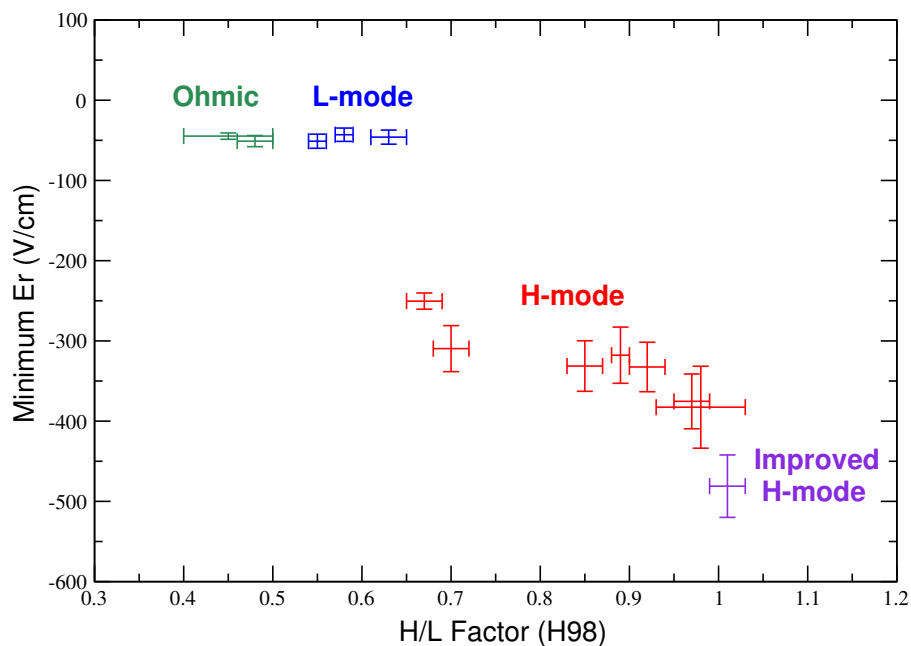


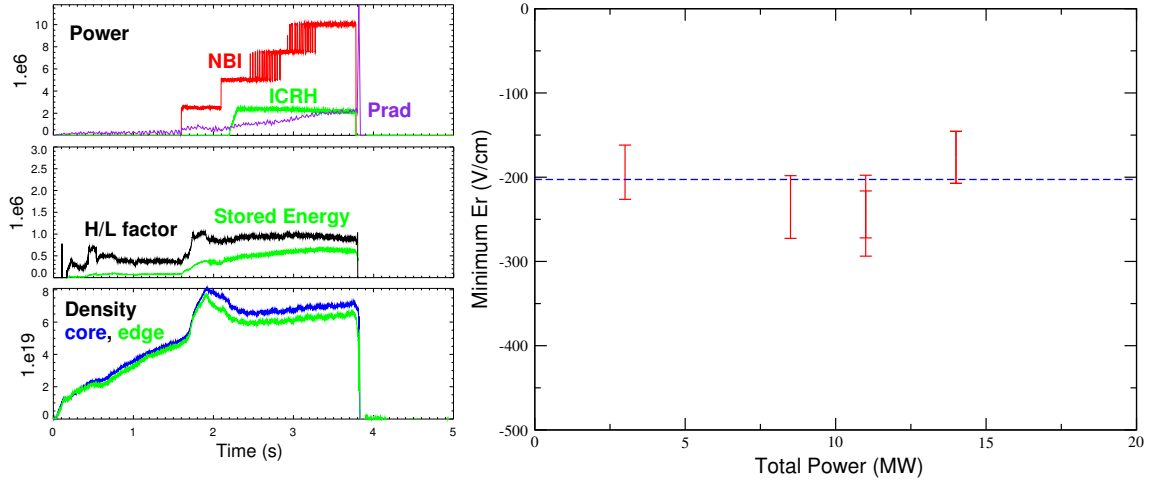
Figure 7.3: The dependence of edge  $E_r$  on plasma confinement, where  $E_r$  is the minimum value and confinement is measured by the H/L factor. The data are taken from several LSN discharges between # 17439 and # 19112. A clear bifurcation in  $E_r$  is observed.

The figure clearly demonstrates the relationship between the edge radial electric field and plasma confinement. The depth of the  $E_r$  well changes dramatically with confinement although no distinct variation in the width of the well is observed. Research is ongoing to determine the source of this enhanced  $E_r$  well although it appears to be related to an increase in the pressure gradient at the edge and hence a higher diamagnetic velocity  $v^*$  contribution to  $E_r$ . (Previously, in figure 6.2, it was shown that at the plasma edge  $v^*$  is the main contributor to  $u_\perp$  and hence  $E_r$ .) This could explain why the depth of the  $E_r$  well is relatively stable within each scenario (i.e. Ohmic, L-mode or H-mode) where the pressure gradient is unchanged within these scenarios and only undergoes a bifurcation at the L-H transition, where  $\nabla P$  changes dramatically due to the steep gradients in the edge H-mode density and temperature profiles. It is unclear at the moment whether the improved confinement in improved H-modes is also due to an increase in pressure gradient [80]. However, if the observed trend is correct, then the data in figure 7.3 indicates that the edge pressure gradient should increase slightly in the improved H-mode phase.

### 7.1.2 Dependence on Plasma Heating

Between the H-mode and improved H-mode phases in figure 7.1, there is an increase in NBI heating power, from 12.4MW to 15MW. The toroidal momentum created from the tangential NBI is recognized as a driving force of the radial electric field. Hence, to determine the role of NBI heating, the behaviour of  $E_r$  in USN discharge # 19424 was examined. This discharge has

a high  $\beta_N$  with NBI power steps ranging from 2.5MW to 10MW. As well, a constant 2.5MW of ICRH power is applied in the discharge. The time traces of several plasma parameters, including heating power, may be seen on the left-hand side of figure 7.4.



(a) The time traces of plasma parameters in discharge # 19424.

(b) The radial electric field as a function of plasma applied heating power.

Figure 7.4: The data was obtained during discharge # 19424 at normalized radius  $\rho_{pol} \approx 0.95$ . It shows that  $E_r$  has no obvious dependence on the amount of auxiliary heating.

The right-hand side of the figure shows the depth of the  $E_r$  well at  $\rho_{pol} \approx 0.95$  measured in discharge # 19424 as a function of total heating power. The measurement points are all obtained in the H-mode phase with similar confinement properties. Between 2.5MW to 12.5MW total applied heating power, no significant variation in  $E_r$  is detected. The depth of  $E_r$  is stable around -200V/cm. This magnitude is smaller than typical LSN H-modes which have edge  $E_r$  values of -300V/cm. This difference arises from the dependence of  $E_r$  on plasma shape (i.e. USN or LSN) and will be discussed in the following section.

There is a minimum input power threshold for achieving H-modes. In ASDEX Upgrade it is generally about 2.5MW of power for LSN discharges. The critical parameter appears to be the power flow across the separatrix rather than the total heating power [81, 82]. The temperature and its gradient in a plasma are believed to be important in determining the power threshold but the ion temperature at the transition is always constant regardless of the total power [81, 83]. Hence, it appears that once the H-mode has been obtained, the total heating power is not significant in either determining the radial electric field structure in a plasma nor in determining the confinement. The observation that the minimum edge  $E_r$  remains constant in H-modes with auxiliary heating power between 2.5MW and 12.5MW confirms that the depth of the  $E_r$  well is mainly affected by changes in the edge pressure gradient,  $\nabla P$ . Although the *total* amount of heating power does not appear to play a key role, this still leaves open the

question whether the *type* of heating power applied affects the radial electric field.

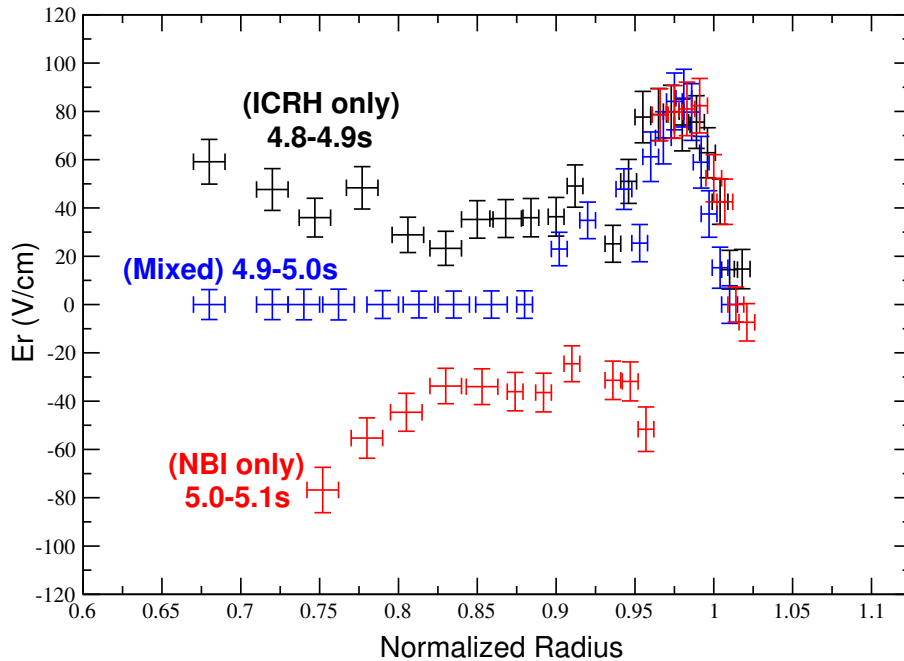


Figure 7.5: Evolution of the radial electric field from an ICRH phase (4.8-4.9s) to an NBI phase (5.0-5.1s) in L-mode discharge #18952. The data was collected in X-mode polarization.

Unlike active charge exchange spectroscopic techniques, the Doppler reflectometer diagnostic is capable of  $E_r$  measurements in all three types of auxiliary heating power: NBI, ICRH and ECRH. It is interesting to understand if ICRH can be a means to control  $E_r$ . Figure 7.5 compares edge  $E_r$  profiles obtained in LSN discharge #18952 ( $B_\phi = +2T$ ,  $I_p = -0.6MA$ ) using NBI and ICRH heating methods. The data was collected using X-mode polarization with a frequency pattern of 1GHz steps between 50 and 74GHz in 100ms. In the discharge, between 4.8 to 4.9s, 1.6MW of pure ICRH heating is applied. At 4.95s, 2.5MW NBI heating is additionally applied and soon after at 5.0s, the ICRH power is switched off so that only pure 2.5MW NBI heating exists between 5.0 to 5.1s. The difference between the two heating methods is immediately evident in the  $E_r$  profiles of figure 7.5. Around the separatrix, the  $E_r$  profiles are positive. The  $E_r$  from the phase with NBI heating (shown in red) then becomes negative as the diamagnetic velocity (i.e. the main contributor to  $E_r$  at the plasma edge) is positive (see figure 6.5 and note that  $E_r = -u_\perp \times B$ ). In the plasma mid-core, the  $E_r$  remains negative as the poloidally mapped toroidal velocity  $v_\phi B_\theta / B$  (i.e. the main contributor to  $E_r$  in the plasma core) is positive in counter-NBI discharges (see discussion in section 6.4). The overall plasma rotation with pure NBI heating is in the counter-current direction. However, when pure ICRH heating is applied, the measured  $E_r$  (shown in black) becomes positive in the plasma mid-core, indicating that a negative poloidally mapped toroidal rotation exists there. The overall plasma rotation is now in the co-current direction. This observation agrees with what was seen in JET

[84] and Alcator C-Mod [85] in which plasmas rotate in the co-current direction with ICRF as the sole additional heating. The mechanism for the observed co-rotation is still unresolved but several theories associated with large drift orbits exist [86].

A combination of both heating power methods (shown in blue) results in a cancellation of the radial electric field in the plasma mid-core. Previous experimental measurements on ASDEX Upgrade, using the charge exchange diagnostic, have shown that ICRH heating causes a reduction of  $v_\phi$  driven by NBI in the co and counter-current directions [78]. A reduction in  $v_\phi$  by a factor of two in counter-NBI discharges is detected and is attributed to an increasing momentum diffusivity connected with the confinement degradation by the additional ICRH power flux [78]. (Confinement degradation is the same mechanism used to explain the reduction in  $v_\phi$  due to pure electron heating with ECH in DIII-D [87].

The experimental measurements in figure 7.5 show that pure ICRH heating may induce toroidal rotation. Previously, only toroidally oriented neutral beam injection NBI was thought to generate toroidal rotation.

### 7.1.3 Dependence on Plasma Shape

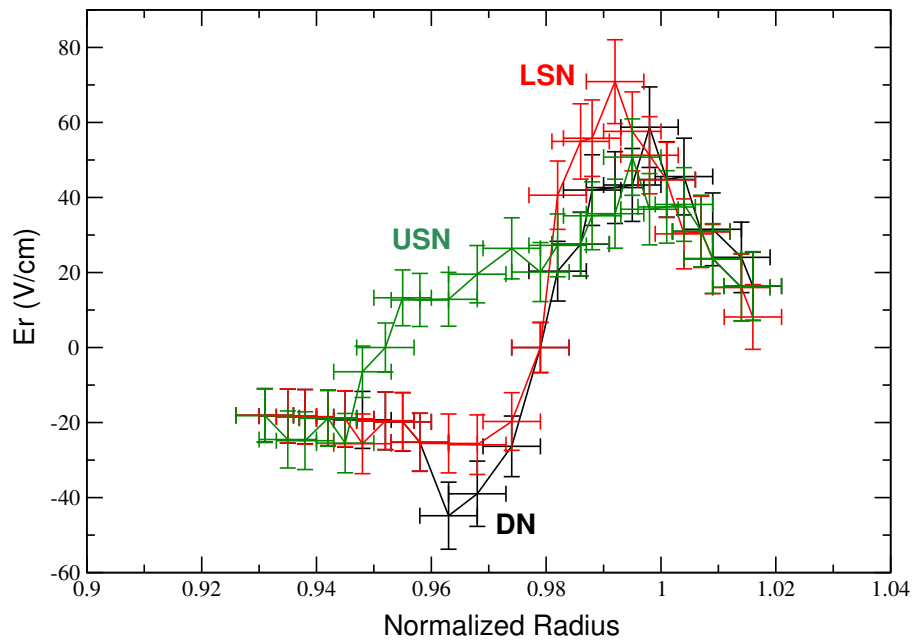


Figure 7.6: *The radial electric field profiles of discharge # 19415 measured during various plasma shapes: LSN (3.0s), DN (4.4s), USN (5.8s). The absolute  $E_r$  and its shear are smaller in USN shaped plasmas.*

Another factor which is known to affect confinement and hence the radial electric field is the shape of the plasma [89]. In a pure heated 1.3MW ICRH discharge # 19415 ( $B_\phi = -2T, I_p = +0.8MA$ ), the plasma shape was altered from lower single null (LSN) to double null (DN) and then to upper single null (USN). In table 2.3, the shapes and their parameters for this

particular discharge are given. The Doppler reflectometer was set in X-mode configuration (due to the low density in the discharge of  $4.0 \times 10^{19} m^{-3}$ ) with a frequency pattern of 1GHz steps between 50 and 74GHz in 100ms. The electron density profile, from which the radial positions are obtained, is a best fit to the DCN line interferometry and edge Thomson scattering data.

Figure 7.6 shows the  $E_r$  profiles with L-mode conditions for the three plasma shapes. A positive radial electric field is measured in the SOL/separatrix region in all profiles due to the fast open flux surface connection to the divertor but, the formation and depth of the  $E_r$  well around the pedestal depends strongly on the plasma shape. The DN configuration has the lowest edge  $E_r$  of -44.8V/cm at  $\rho_{pol} = 0.96$ , followed by the LSN configuration with -25.6V/cm at the same position. The  $E_r$  measured in the USN configuration, however, is still positive at the plasma edge at  $\rho_{pol} = 0.96$  and only makes the transition to negative  $E_r$  at  $\rho_{pol} = 0.95$ .

Figure 7.7 shows the minimum  $E_r$  at  $\rho_{pol} \approx 0.96$  in discharge # 19415 as a function of time. The depth of the  $E_r$  well decreases as the plasma moves from a LSN shape to a DN shape and then increases when the plasma has an USN shape.

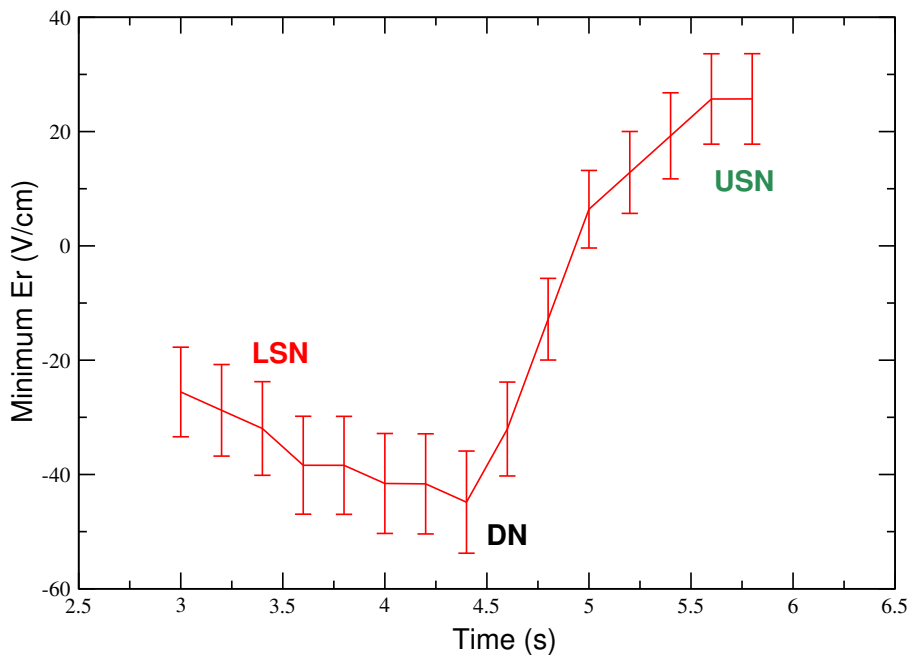


Figure 7.7: The evolution of the minimum edge radial electric field measured in discharge # 19415. The lowest  $E_r$  value was measured in a DN shaped plasma.

The behaviour observed can be explained by the impact the divertor configuration has on the parallel fluxes in the plasma. Rozhansky has undertaken modeling of the radial electric field in discharge # 19415 for the three plasma shapes using a B2SOLPS5.0 transport code [88]. He has found that the geometrical configurations change mainly the distribution of the parallel fluxes in the SOL and through the anomalous viscosity change the parallel fluxes in the viscous layer (i.e. the layer just adjacent to the separatrix where  $E_r$  changes in the three plasma shapes).

There are three contributions to the parallel fluxes in the SOL: the Pfirsch-Schluter PS flux (which closes the vertical  $\nabla B$  drift of ions), the flux compensating the  $\mathbf{E} \times \mathbf{B}$  drift in the radial electric field, and the parallel unbalanced flux (which is directed to the divertor target plates). Rozhansky's simulation work shows that in upper single null shaped plasmas, the divergences of the vertical  $\nabla B$  drift flux and parallel fluxes is smaller than in lower single null and double null shaped plasmas. This accounts for the divergence of  $E_r$  and its shear being small in USN shaped plasmas, as seen in the experiment.

Another possible explanation for the changes in  $E_r$  is the differences in plasma confinement. Figure 7.3 shows that between 0.6 and 0.7  $H_{98}$  factors, the change in the depth of the  $E_r$  well is greatest. This may be a reason why the lower confined USN discharge, with 0.59  $H_{98}$ , has a smaller  $E_r$  well than the LSN and DN configuration with  $H_{98}$  factors of 0.65.

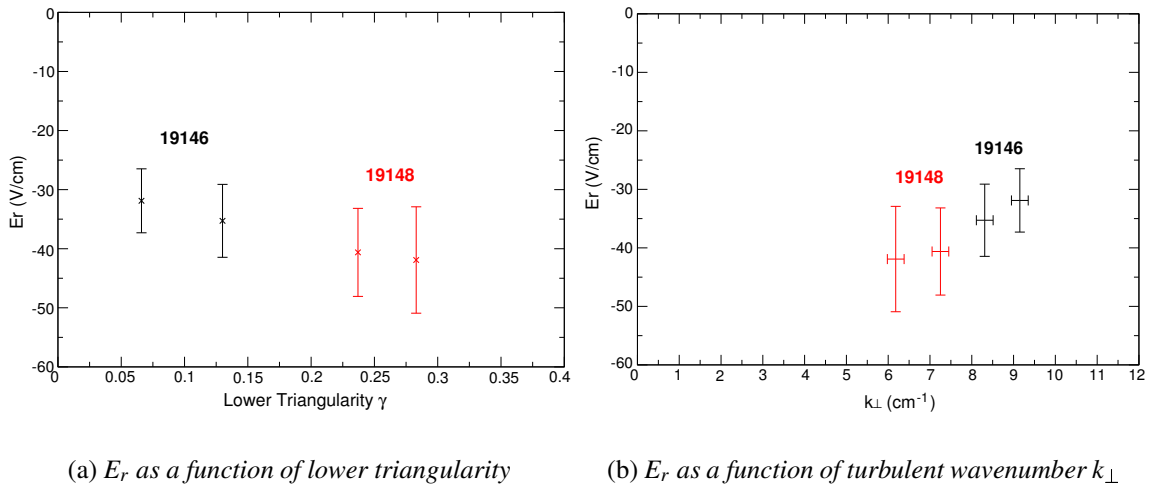


Figure 7.8: The radial electric field as a function of both lower triangularity and turbulent wavenumber calculated for the pair of USN L-mode discharges # 19146, # 19148.

To study the role of plasma shape and triangularity without the influence of plasma confinement, a triangularity ramp was performed in two USN L-mode discharges # 19146 and # 19148. All plasma parameters were held constant in these discharges. Figure 7.8 presents the relationship of  $E_r$  with plasma triangularity and the perpendicular wavenumber  $k_{\perp}$ .  $k_{\perp}$  is calculated by the Bragg equation  $k_{\perp} = 4\pi \sin \theta_{tilt} / \lambda_o$ , where  $\theta_{tilt}$  is the geometric tilt angle between the plasma flux surface normal and  $\lambda_o$  is the wavelength of the incident microwave. The  $E_r$  shows a slight dependence on both quantities, decreasing with triangularity and increasing with  $k_{\perp}$ . Measurements on JET and DIII-D show that the confinement time in a plasma depends strongly on plasma shape, improving with triangularity [89, 91]. The experimental results presented here offer supporting evidence of this observation, although with the newly planned tiltable antennae system on ASDEX Upgrade, this may be further investigated with the Doppler reflectometer in the near future.

### 7.1.4 Comparison with Modeled $E_r$ Profiles

To confirm how well Doppler reflectometry measures  $E_r$ , comparisons with models and CXRS measurements are helpful. This section describes two models used for comparing experimental Doppler reflectometry measurements.

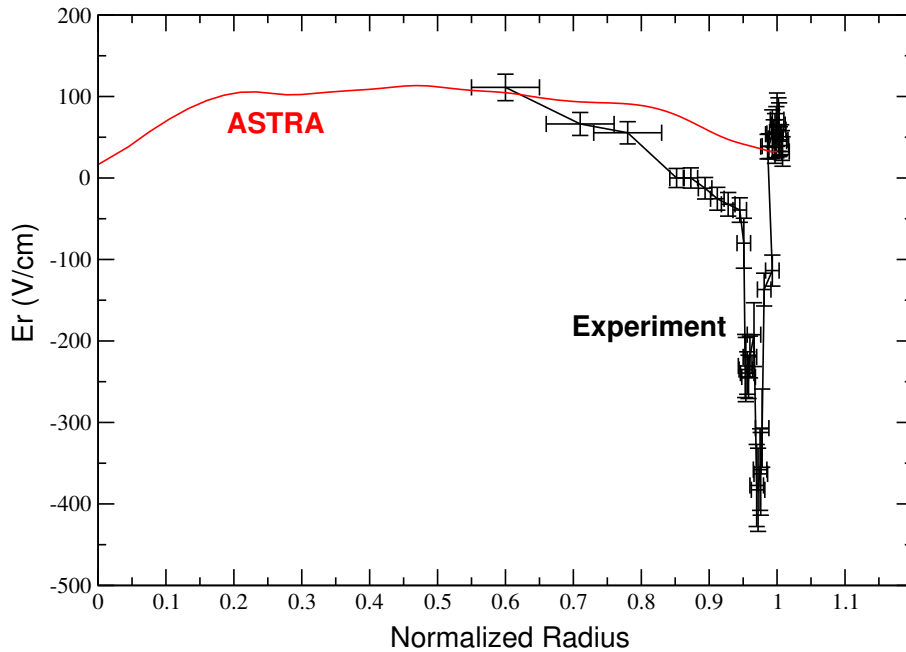


Figure 7.9: The radial electric field in a LSN H-mode discharge measured experimentally by Doppler reflectometry and modeled from ASTRA. There is agreement only in the plasma core.

The first example shows the modeling of  $E_r$  using the ASTRA (Automated System for Transport Analysis) code [92], which is a transport code used for particle and heat transport modeling and for stability analysis. The code is used here to model the radial electric field using neoclassical calculations and experimental plasma parameters. Figure 7.9 shows a comparison between a simulated  $E_r$  profile from ASTRA for H-mode discharge # 17439 at 2.2s with the corresponding  $E_r$  profile from the Doppler reflectometer. (The particulars of this discharge were previously described in chapter 6.) Although there is good agreement between code and experiment in the plasma core, the ASTRA code fails to reproduce the pedestal reversal or  $E_r$  well at the plasma edge. This is mainly because the code does not account for the steep edge gradients in both density and temperature, which result in a large diamagnetic velocity and hence a reversal in  $E_r$  at the plasma edge.

The second modeling effort discussed here is for a LSN Ohmic discharge # 18737 ( $B_\phi = -2T, I_p = +0.8MA$ ). In this case, the radial electric field at the edge is simulated by means of a B2-SOLPS fluid code [93, 94]. In the code, the most complete system of transport equations is solved including all  $E \times B$  drifts. By altering the drifts, a good match in both position and magnitude between the calculated  $E_r$  and measured  $E_r$  is found and is presented in figure 7.10.

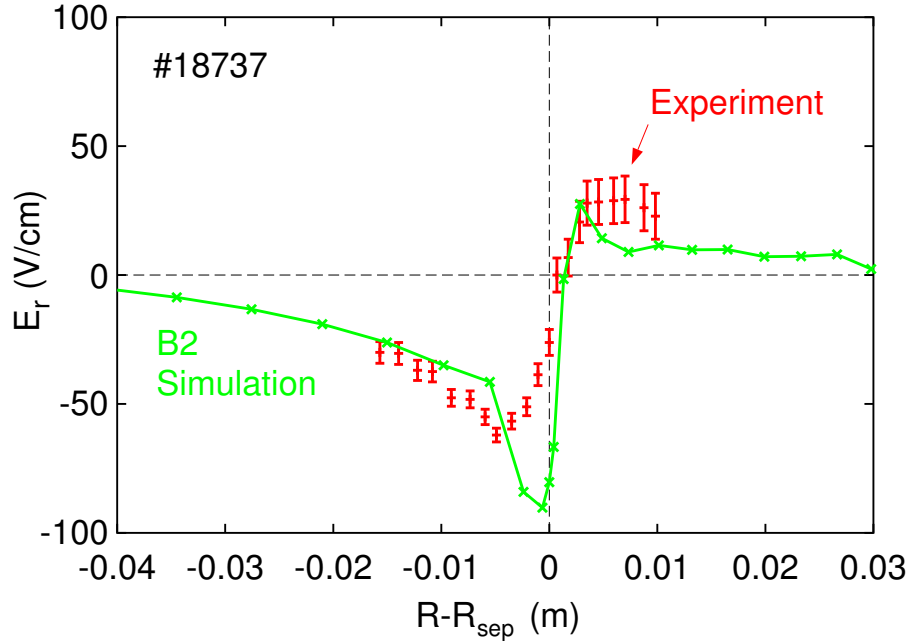


Figure 7.10: The radial electric field in a LSN ohmic discharge measured experimentally by Doppler reflectometry and modeled from B2. There is agreement at the plasma edge.

## 7.2 Measurements of the Radial Electric Field Shear

The radial electric field measurements from Doppler reflectometry show interesting behaviour of  $E_r$ , in particular by its dependence on confinement, heating power and plasma shape. Nevertheless, theory exists which predicts that the shear in  $E_r$  may be of greater importance in tokamak physics, especially in the stabilization of turbulence. Using the correlation Doppler reflectometer system and the techniques and analysis described in chapter 5, measurements of  $\partial E_r / \partial r$  are presented here for various plasma scenarios.

Figure 7.11 presents the radial electric field shear measured in an L-mode (# 18103 at 3.7s) and H-mode (# 17973 at 6.0s) LSN discharge. In both discharges, the two channels of the correlation Doppler reflectometer had a similar frequency launch pattern: 1GHz steps from 50 to 74GHz in 100ms with a 2GHz fixed frequency difference between the two channels. In the L-mode discharge, the data was obtained using X-mode polarization while in the H-mode discharge, O-mode polarization was used. The polarization was chosen for edge measurements in both discharges.

In comparing the shear measured in the two discharges, three observations can be made. First, the shear is localized at the plasma edge and zero elsewhere. It has both a positive peak and a negative well. Second, the H-mode  $E_r$  shear profile is shifted inwards in comparison to the L-mode profile. This may be due to the density pedestal which steepens and moves inwards during an H-mode [19]. This is seen when comparing the experimental density profiles obtained by DCN, standard reflectometry and core Thomson scattering diagnostics in both discharges. The third observation is that the absolute value of the edge  $E_r$  shear increases

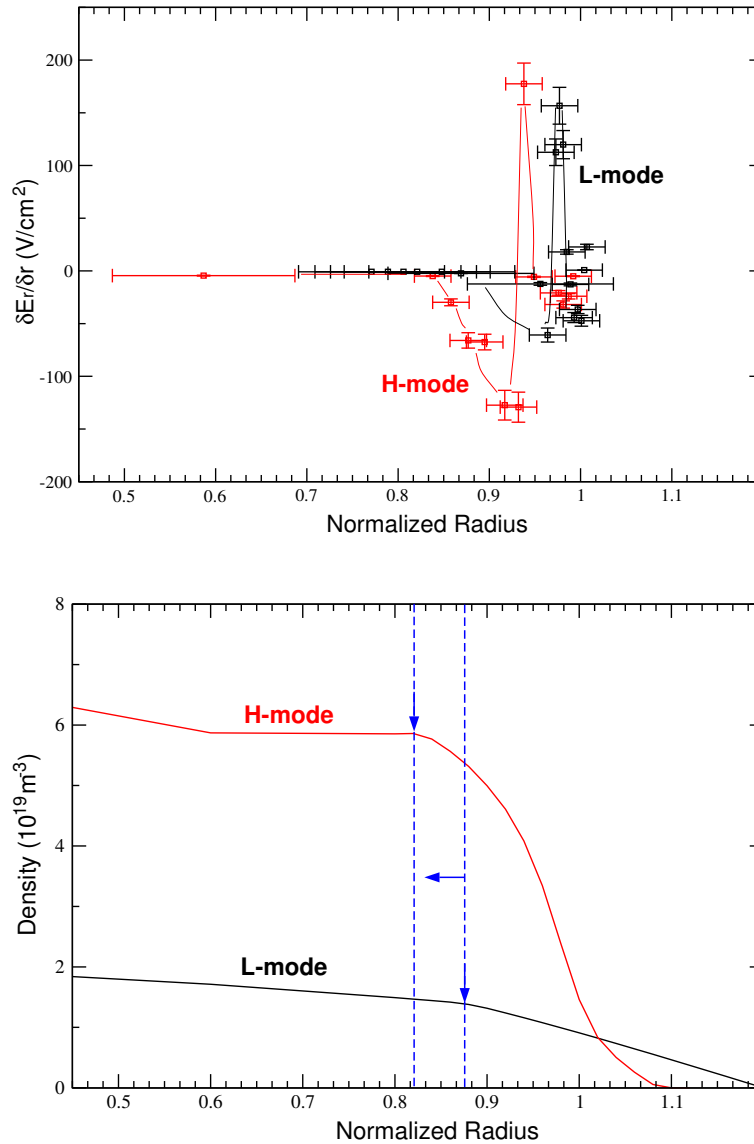


Figure 7.11: The radial electric field shear measured during L-mode (# 18103) and H-mode discharges (#17973). The experimental electron density profile steepens and moves inwards during an H-mode, accounting for the radial shift in the  $E_r$  shear profiles.

after the L-H transition. Typically at ASDEX Upgrade the maximum negative edge  $E_r$  shear measured in L-modes is between 0 and  $-75\text{V/cm}^2$  (see figure 7.12 for examples of further shear measurements in L-mode discharges) and in H-modes between  $-150$  and  $-250\text{V/cm}^2$ . This enhanced shear in H-mode is observed for all types of H-modes, i.e. NBI heated, ICRH, etc.

Figure 7.13 shows the shear measured on ASDEX Upgrade during a quiescent H-mode phase.

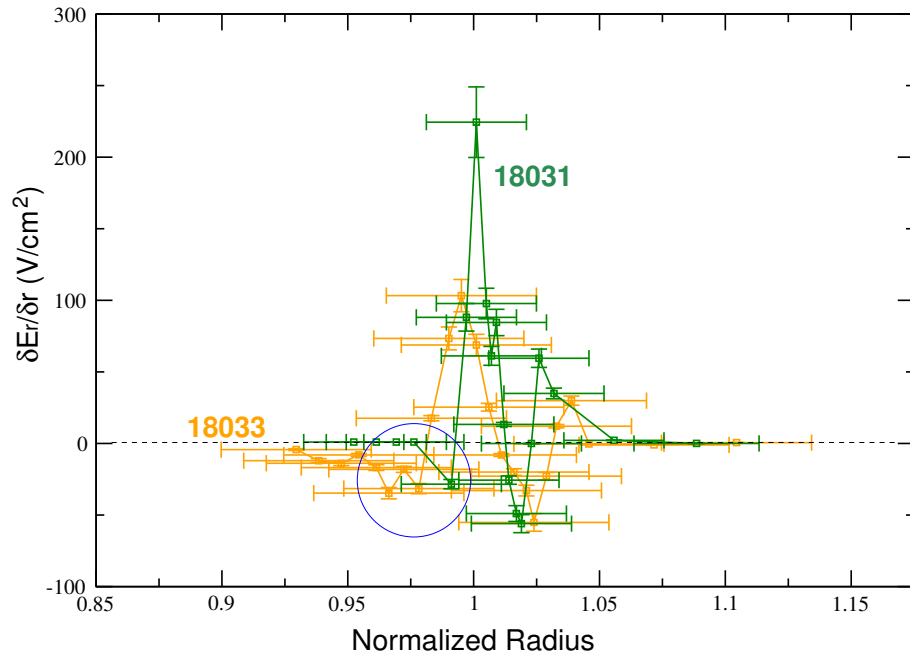


Figure 7.12: The radial electric field shear measured in LSN L-mode discharges (# 18031, 2.1s and # 18033, 3.4s) using the correlation Doppler reflectometer system with X-mode polarization. The negative shear is small, approximately  $-25V/cm^2$ .

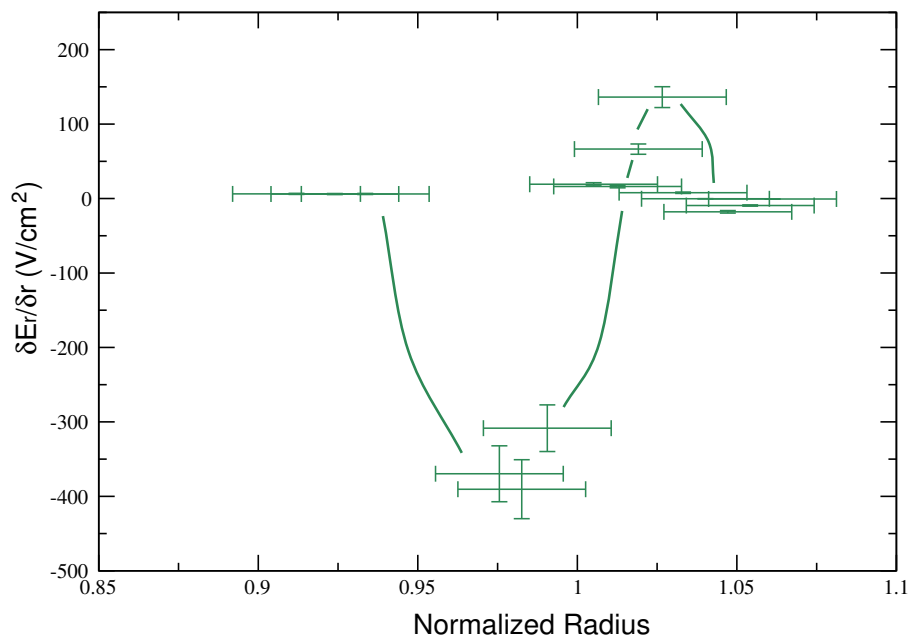


Figure 7.13: The radial electric field shear measured during a quiescent H-mode discharge # 18925 at 3.5s. The largest absolute  $E_r$  shear measured on ASDEX Upgrade to date has been during the quiescent H-mode discharges.

The quiescent H-mode phase, like the ELMy H-mode, has very high confinement but is ELM-free. The data was collected with the usual frequency launch pattern and in X-mode polarization due to the low plasma densities. In ASDEX Upgrade, the highest shear measured to date has been during the quiescent H-mode phase. It has been suggested by Burrell [24] that the strong shear (greater than  $-400 \text{ V/cm}^2$ ) in this plasma regime may be an explanation for the observed ELM stabilization.

The  $E_r$  shear measurements all show that the positive shear at the plasma edge is relatively unchanged ( $\approx -150$  to  $-200 \text{ V/cm}^2$ ) for a variety of discharges. This shear is associated with the plasma separatrix/SOL region. It is rather the negative shear, linked to the plasma pedestal region, that appears more influential with changes ranging from almost zero to  $-400 \text{ V/cm}^2$ . In Itoh's model, it was found that the shear flips from being small and positive in L-mode to large and negative in H-mode and it is the jump in  $E_r$  shear which is responsible for confinement improvement [95]. Apparently, the small negative shear in L-modes which were seen in the Doppler reflectometer measurements are not accounted for in Itoh's model. In Shaing's model, turbulence stabilization occurs primarily for  $E_r$  shear greater than zero [49]. Again, this model does not represent the experimental  $E_r$  shear measurements since the role of the negative shear is dominant. The Biglari, Diamond and Terry (BDT model) predict that an increase in absolute shear suppresses density fluctuations and stabilizes the turbulence [8]. Turbulence stabilization may occur for either sign of  $\partial E_r / \partial r$  in this model. The data shown in figure 7.11 is consistent with their model.

### 7.3 Summary

Radial electric field and shear measurements were performed on ASDEX Upgrade using the newly developed correlation Doppler reflectometer system. Both these parameters,  $E_r$  and  $\partial E_r / \partial r$ , are thought to play a major role in the suppression of plasma turbulence and hence their measurements are much sought after. Generally, the radial electric field in a plasma is measured using active charge exchange spectroscopy (CXRS) and the radial force balance equation. This method relies on accurate poloidal and toroidal rotation measurements from CXRS as well as accurate electron or ion densities and temperatures for calculation of the electron or ion diamagnetic velocity. Due to the strong gradients in density and temperature at the plasma edge, accurate measurements are difficult to achieve and diagnostics need to be specially developed for such measurements. For example, on ASDEX Upgrade, the lithium beam diagnostic was recently adapted for measuring edge ion temperatures. The Doppler reflectometer can bypass all these obstacles since the perpendicular velocity which it measures is directly related to  $E_r$ . By using a second Doppler reflectometer channel (i.e. correlation Doppler reflectometry), the measurement of instantaneous  $E_r$  shear is possible.

The  $E_r$  profile in a standard ASDEX Upgrade plasma configuration, with  $-B_\phi, +I_p$ , is positive in the SOL and then undergoes a reversal at the plasma edge, coinciding with the plasma pedestal region. This reversal forms what is known as an  $E_r$  well. The depth of the well is observed to increase dramatically with the confinement of the discharge (see figure 7.3) while the width of the well appears unaffected. The edge pressure gradient  $\nabla P$  is most likely

the influential factor in determining the depth of the  $E_r$  well. The pressure gradient becomes steeper at the edge in H-mode (in comparison with L-mode and ohmic discharges) due to the steeper gradients in density and temperature. Once an H-mode is obtained, the amount of total auxiliary heating power does not affect the  $E_r$  well depth. This supports that  $\nabla P$ , which remains relatively constant in H-modes, is the influential factor in determining the depth of the  $E_r$  well.  $\nabla P$  is limited by MHD stability criterion, that is, a certain edge current density can only support a certain plasma pressure otherwise it becomes kink unstable. The  $E_r$  profile, however, is altered by the type of heating power applied. In counter-current pure NBI heated discharges,  $v_\phi B_\theta/B$  is in the counter-current direction while in pure ICRH heated discharges, it is in the co-current direction. Hence, the  $E_r$  profiles in figure 7.5 have opposite signs. The results indicate that ICRH heating may drive toroidal rotation, although when it is added to NBI heating, it reduces  $v_\phi$ . This reduction can be explained by an increase in momentum diffusivity connected with the confinement degradation by the additional ICRH power flux [78]. The dependence of  $E_r$  on plasma shape was also investigated in this thesis work. It was found that the shape does have a strong influence on the edge  $E_r$  profiles. USN shaped plasmas have smaller absolute  $E_r$  magnitudes than LSN shaped plasmas. Simulation work by Rozhansky has shown that the divertor configuration changes the parallel fluxes in the SOL and edge, resulting in a difference in  $E_r$  [88].

The  $E_r$  shear measurements have shown the importance of accurate electron density measurements since  $\partial E_r/\partial r$  depends heavily on  $r$ . The  $E_r$  shear profiles are localized at the plasma edge, being small elsewhere. Measurements in L-modes, H-modes and quiescent H-modes show that the positive shear at the plasma edge is relatively constant but the amount of negative shear changes, depending on the plasma confinement. The results are summarized in table 7.1. In comparing the experimental measurements to the global aspects of various theories about  $E_r$  shear, it was found that the BDT model agrees best with the trend observed in the measurements.

Type of Discharge	Edge $\partial E_r/\partial r$ (V/cm <sup>2</sup> )
L-mode	0 to -75
H-mode	-150 to -250
Quiescent H-mode	-400 to -500

Table 7.1: Typical edge  $E_r$  shear measurements on ASDEX Upgrade.



# Chapter 8

## Radial Correlation Length of the Turbulence

The radial correlation length of the turbulence,  $L_r$ , has in the past been measured using a variety of diagnostics, the most common being correlation reflectometry [34, 36, 96, 97, 98]. However, there has been divergence concerning not only how  $L_r$  is determined but also how it is defined [35, 37, 73, 99]. Nevertheless, researchers are striving to measure  $L_r$  since it contains valuable information about the type of turbulence existent in the plasma and its behaviour. For the first time, Doppler reflectometry has been utilized for obtaining  $L_r$  measurements as part of this thesis work. While many of the experimental results agree with theory, one in particular, namely the dependence of  $L_r$  on the turbulent wavenumber  $k_\perp$ , revealed an unexpected result. This motivated an investigation using a two-dimensional Finite Difference Time Domain (FDTD) code to simulate the Doppler reflectometer response and to recreate the experimental  $L_r$  measurements. This chapter presents experimental  $L_r$  measurements from Doppler reflectometry with a comparison to theory, to the measured  $L_r$  in other tokamaks using standard correlation reflectometry and to the  $L_r$  obtained from the 2D code with the aim of examining how well the diagnostic determines the true turbulent  $L_r$ .

### 8.1 Experimental Measurements

#### 8.1.1 Radial Correlation Lengths in L-mode and H-mode

The  $u_\perp$ ,  $E_r$ , and  $E_r$  shear measurements show a marked difference at the plasma edge between L-modes and H-modes. Several theories exist, such as the oft-cited Biglari Diamond and Terry (BDT) model [8], which claim that an increase in absolute  $E_r$  shear should lead to a decorrelation of the turbulence. Since the radial correlation length of the turbulence gives a measure of the spatial size of a turbulent perturbation, this means that in the region of high  $E_r$  shear (i.e. H-mode pedestal region),  $L_r$  may be reduced.

Figure 8.1 shows a comparison of the complex coherence  $\gamma$  measured in an L-mode and an H-mode at  $\rho_{pol} \approx 0.98$ . Taking the distance over which the coherence has dropped to a value

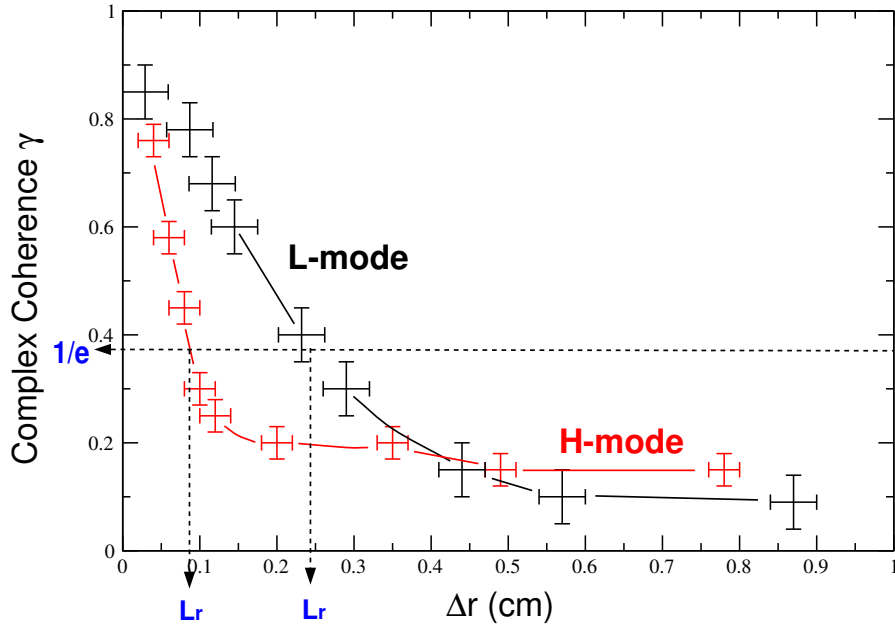


Figure 8.1: Complex coherence measured during L (# 18761,  $k_{\perp} = 9.56 - 10.2\text{cm}^{-1}$ ) and H-mode (# 18749,  $k_{\perp} = 6.6 - 7.1\text{cm}^{-1}$ ) discharges at  $\rho_{pol} \approx 0.98$ .

of  $1/e$ , a correlation length of  $0.24\text{cm}$  in L-mode and  $0.09\text{cm}$  in H-mode is obtained. In the DIII-D tokamak, radial coherence lengths of the density fluctuations, measured by standard correlation reflectometry, show changes from roughly  $0.4\text{cm}$  in L-mode to  $0.2\text{cm}$  in H-mode at the same normalized radius [41]. Both the ASDEX Upgrade and DIII-D results show the edge radial correlation length decreasing to at least half its value after the L-H transition. In the ASDEX case, this coincides with an increase in the  $E_r$  shear measured there (see figure 7.11). The experimental link made between an increase in  $E_r$  shear and decrease in  $L_r$  agrees well with the BDT model.

### 8.1.2 $L_r$ as a Function of Plasma Normalized Radius

Turbulence measurements have shown that density fluctuation levels are far higher at the plasma edge than in the core [55]. Likewise, the  $E_r$  shear profiles presented in the previous chapter show large varying values at the plasma edge but dropping to negligible values in the mid-core region. Hence, the higher shear and fluctuation levels indicate a highly turbulent edge region of the plasma and a more quiescent core region.  $L_r$  measurements in the plasma edge and core regions should show a similar trend since turbulent fluctuation levels,  $E_r$  shear and  $L_r$  are all linked in the BDT model.

Figure 8.2 shows how  $L_r$  varies with plasma position. The data are from the early L-mode phases of ASDEX Upgrade's standard NBI-heated H-mode discharges. All plasma parameters were constant during the time the Doppler correlation was measured in O-mode polarization. Note that the radial positions of the core measurements (i.e. in # 19380 and # 18739) were

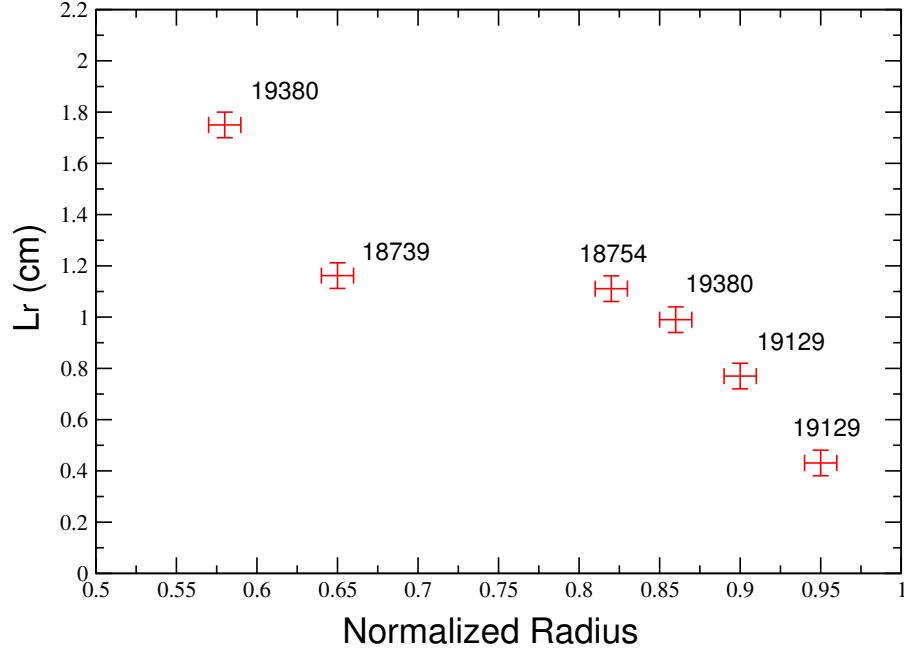


Figure 8.2:  $L_r$  measured as a function of normalized radius during L-mode phases in ASDEX Upgrade's standard H-mode discharges (#18739-19380).

corrected using the TORBEAM beam-tracing code to account for the large beam refractive effects in the plasma core. The figure shows  $L_r$  increasing into the plasma core, ranging from about 0.40cm at  $\rho_{pol} \approx 0.95$  to 1.75cm at  $\rho_{pol} \approx 0.58$ . The magnitude of  $L_r$  is similar to those measured on DIII-D using a standard correlation reflectometer ( $k_{\perp}=0$ ) [36]. The increase of  $L_r$  into the plasma core confirms its link to  $E_r$  shear and turbulent fluctuation levels. The magnitude of  $L_r$  also provides details on the type of turbulence existent in the plasma. The results indicate that smaller turbulent structures exist at the plasma edge in comparison with the core.

### 8.1.3 The Relationship Between $L_r$ and $k_{\perp}$

Of particular interest is the relationship between  $L_r$  and the turbulent wavenumber  $k_{\perp}$ . This can be examined with the correlation Doppler system since the tilted antennae of a Doppler reflectometer probe a non-zero turbulent wavenumber,  $k_{\perp}$ . The wavenumber is given by the Bragg equation:  $k_{\perp} = 4\pi \sin \theta_{tilt} / \lambda_o$ , where  $\theta_{tilt}$  is the geometric tilt angle between the plasma flux surface normal and the incident microwave beam and  $\lambda_o$  is the wavelength of the incident microwave. The antennae on ASDEX Upgrade are fixed so to vary the tilt angle and hence,  $k_{\perp}$ , the plasma shape is scanned from low to high triangularity. This was performed in two similar L-mode upper single null discharges (#19146 and #19148) and the results are shown in figure 8.3. Figure 8.3 shows  $L_r$  increasing with  $k_{\perp}$ . This is a surprising result since simple theory would argue that higher  $k_{\perp}$  means smaller probed turbulent wavelengths  $\Lambda_{\perp}$  which should

coincide with smaller structure size and hence smaller radial correlation lengths. This simple argument is of course based on the assumption that the turbulence is isotropic; its structures have equal dimensions in the transverse (i.e. poloidal) and radial directions. A literal physics interpretation of figure 8.3 would be that smaller probed  $\Lambda_{\perp}$  have longer radial dimensions (i.e. the turbulence is anisotropic). In this case, the narrower the density fluctuations are poloidally, the more they are stretched radially.

There are several other possible explanations for this unexpected trend. For example, by changing the plasma shape, the nature of the edge turbulence may be changed. Previous measurements show that the radial electric field and its associated shear changes with plasma shape (see figure 7.8). The varying shear as a function of  $k_{\perp}$  could vary the amount of deformation of the turbulent structures and hence,  $L_r$ . Another possibility is that the Doppler reflectometer is not measuring  $L_r$  alone but rather in addition some other component such as the poloidal correlation length  $L_p$ . To remove the shape dependence, one would need to repeat the experiment with tiltable antennae, allowing the measurement to be performed under constant plasma conditions. This is planned for the following experimental campaign on ASDEX Upgrade when the construction of the new tiltable antennae will be complete. However, to test the  $L_p$  and  $L_r$  interdependence, one could simulate the reflectometer response with the overall goal to recreate the  $L_r$  experimental measurements and in particular, examine the dependence of  $L_r$  on  $k_{\perp}$ . The model used along with its results are described in the following section.

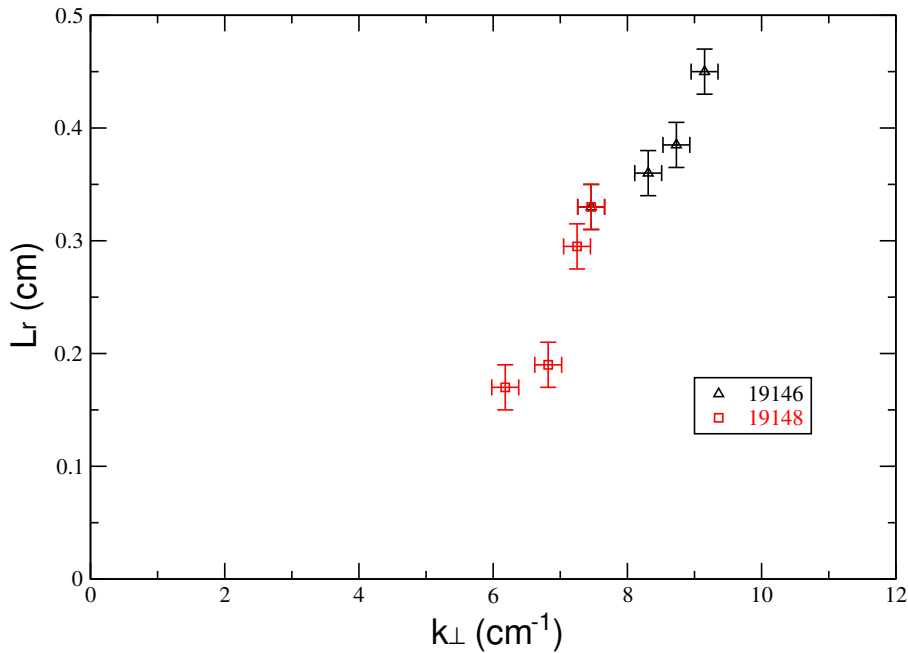


Figure 8.3: *Dependence of radial correlation length edge measurements on the perpendicular wavenumber. The measurements were obtained in a pair of USN L-mode discharges.*

## 8.2 2D Full Wave Simulation of Doppler Reflectometry

Modeling of the reflectometer response has been an important aspect of the diagnostic development since the beginning, not only to aid interpretation but also for its predictive capabilities in assisting the design of future devices, etc. [100] In particular, for the design of the next fusion device ITER, discussions are ongoing as to what role reflectometry will play. Simulations which show what key measurements are possible with such a system are very valuable for these discussions. Over the years, several codes have been developed, two of the more popular being the Born approximation code and the two-dimensional full-wave code [101]. Both have their advantages and their disadvantages. The Born approximation code, however, is mainly used when small density fluctuations exist. Generally, this is not valid at the plasma edge where the density fluctuation level could reach up to 25%. The 2D full-wave code, although more time consuming, provides a more complete simulation when fluctuation levels are high. As part of this thesis work, a 2D full-wave code in the extraordinary mode has been adapted to simulate Doppler reflectometry in the ASDEX Upgrade tokamak and recreate the experimental results in figure 8.3. The equations in the 2D full-wave numerical code are presented in the next section. A description of the experimental parameters and modeled turbulence required in the code and the the results of the simulation are given in the following sections.

### 8.2.1 The 2D Finite Difference Time Domain Full Wave Code

For X-mode propagation in a plasma, the Maxwell equations of interest are:

$$\frac{\partial B_x}{\partial t} = -\frac{\partial E_z}{\partial y} \quad (8.1)$$

$$\frac{\partial B_y}{\partial t} = \frac{\partial E_z}{\partial x} \quad (8.2)$$

$$\mu_o \epsilon_o \frac{\partial E_z}{\partial t} = -\mu_o j_z + \frac{\partial B_y}{\partial x} - \frac{\partial B_x}{\partial y} \quad (8.3)$$

where the electric field of the wave is in the  $z$  direction and the magnetic field lies in the  $xy$  plane. The constants  $\mu_o$  and  $\epsilon_o$  are the permeability and permittivity of free space respectively. Note that the current density  $\mathbf{j}$  term (defined in equation 4.9) is included to account for the dynamic response of the electrons in the plasma to the electric and magnetic fields introduced by the electromagnetic wave. Under the assumption of a cold plasma ( $T_e = 0$ ), the equation for the current density is:

$$\frac{\partial j_z}{\partial t} = \epsilon_o \omega_p^2 E_z - \omega_c j_x + \omega_c j_y \quad (8.4)$$

where  $\omega_p$  and  $\omega_c$  are the familiar terms for plasma frequency (4.16) and cyclotron frequency (4.17).

Equations 8.1 to 8.4 need to be solved self-consistently. This can be achieved with a finite-difference time-domain (FDTD) algorithm developed by Blaschak and Kriegsmann [102]. An

approximate solution to the above Maxwell equations (8.1-8.3) is achieved by first discretizing the set of equations into a finite difference rectangular grid of dimensions  $(\Delta x, \Delta y)$  and then explicitly integrating the equations forward in time at discrete time steps  $(\Delta t)$ . In the 2D full-wave code, the variables used are  $\Delta x = \Delta y = \lambda_o/25$  and  $\Delta t = \tau/25$  where  $\lambda_o$  is the vacuum wavelength of the wave corresponding to a microwave frequency of 61GHz and  $\tau$  is its period. These parameters were chosen as a compromise between computational time and dispersion introduced artificially in the grid from the discretization process [101]. The output of the code includes the Doppler reflectometer In-phase ( $I$ ) and Quadrature ( $Q$ ) reflectometer signals, from which the Amplitude ( $A$ ) and Phase ( $\phi$ ) signals may be calculated.

## 8.2.2 The Input Parameters

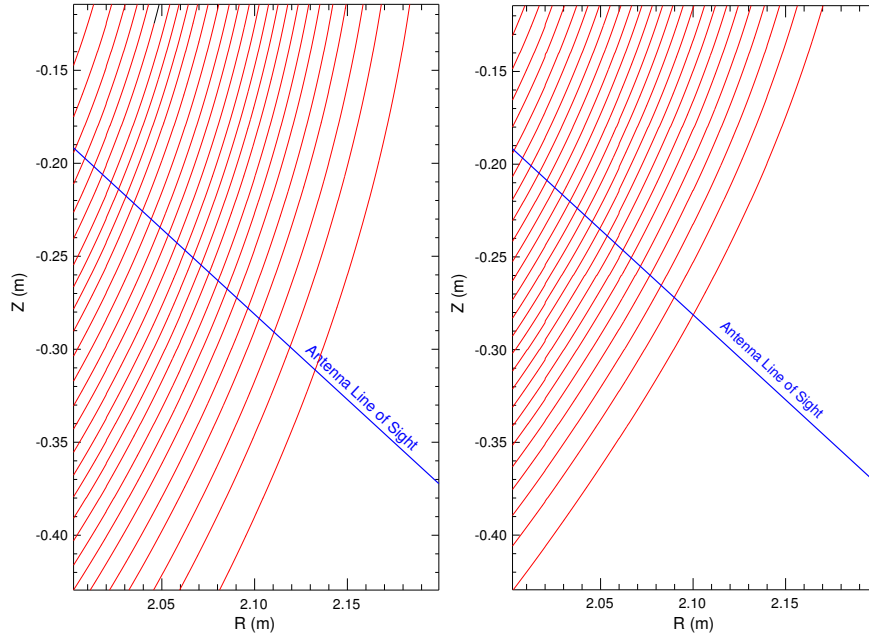
Since the overall goal is to replicate the experimental results in discharges # 19146 and # 19148, the experimental conditions in those discharges are closely matched in the code. The code uses the experimental density, magnetic field, antenna characteristics and a realistic model for the turbulent density fluctuations. This section describes the various input parameters of the code and how they are obtained.

As a first step, a computational grid size needs to be carefully selected. The number of grid points should be large enough to include the entire cutoff interaction and yet be as small as possible to reduce computational time. In the experiment, microwave frequencies were launched between 61.0 and 65.0 GHz, corresponding to wavelengths  $\lambda$  in the range between 0.49 cm and 0.46 cm. The normalized period  $\tau_{norm}$  chosen for the runs is 25. After a few initial runs of the code, an optimal grid size of 1601 points in the  $z$  direction and 1001 points in the  $r$  direction was chosen. The distance per grid point is then  $d = \lambda/\tau_{norm} \approx 0.02cm$ . Hence, the computational grid corresponds to roughly 20 cm in  $r$  and 32 cm in  $z$ . Again, some optimization was needed to determine the actual  $r$  and  $z$  coordinates which would include the cutoff position for both the low and high triangularity cases of discharges # 19146 and # 19148. The final grid coordinates chosen were:  $r$  between 2.00 to 2.20 m and  $z$  between -0.11 to -0.43 m, as shown in figure 8.4.

### 8.2.2.1 Experimental Electron Density and Magnetic Field

The electron density  $n_e$  profile is obtained from DCN interferometry, core Thomson scattering and standard reflectometry diagnostics for each of the eight experimental data points listed in table 8.1. Figure 8.4 shows density contours for the two extreme triangular cases (i.e. # 19146, 3.12s and # 19148 3.37s) plotted in the chosen  $r, z$  grid. The figure also illustrates the X-mode antenna line of sight into the plasma.

Likewise, the magnetic field components  $B_\theta$ ,  $B_\phi$  and  $B_r$  are obtained from the function parametrization reconstruction code.



(a) Electron density contours of discharge # 19146 at time=3.12s

(b) Electron density contours of discharge # 19148 at time=3.37s

Figure 8.4: Electron density contours measured in discharges # 19146 and # 19148. The contours are plotted in the chosen  $r, z$  grid for the computations.

### 8.2.2.2 Antenna Characteristics

The antenna in the 2D code resembles the X-mode antenna on ASDEX Upgrade. It is modeled as a monostatic system which launches a Gaussian beam distribution with the same beam width as the actual width in experiment ( $\approx 3\text{cm}$ ). It injects the microwave beam upwards at an angle of  $45^\circ$ , which accurately describes the launch angle of the X-mode antenna. (See section 4.2.1).

The one point in which the modeled antenna deviates from experiment is in its position. The antenna in the 2D code is positioned as close as possible to the plasma to minimize computational time. Outside the plasma, in vacuum, there is no electric and magnetic field and hence a more simpler and faster code may be utilized for calculating the remaining microwave propagation from the antenna position in the 2D code to the *actual* antenna position. Since we are only interested in the correlation of the fluctuations between two close cutoff layers, it is adequate to skip the last stage and correlate the signals at the plasma boundary.

To avoid reflection from the boundaries of the rectangular grid, a numerical absorber with a depth of 120 grid points is placed on all sides. The antenna is then positioned at the right hand side of the grid in front of an absorber. Hence, the antenna's position is  $r = 1001 - 120 = 881$  grid points,  $z = 399$  grid points.

### 8.2.2.3 Modeling Turbulent Density Fluctuations

The reflection layer in the plasma may be modeled as thin 'iso-refractive index' surface with two-dimensional distortions [37]. Each layer has perturbations with a wavenumber  $k$ -spectrum in both the radial and poloidal directions. The reflection layer displacement in  $r$  may be modeled by a Fourier summation given by

$$\zeta(z, r, t) = \frac{\sigma}{\zeta_{rms}} \sum^N h(k_p, k_r) \cos(\omega t + k_p z + \theta_p) \cos(k_r r + \theta_r) \quad (8.5)$$

where  $N = 231$ ,  $\sigma$  is the amplitude factor,  $\zeta_{rms}$  is the root mean square displacement,  $h(k_p, k_r)$  is the normalized  $k$ -spectral profile and  $\theta_p$  and  $\theta_r$  are random phases with a uniform distribution between  $\pm\pi$ . The  $k$ -spectral profile is modeled as a top hat function

$$h(k_p, k_r) = \begin{cases} 1 & \text{if } 0 \leq k_p \leq k_{pmax}, 0 \leq k_r \leq k_{rmax} \\ 0 & \text{otherwise} \end{cases} \quad (8.6)$$

Although equation 8.5 is a single slice through the  $k_r$  and  $k_p$  spectrum, it was found to give random layers with realistic poloidal and radial correlation functions and is computationally fast [37]. A simple relationship was found between the  $1/e$  poloidal and radial correlation lengths ( $L_p, L_r$ ) and the spectral widths.

$$L_p = 2.1/k_{pmax} \quad (8.7)$$

$$L_r = 2.1/k_{rmax} \quad (8.8)$$

The density fluctuations,  $\delta n_e$ , are finally calculated by taking a percentage of  $\zeta n_e$ . The percentage is variable, although anywhere between 10 – 25% is realistic at the plasma edge. The density distribution modified by the plasma turbulence, via the  $\delta n_e$  term, is then given by

$$n_e(x, y, t) = \langle n_e(x, y) \rangle_t + \delta n_e(x, y, t) \quad (8.9)$$

where  $\langle n_e(x, y) \rangle$  is the average experimental density profile. Since the density fluctuations are aligned with the magnetic field lines and move in the poloidal direction, a poloidal velocity of the fluctuations should also be accounted for in the code. This is most easily performed by first creating a larger grid of the displacement fluctuations (i.e. 10806 by 12552 grid points) and then rotating the fluctuations to match the tilt in the density contours. (The density contours are assumed to be straight tilted lines in the computational grid.) The movement of the turbulence may be modeled as the original computational grid size (i.e. 1001 by 1601 grid points) is stepped up in this large sized grid.

Using standard correlation techniques [104], it is possible to test the radial and poloidal correlation of the displacement fluctuations. The results for fluctuations with  $k_{pmax} = 10cm^{-1}$  and  $k_{rmax} = 15cm^{-1}$  are illustrated in figure 8.5. Both the poloidal and radial correlation lengths obtained satisfy the relationships given by equations 8.7, 8.8. The poloidal correlation length is  $L_p = 0.248cm \approx (2.1/10)cm$  while the radial correlation length is  $L_r = 0.146cm \approx$

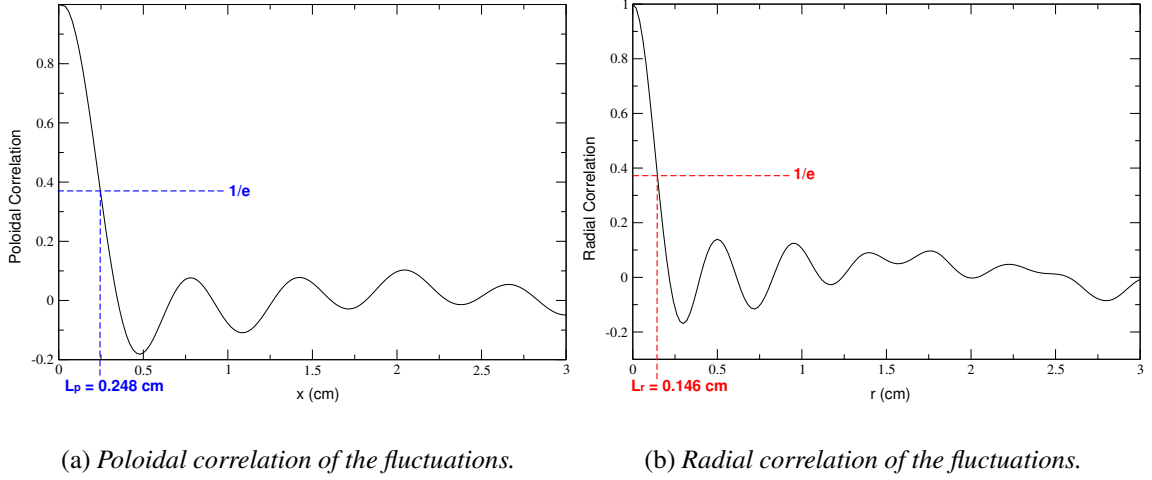


Figure 8.5: The poloidal and radial correlations of the modeled fluctuations with  $k_r = 15\text{cm}^{-1}$  and  $k_p = 10\text{cm}^{-1}$ .

( $2.1/15$ )cm. The  $k_{rmax}$  is chosen such that the resulting  $L_r$  is of the same order of magnitude as the  $L_r$  from experiment.

Another consideration to account for in the modeling of plasma turbulent fluctuations is the speed in which the turbulence moves. (Note the linear dispersion relation  $\omega/k_p = v_\theta$  where  $v_\theta$  is the propagating poloidal velocity.) If one assumes that the phase velocity of the turbulence is approximately 4km/s in the poloidal direction, it is obvious that in the computational grid of roughly 20 by 30cm, the turbulence moves so rapidly that the propagating microwave should encounter a statistically new turbulent fluctuation pattern with each launch of the beam. However, it is not possible to step the grid 1601 points in  $z$  each time, offering a new turbulence pattern each time. This would require an enormous fluctuation grid and is most likely not necessary. In the initial testing phase of the code, it was found that turbulence movements of +30 gave acceptable I and Q output signals. Steps of +1 were statistically oversampled (the I and Q signals were perfect sine waves) while steps greater than +100 appeared undersampled.

### 8.2.3 Obtaining $L_r$ from the 2D Full Wave Code

For recreating the experimental results shown in figure 8.3, the 2D full-wave code must provide radial correlation lengths. There are however major differences in the methods the experiment and simulation use to determine  $L_r$ . In the experiment, a large amount of data is collected in a short time (20MHz sampling rate) and the coherence of the signals may be obtained. From the 1/e coherence, the  $L_r$  is extracted. In the simulation, however, the computational time is so great that the bare minimum data is computed. This makes a calculation of the coherence which needs a large number of data points for an ensemble average impossible. Instead, the  $L_r$  in the simulation is obtained by the 1/e radial correlation of the signals. (In section 5.4.2,

correlation and coherence are defined.) The correlation requires far less data points, although the statistical error goes as  $1/\sqrt{N}$  where  $N$  is the number of data points. Nevertheless, the coherence and correlation contain the same information and so one will obtain the same  $L_r$  using these two signal processing methods just with different accuracies.

Discharge	Time (s)	$\theta_{tilt}$ (degrees)	$k_{\perp}$ ( $\text{cm}^{-1}$ )	$L_r$ (cm)
19146	2.35-2.40	17	7.46	0.33
	2.60-2.65	19	8.31	0.36
	2.85-2.90	20	8.73	0.385
	3.10-3.15	21	9.15	0.45
19148	2.35-2.40	17	7.46	0.33
	2.60-2.65	16.5	7.25	0.295
	2.85-2.90	15.5	6.82	0.19
	3.35-3.40	14	6.18	0.17

Table 8.1: The experimental results of discharges # 19146 and # 19148 which will be simulated by the 2D FDTD code.

The experimental results to be simulated by the 2D code are summarized in table 8.1. In the correlation experiment, one frequency channel was held constant at 61.0 GHz while the other frequency channel was stepped away to a maximum of 65.0 GHz. By 63.0 GHz, the complex coherence of the signals ( $I_1 + iQ_1$  and  $I_2 + iQ_2$ ) already dropped to its  $1/e$  value. In the simulation, eight frequencies were selected between 61.0 and 65.0 GHz (61.0, 61.1, 61.3, 61.5, 61.7, 62.1, 63.0 and 65.0 GHz). The code is run for each of these microwave launch frequencies until 128 I and 128 Q output values are collected. 128 was chosen to save computational time and yet offer an acceptable statistical error of  $1/\sqrt{128} = 0.09\%$ . The I and Q signals are then cross-correlated ( $I_1$  with  $I_2$  and  $Q_1$  with  $Q_2$ ) for varying frequency differences,  $\Delta f$ . Again here a difference between the methods experiment and simulation use for determining  $L_r$  is introduced. The correlation is performed on the homodyne I and Q signals as opposed to the complex signals. Rhodes has shown that plasma turbulence is adequately represented by homodyne signals [103]. Hence, for the purpose of this simulation, the homodyne I and Q signals are used. The eight frequencies selected for the simulation offer twenty possible combinations of  $\Delta f$ . To recreate figure 8.3, this method is then repeated for all eight experimental data points.

## 8.2.4 Testing of the 2D Code

Before the 2D full wave code could be used for determining radial correlation lengths of the turbulence, several tests were performed to check what the optimum settings should be and also that the code gives a reasonable output.

## 8.2.4.1 Radial Electric Field Patterns and Density Fluctuation Levels

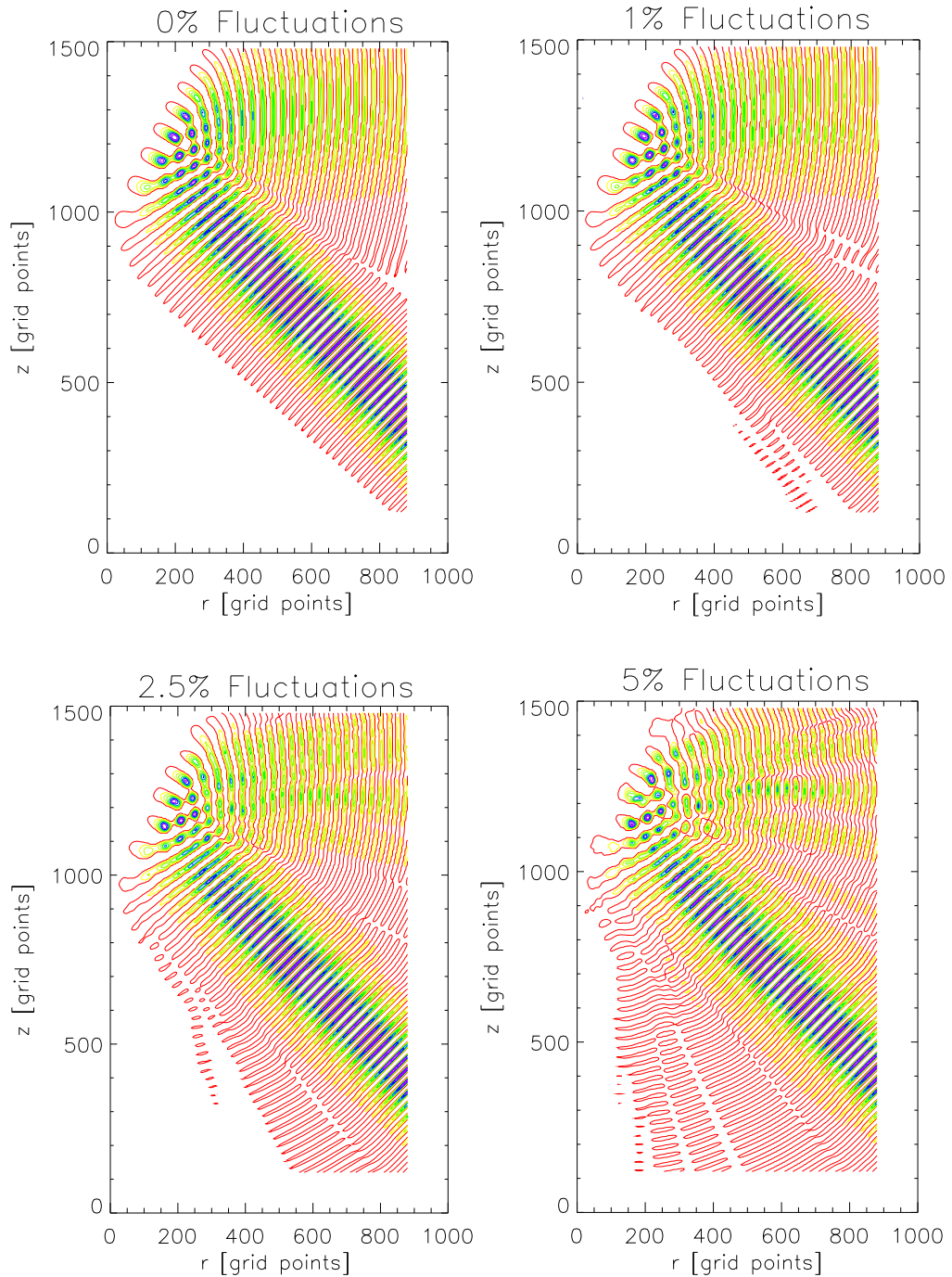


Figure 8.6: *Electric field patterns simulated for discharge # 19146 at 3.37s with various density fluctuation levels. The microwave is launched in X-mode with 61.0 GHz frequency.*

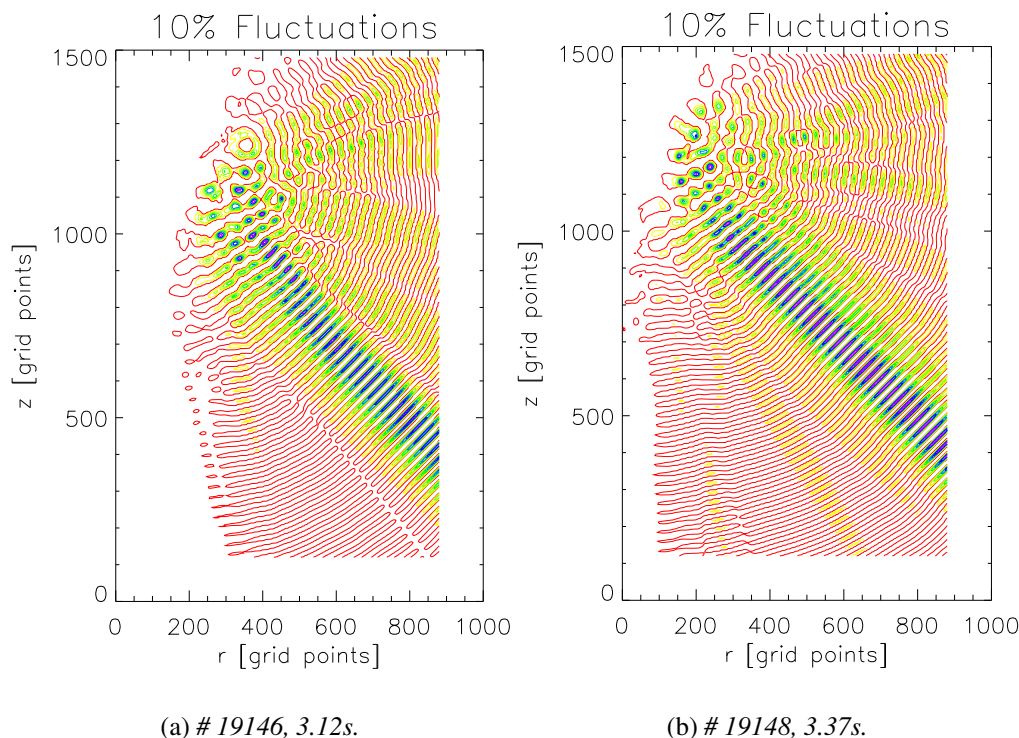


Figure 8.7: *Electric field patterns simulated for discharge # 19146 (3.12s) and discharge # 19148 (3.37s) with 10 % fluctuation level. The microwave beam is launched in X-mode with 61.0 GHz frequency.*

The first test performed was to run the code for discharge # 19148 (3.37s) and examine the resultant electric field patterns. A microwave beam of 61.0GHz is launched into the plasma with a fixed fluctuation pattern (i.e. not moving) but varying fluctuation level from 0% to 5%. The resulting electric field patterns are presented in figure 8.6. A counter in the code controls how long the code runs. It was found that approximately 2000 iterations or time steps ( $\Delta t$ ) are needed for the microwave beam to propagate into the plasma, interact at the cutoff layer with the density fluctuations and for the information of the interaction to return to the monostatic antenna. The electric field plots were obtained after 4000 time steps. The first example with a 0 % fluctuation level relates to the case of a plasma with no turbulence. As soon as the turbulence is increased via the density fluctuation level, side lobes appear in the electric field patterns. The interaction between the microwave beam and the turbulence at the cutoff layer becomes more complicated at the higher fluctuation levels. Since theory predicts density fluctuation levels of at least 10% at the plasma edge (see section 3.3), this level will be used for the 2D full wave simulation. The radial electric field patterns at 10% fluctuation level for the two extreme triangular cases of the discharges # 19146 and # 19148 are presented in figure 8.7.

Previously in figure 8.5, the radial and poloidal correlation lengths of the displacement fluc-

tuations  $\zeta$  agreed with the relationships in equations 8.7, 8.8. As a further check, the radial correlation of the density fluctuations  $\delta n_e$  may also be determined. Using the example discharge # 19148, 3.37s with a 5% fluctuation level, the parameters: displacement ( $\zeta$ ), density fluctuations ( $\delta n_e$ ), experimental density ( $n_e$ ) and the density distribution ( $n_e + \delta n_e$ ) along the  $r$  direction with constant  $z = 1480$  grid points may be extracted from the lower right-hand plot of figure 8.6. These parameters are plotted as a function of  $r$  in figure 8.8. Note how the fluctuations add to the *average* experimental density profile such that the resulting density distribution has the same mean as the experimental density profile. This is important since a higher density distribution would push the cutoff position further out of the plasma with reference to the undisturbed  $n_e$  profile.

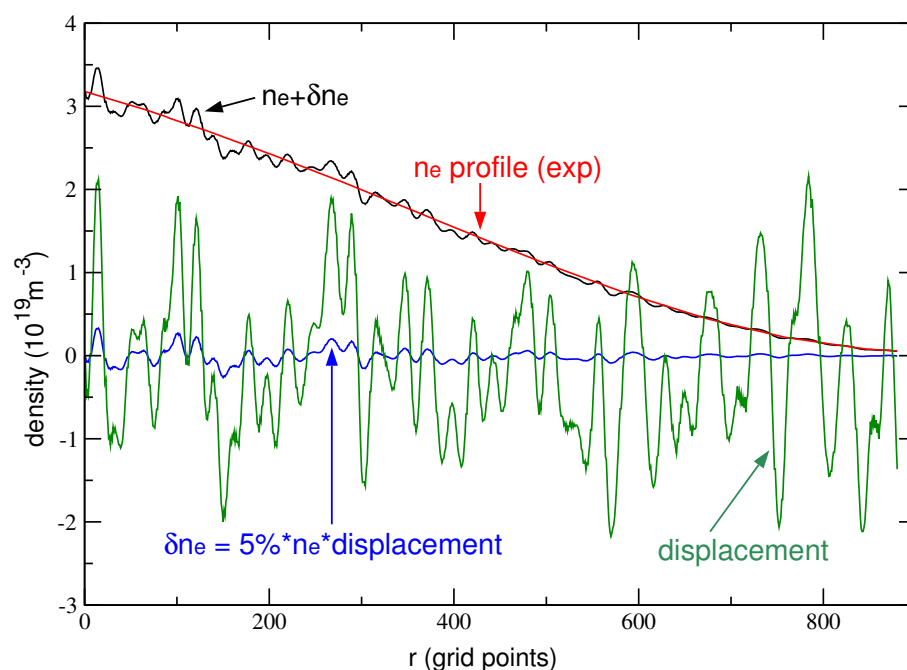


Figure 8.8: The displacement, density fluctuations, experimental density profile and density distribution ( $n_e + \delta n$ ) along  $r$  with constant  $z=1480$  grid points. The parameters are obtained from discharge # 19148 at 3.37s with a 5 % fluctuation level.

A comparison of the radial correlation of the density fluctuations and of the displacement fluctuations, which were already seen in figure 8.5, is given in figure 8.9. The density fluctuations give a slightly larger  $L_r$  most likely due to the fact that these fluctuations are rotated to align with the magnetic field, in this case  $29^\circ$ . While this is the maximum rotation performed (the other seven data points have tilted density contours at smaller angles), the maximum difference in  $L_r$  is 0.03 cm. This is such a small difference compared with the measurement error that it can be considered negligible.

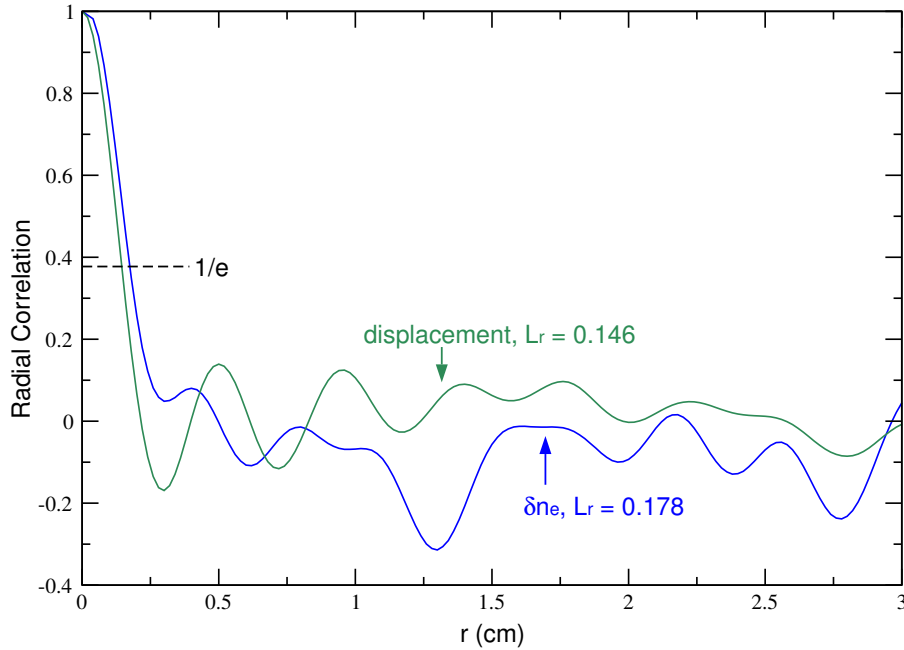


Figure 8.9: The radial correlation of the simulated displacement fluctuations as well as the density fluctuations. Both give radial correlation lengths as expected.

#### 8.2.4.2 The I and Q Output Signals

Further testing of the 2D code includes examining the I and Q output signals and their behaviour as a function of the number of time steps. Using the same example discharge # 19148 at 3.37s, the I output signals for three different fluctuation levels were collected for 100,000 iterations. At first, a 0% density fluctuation level is applied in all three cases. The fluctuation pattern is held fixed for the 10,000 time steps, at which time the fluctuation level increases to 1, 5 or 10% and remains set at that level. At every following 10,000 time steps (starting with 20,000 time steps), the fluctuations are moved +500 grid points and then are held stationary. The behaviour of the I output signals is presented in figure 8.10. With no turbulence in the plasma (i.e. a 0% fluctuation level), the Doppler reflectometer signals I and Q are very small. This clearly shows how difficult it is to use the diagnostic for measurements in low turbulent plasma regimes. At the moment in which the turbulent fluctuations are moved, the I output signal does not register this movement. After a short time ( $\approx 2000$  iterations) a large spike or peak is detected in the I output signal. This is the time the microwave has travelled to the new fluctuation pattern and returns back to the receiving antenna. Depending on the level of fluctuations, it takes some time for the I signal to stabilize at a mean value. The I signal from the 10 % fluctuation level appears, even after 10,000 time steps, to still fluctuate about the mean value. This indicates the strong multiple reflections occurring there, which can be observed in the radial electric field patterns of figure 8.7.

The Q output signals behave similarly as the I signals except they are in quadrature. Figure 8.11 shows the output signals obtained using the 2D full wave code and simulating the experimental

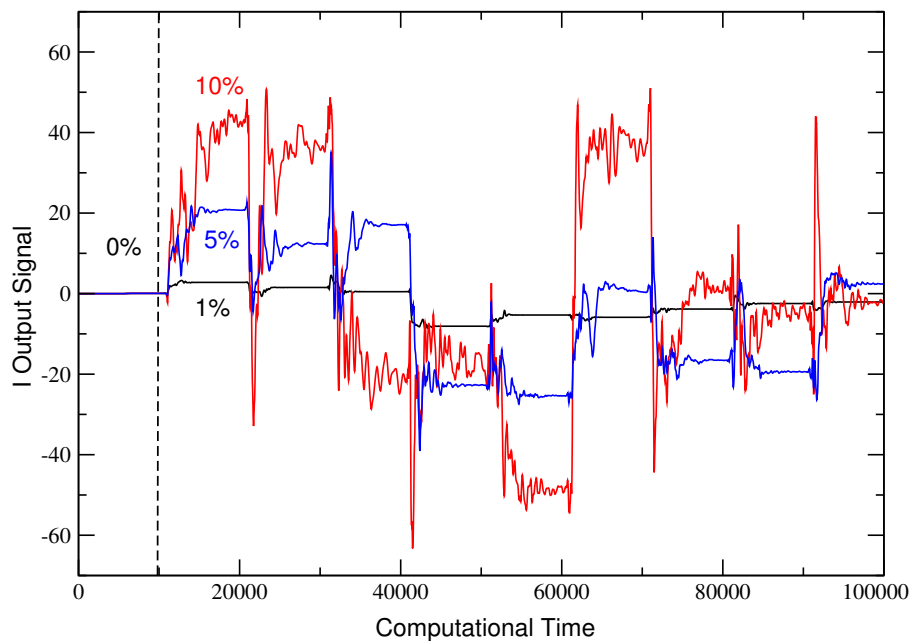


Figure 8.10: The  $I$  output signal variations with 0, 1, 5 and 10 % fluctuation levels for the example # 19148, 3.37s.

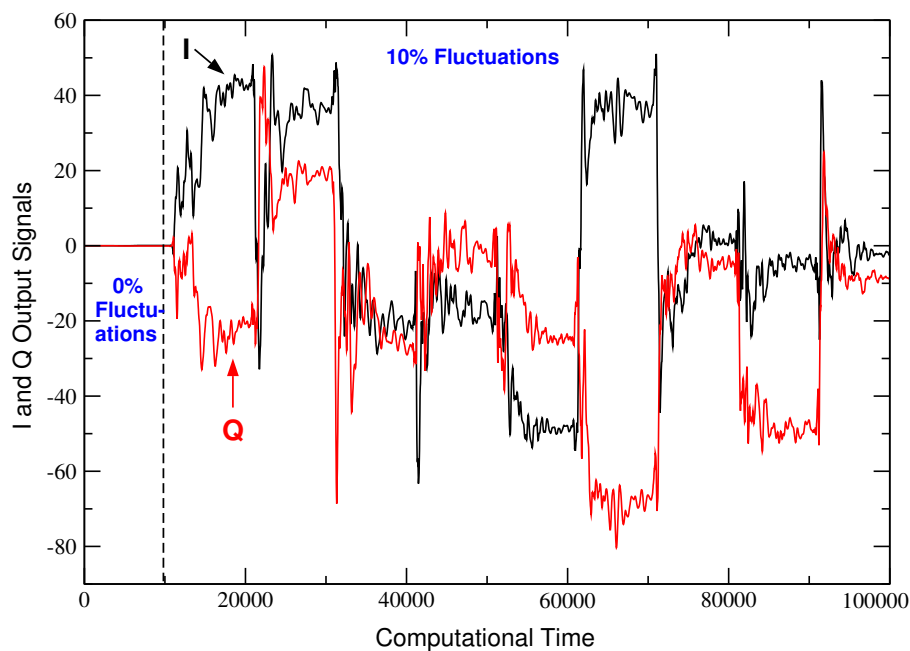


Figure 8.11: The behaviour of the  $I$  and  $Q$  output signals as a function of time for example # 19148, 3.37s, 10 % fluctuation level. The  $I$  and  $Q$  signals are  $90^\circ$  out of phase.

conditions of discharge # 19148 (3.37s). Again in the first 10,000 iterations the fluctuation level is 0%. Afterwards, the level increases to its fixed value of 10%. With every 10,000 time

steps, the turbulence is moved +500 grid points. The I and Q signals are  $90^\circ$  out of phase and their behaviour shown in the figure is as expected.

It was decided after these tests to move the turbulence every 4000 iterations. At the end of 4000 iterations, the I and Q output signals are then collected. This amount of time allows the signals to become relatively stable (recall a minimum of 2000 iterations are needed for the microwave to travel to the cutoff and back again) while not being too long of a waiting time in order to obtain a result in a reasonable amount of time. 4000 iterations takes approximately one hour of computation.

### 8.2.5 Results

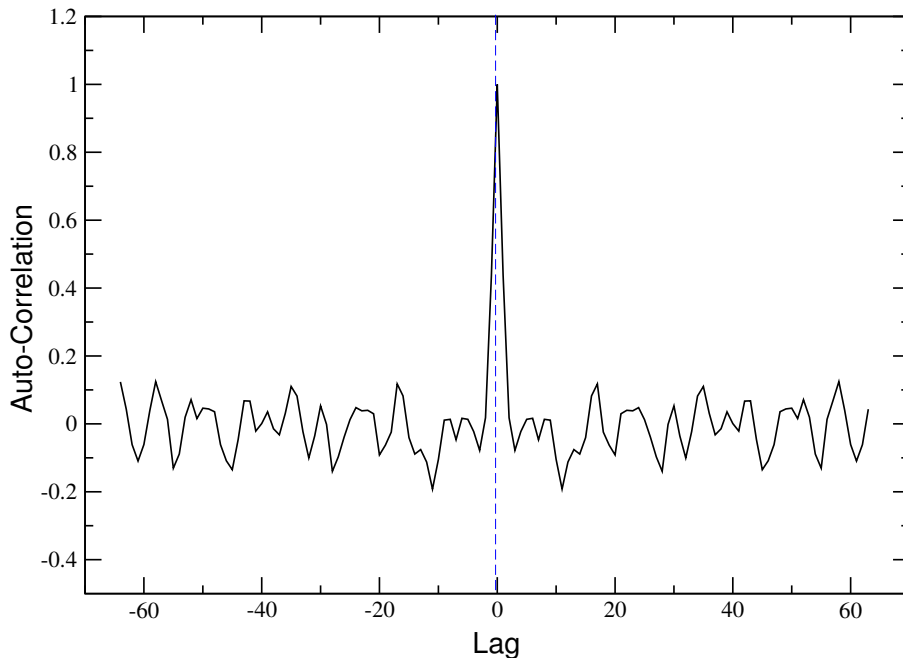


Figure 8.12: *The auto-correlation as a function of lag obtained by cross-correlating the I signal from discharge # 19418 (3.37s, 61 GHz) with itself. A solid peak occurs at zero lag.*

The previous sections of this chapter have described the main settings chosen for the simulation. The modeled turbulence moves +30 grid point steps and after each movement, a waiting time of 4000 time steps is made before sampling the I and Q output signals. For each of the eight experimental data points listed in table 8.1, 128 data points in I and Q each are simulated for eight frequencies between 61.0 and 65.0 GHz. The modeled turbulence may be altered by varying three parameters: level of density fluctuations and the spectral widths  $k_{pmax}$  and  $k_{rmax}$ . The first simulation case performed was with a turbulence defined by 10% fluctuations,  $k_{pmax} = 10cm^{-1}$ , and  $k_{rmax} = 15cm^{-1}$ . Taking the auto-correlation of the I output signal simulated for a microwave launch frequency of 61.0GHz in discharge # 19148 at 3.37s, one obtains

the plot shown in figure 8.12. The result is common for an auto-correlation, which typically gives a well defined peak at zero lag with a correlation of unity.

By cross-correlating the resulting I output signals from the other frequency sets, one obtains plots of the cross-correlation varying with frequency separation, as shown in figure 8.13. It is evident that the correlation changes sign frequently. This is expected because the homodyne I and Q signals have a cosine/sine dependence (see equations 4.30 and 4.31), which results in an oscillation in the correlation. This has been observed both experimentally and in simulation work in other devices [73]. Generally, the maximum absolute correlation occurs at or very close to zero lag. At large time lags, the cross correlation coefficient should go to zero. However, due to the finite sample length of 128 points, it oscillates randomly around  $0 \pm 0.1$ . This agrees with the predicted error in the correlation when using 128 points (i.e. error  $\approx 1/\sqrt{128} \approx 0.09$ ). For determining  $L_r$ , one could plot the maximum correlation (whether

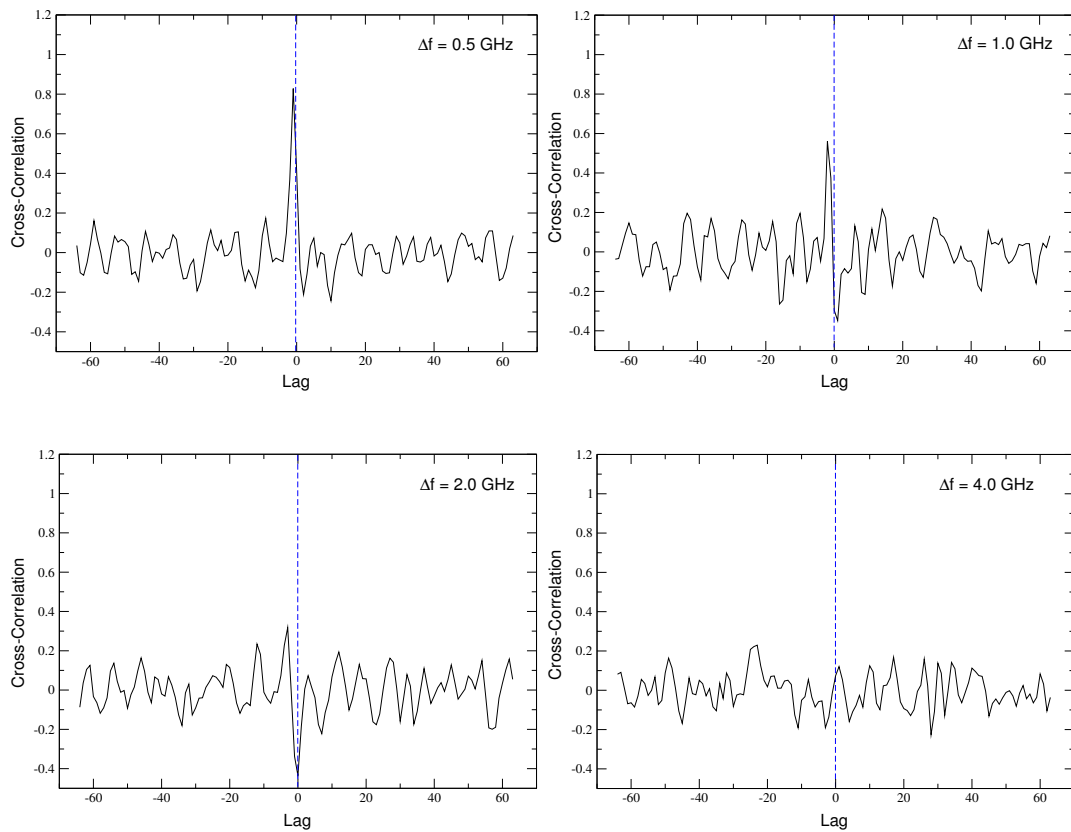


Figure 8.13: Cross-correlations of the I output signals of discharge # 19148 (3.37s). The various I signals were obtained from the 2D FDTD runs, each with different launched frequency microwave beams.

positive or negative) of the signals as a function of frequency separation or the correlation at zero lag as a function of frequency separation. An example is shown in figure 8.14 for dis-

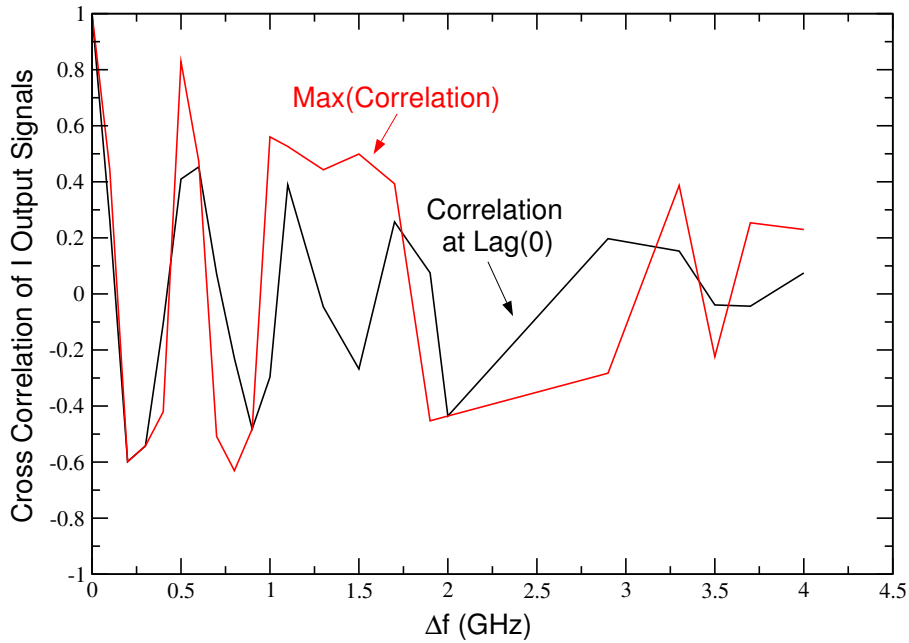


Figure 8.14: Two methods for obtaining the correlation as a function of frequency difference,  $\Delta f$ . The first is to take the maximum correlation and the second is to take the correlation at zero lag. The second method is utilized in this thesis.

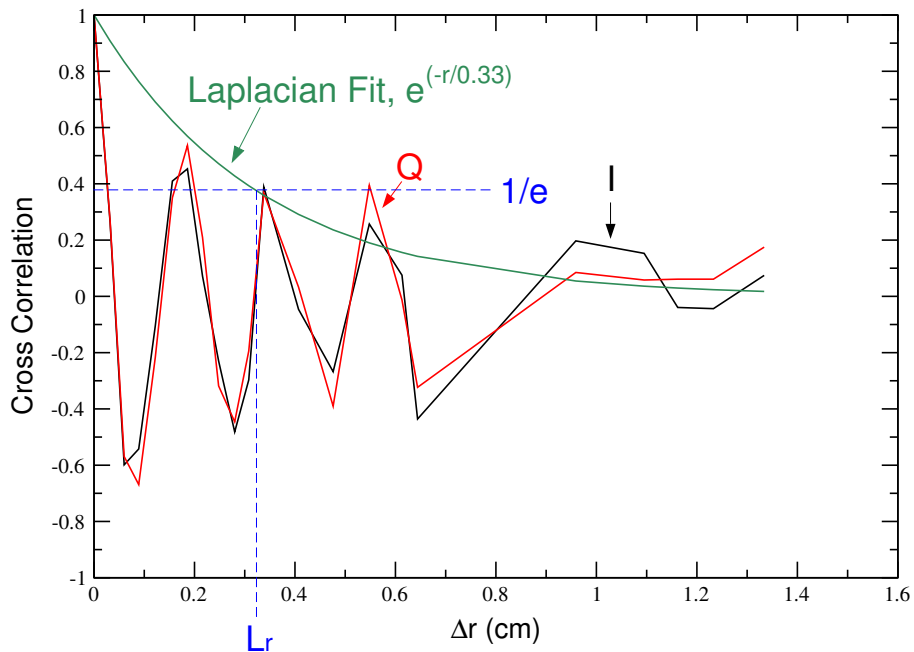


Figure 8.15: Cross-correlation of the output  $I$  and  $Q$  signals of discharge # 19148 (3.37s). The Laplacian fit is shown by the green curve, from which  $L_r = 0.33\text{cm}$ .

charge # 19148 (3.37s). The reason why the correlation peak can move away from  $\tau = 0$  is due to radial propagation delay between the two cutoff layers (i.e. one microwave travels further into the plasma than the other). But, the cutoff layer separation is small compared to  $c/f$  and hence, for this thesis work, the correlation at zero lag was used for determining  $L_r$ .

By translating the frequency separation  $\Delta f$  to a radial separation  $\Delta r$  with the use of the X-mode cutoff equations 4.26, 4.25, the cross-correlations may be plotted as a function of  $\Delta r$ . Figure 8.15 shows the I and Q cross-correlations as a function of radial separation for discharge # 19148 (3.37s). As expected for homodyne reflectometer signals, a maxima-minima structure in the correlation versus radial separation between the reflecting layers is observed. It has been found that an envelope may be fitted to the maxima to give the correct decay [73]. In this example, a Laplacian is fitted to the correlation, giving an  $L_r = 0.33\text{cm}$ . This procedure is repeated for the other time points in discharges # 19148 and #19146 and the results are plotted along with the experimental  $L_r$  in figure 8.16.

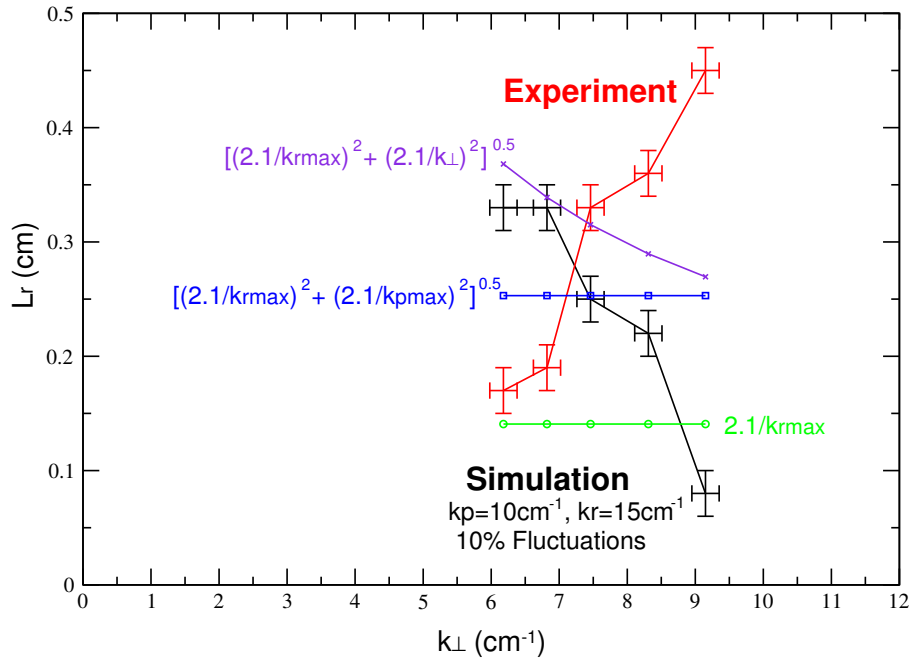


Figure 8.16: The radial correlation lengths as a function of  $k_{\perp}$  measured in the experiment and simulated by the 2D FDTD code. The experiment and simulation show opposite trends.

The simulation results, although having the same magnitude in  $L_r$ , show the opposite trend:  $L_r$  decreases with increasing  $k_{\perp}$ . This is the trend simple theory predicts, as described in section 8.1.3. It is also interesting to note that the predicted  $L_r$  (defined by  $L_r \approx 2.1/k_{rmax} = 0.14\text{cm}$ ) agrees only with the simulation result at the higher  $k_{\perp}$  values. Fits using a combination of  $k_{rmax}$ ,  $k_{pmax}$  and  $k_{\perp}$  are also shown in figure 8.16. None of the proposed fits accurately describe the simulation results. There must be some other strong influential factor present or the dependence of  $L_r$  on the turbulent wavenumbers is not so obvious.

The modeled turbulence allows the simulation to be repeated for various turbulence parameters

(via the change in fluctuation level,  $k_{pmax}$  and  $k_{rmax}$ ). As a next step, the fluctuation level was decreased to 5% but no obvious change appeared in  $L_r$ . A systematic scan of the simulation was repeated with varying wavenumbers and a fixed 10% fluctuation level and the results are presented in figure 8.17. Here, only the two extreme triangularity cases (#1946, 3.12s and #19148, 3.37s) are simulated. The simulation shows that the variation in radial and poloidal wavenumbers can change not only the magnitude of  $L_r$  but also its gradient with respect to  $k_{\perp}$ . The left hand side of the figure shows a scan in  $k_{rmax}$ , where  $k_{pmax}$  is held constant at  $10cm^{-1}$ . With a decrease in  $k_{rmax}$  from 15 to  $2cm^{-1}$ , the  $L_r$  gradient changes from negative to almost constant and then positive. The case where  $k_{pmax} = 10cm^{-1}$  and  $k_{rmax} = 2cm^{-1}$  is the one case which gives a similar trend as in experiment where  $L_r$  increases with  $k_{\perp}$ . Hence, it is plausible that in the experiment, the turbulence has a very low  $k_r$  accounting for the surprising trend.

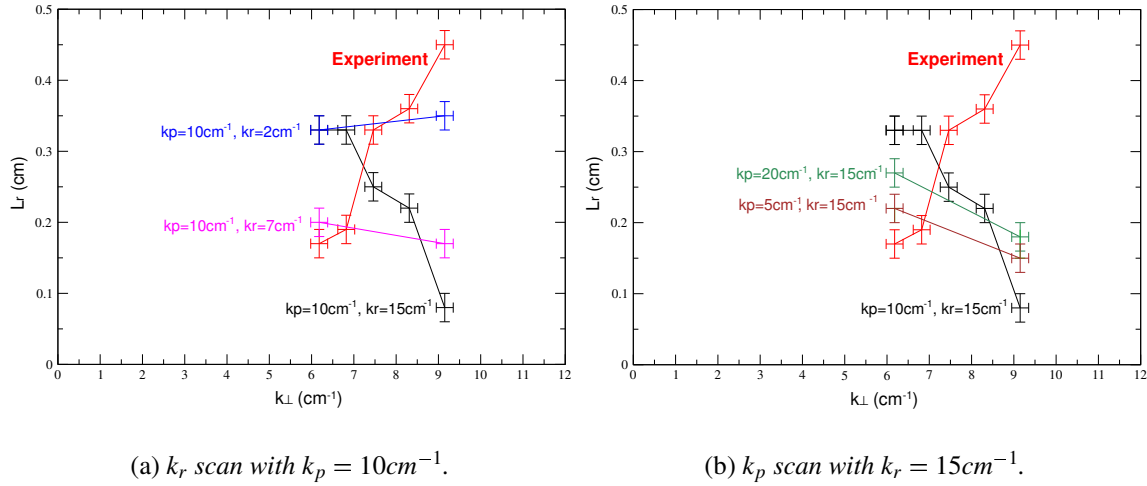


Figure 8.17: Comparison of  $L_r$  determined experimentally and the  $L_r$  from the simulations. The various changes in  $k_p$  and  $k_r$  affect the gradients in  $L_r$ .

Figure 8.17(b) shows the simulation results for a scan in  $k_{pmax}$  with constant  $k_{rmax} = 15cm^{-1}$ . The gradient in  $L_r$  shows no obvious trend in the figure. The  $L_r$  gradients when  $k_{pmax} = 20cm^{-1}$  and  $k_{pmax} = 5cm^{-1}$  are similar while the gradient steepens for the  $k_{pmax} = 10cm^{-1}$  scan. The gradients remain negative for all the three scans performed. The predicted  $L_r$  (defined by  $L_r \approx 2.1/k_{rmax} = 0.14cm$ ) agrees with the three scan in  $k_{pmax}$  only at the higher  $k_{\perp}$  values. This might imply that the Doppler reflectometer diagnostic measures the *true*  $L_r$  only for cases of high  $k_{\perp}$  greater than  $9cm^{-1}$ . This however would be in contradiction with some of the results in the  $k_{rmax}$  scan.

The observation that the  $L_r$  gradient changes with variation in  $k_{rmax}$  indicates that the radial wavenumber may have a greater effect on  $L_r$  than the poloidal wavenumber. This is an area for future research. The agreement between the experimental results and the  $k_{pmax} = 10cm^{-1}, k_{rmax} = 2cm^{-1}$  scan is far from perfect and much of the parameter space is still to be investigated.

## 8.3 Summary

For the first time, correlation Doppler reflectometry was employed for determining the radial correlation lengths of the turbulence. The experimental measurements give results which agree with theory as well as with experimental measurements from other diagnostics on other tokamak machines.  $L_r$  decreases by a factor of two at the L-H transition at the plasma edge. The absolute  $E_r$  shear was also observed to increase in this plasma region (see chapter 7). Hence, the experimental results support the Biglari, Diamond and Terry (BDT) model [8], which predicts that an increase in absolute shear suppresses density fluctuations and stabilizes the turbulence, thereby decreasing  $L_r$ . At the plasma edge, density fluctuations and  $E_r$  shear are higher than in the core. The  $L_r$  measurements agree with this observation by increasing monotonically into the plasma core. The main experimental result, which has motivated 2D FDTD simulations, is the relationship of  $L_r$  with  $k_\perp$ . The experiment shows  $L_r$  increasing with  $k_\perp$ , in contradiction with the simple theory described in section 8.1.3. The simulation, performed to understand this result, requires the experimental density and magnetic fields. The turbulence in the simulation is modeled such that its poloidal and radial wavenumbers and fluctuation levels may be altered. The simulation work has shown that although most cases of specified turbulence show  $L_r$  decreasing with  $k_\perp$ , one case in particular with very low  $k_r$  agrees with the experimental trend. In addition, it appears as though the Doppler reflectometer diagnostic measures the *true*  $L_r$  of the turbulence only at high  $k_\perp$  magnitudes (i.e. greater than  $9\text{cm}^{-1}$ ). The simulation has also shown the dependence of the Doppler reflectometer on the turbulence level. The Doppler reflectometer signals require a certain level of turbulence otherwise they are too small to give any Doppler shifts. This explains nicely why at an ELM event, the Doppler shifted frequency vanishes briefly for a moment and only recovers shortly thereafter when the turbulence level is restored.

In conclusion, the surprising increase of  $L_r$  with  $k_\perp$  may be explained by three possibilities: either the turbulence in discharges #19146 and #19148 has structures with very short radial dimensions, stretched in the poloidal direction and/or the  $L_r$  measurements from the Doppler reflectometer diagnostic are only valid for very high  $k_\perp$ . A third possibility is that by changing the triangularity of the plasma (as in the case of discharges #19146 and #19148), the turbulence is also changed accounting for the puzzling experimental results. As shown in figure 7.8, the radial electric field shear becomes weaker as a function of  $k_\perp$  in the experimental discharges. The weaker shear may be responsible for the increase in  $L_r$ , since shear is believed to deform and tear turbulent structures, thereby affecting  $L_r$ . A repeat of this experiment with constant plasma conditions and a remote steerable antennae system could provide an answer to whether the change in plasma triangularity affects the relationship between  $L_r$  and  $k_\perp$ .



# Chapter 9

## Conclusions and Outlook

Anomalous transport remains the most significant obstacle to performance improvement in tokamaks. Plasma micro-turbulence is believed to be the main cause of the enhanced radial transport over the level predicted from collisional calculations. Hence, this makes measurements of turbulence properties important in order to understand and thereby control the turbulence. A full understanding of turbulence requires knowledge, or measurement, not just of its amplitude but also its dispersion relation, that is, frequency and wavenumber distribution or spectra and phase and group velocity. Obtaining measurements of all parameters simultaneously in all plasma quantities (i.e.  $\tilde{n}$ ,  $\tilde{T}_e$ ,  $\tilde{\Phi}$  and  $\tilde{B}$ ) is particularly challenging. The majority of measurements to date are of  $\tilde{n}$  fluctuation profiles and spectra or of correlation lengths.  $\tilde{n}$  is the easiest parameter to measure but also the most important since it is orders of magnitude larger than in other types of fluctuations. Diagnostic tools are constantly being developed to advance our present day understanding of plasma turbulence.

Doppler reflectometry is a new radar technique used since 1999 for diagnosing magnetically confined plasmas [9, 10, 11]. It uses the back-scatter of microwaves from a radial position where the plasma refractive index equals zero to measure the perpendicular velocity of the turbulent fluctuations,  $u_{\perp}$ .  $u_{\perp}$  is directly related to the plasma  $E \times B$  velocity,  $v_{E \times B}$ , from which the radial electric field  $E_r$  in the plasma can be obtained. In this thesis work, the technique is extended with the introduction of a second Doppler reflectometer channel to allow correlation measurements. This new technique, radial correlation Doppler reflectometry, is capable of simultaneous measurements of the radial electric field shear  $\partial E_r / \partial r$  and the radial correlation lengths of the turbulence  $L_r$ . Both  $E_r$  and  $\partial E_r / \partial r$  are believed to be fundamental in quenching plasma turbulence. Since  $L_r$  gives the spatial dimension of a turbulent eddy, these parameters should be linked.

This thesis work presents a survey of experimental  $u_{\perp}$  (chapter 6),  $E_r$ ,  $\partial E_r / \partial r$  (chapter 7) and  $L_r$  measurements (chapter 8) made by Doppler reflectometry in a variety of plasma scenarios. The results show good agreement in comparison with theoretical models and experimental measurements from other diagnostics, hence validating the use of Doppler reflectometry as a plasma diagnostic.

The  $u_{\perp}$  measurements show a dependence on both the plasma radial electric field  $E_r$  and

magnetic field  $B$ , confirming the relationship  $u_{\perp} \approx v_{E \times B}$ . The dependence of  $u_{\perp}$  on  $B$  was clearly observed when the toroidal magnetic field was reversed in a closely matched discharge and the resulting  $u_{\perp}$  profiles were mirror images of each other. As a function of radius,  $u_{\perp}$  typically displays a negative peak at the plasma edge, around the density pedestal location. The  $u_{\perp}$  results show a strong correlation between the confinement of a discharge and this peak. The higher the confinement, the higher the absolute peak value of  $u_{\perp}$  at the plasma edge. Theory predicts that confinement is linked to high  $E_r$  and in particular high  $E_r$  shear. Hence, the trend of increasing confinement with edge  $u_{\perp}$  values is expected. This trend was seen in the results from low confined L-modes to high confined H-modes and QH-modes. These results give confidence that the Doppler reflectometer may be used for obtaining accurate  $E_r$  measurements. By examining the various components of  $u_{\perp}$  (given by the radial force balance equation), it was found that at the plasma edge, the diamagnetic velocity  $v^*$  dominates. The steeper gradients in the electron density and temperature profiles of an H-mode, compared to an L-mode, are the main reasons accounting for the larger  $v^*$  and hence  $u_{\perp}$  absolute magnitudes at the plasma edge.

As part of this thesis work,  $E_r$  measurements were made on the ASDEX Upgrade tokamak for a wide variety of plasma discharges. The  $E_r$  profile in a standard ASDEX Upgrade plasma configuration, with  $-B_{\phi}, +I_p$ , is positive in the SOL and then undergoes a reversal at the plasma edge, coinciding with the plasma pedestal region. This reversal forms what is known as an  $E_r$  well. The depth of the well is observed to increase dramatically with the confinement of the discharge while the width of the well appears unaffected. The large depth of the  $E_r$  well in H-modes can be explained by the large edge pressure gradient which exists there. Once the transition to H-mode is obtained, the  $E_r$  well depth is unaffected by the total auxiliary heating power applied in a discharge. This supports the prediction that it is the pressure gradient  $\nabla P$  which is responsible for the variation in the depth of the  $E_r$  well.  $\nabla P$  is limited by MHD stability criterion, that is, a certain edge current density can only support a certain plasma pressure otherwise it becomes kink unstable. Although not affected by the *total* heating power, the  $E_r$  profile is altered by the *type of* heating power applied. In comparing pure NBI and pure ICRH heated phases in a counter-current NBI injected discharge, the  $E_r$  profile flips sign in the plasma core. This is due to the direction of the toroidal velocity  $v_{\phi}$  which is in the counter-current direction in the NBI heated phase and in the co-current direction in the ICRH heated phase. The result indicates that ICRH power may also be a driving force for toroidal rotation. With an addition of ICRH heating power to NBI,  $v_{\phi}$  decreases in the plasma mid-core, leading to a decrease in  $E_r$ . The dependence on plasma shape was also investigated and was found to have a strong influence on the edge  $E_r$  profiles. Discharges with an upper single null (USN) have smaller absolute values of  $E_r$  compared to discharges with a lower single null (LSN). Simulation work exists which shows that the divertor configuration changes the parallel fluxes in the plasma SOL and edge, resulting in a modification in  $E_r$  [88].

There is debate in the literature concerning which parameter,  $E_r$  or its first derivative  $\partial E_r / \partial r$  (i.e. shear), is more important for plasma turbulence suppression. For the first time, correlation Doppler reflectometry was employed for determining  $E_r$  shear profiles. The results show that  $E_r$  shear is localized at the plasma edge, being small elsewhere. Measurements in L-modes, H-modes and quiescent H-modes show that the positive shear at the plasma edge (linked to the

separatrix/SOL region) is relatively constant but the amount of negative shear (associated with the pedestal region) changes, depending on the plasma confinement. In comparing the experimental measurements to the various theories involving  $E_r$  shear, it was found that the BDT model agrees best with the measurements. The BDT model claims that an increase in absolute shear, decreases turbulent fluctuations, stabilizes the turbulence and leads to a decrease in  $L_r$  [8].  $L_r$ , also measured from the same correlation Doppler reflectometer diagnostic, decreases by a factor of two at the L-H transition at the plasma edge in agreement with the BDT model. Further experimental  $L_r$  measurements show that radial lengths increase monotonically into the plasma core. This observation agrees with the BDT model since in the plasma core, density fluctuations and  $E_r$  shear are lower than at the edge. The correlation Doppler reflectometer also allows  $L_r$  to be measured as a function of the turbulence wavenumber  $k_\perp$ . The results show  $L_r$  unexpectedly increasing with  $k_\perp$ . This motivated an investigation of the diagnostic response using a 2D full wave simulation code. The simulation uses experimental density and magnetic fields with a realistic turbulence model with adjustable poloidal and radial wavenumbers as well as fluctuation levels. The simulation results show that for the majority of turbulence parameter scans,  $L_r$  decreases with  $k_\perp$ , except for very short  $k_r$  turbulence which shows  $L_r$  increasing with  $k_\perp$ . The simulation has also shown the dependence of the Doppler reflectometer on the turbulence level; the signals becoming stronger with increasing turbulent fluctuation level, indicating that there may be a threshold fluctuation level, below which the Doppler reflectometer fails to give a Doppler shift. There is still much future work to be done with the simulations to fully understand the instrument response function.

The measuring potential of the Doppler reflectometer diagnostic has only just been touched upon. New applications are still being discovered, such as measurements of  $E_r$  fluctuations and changes in the turbulence phase velocity. The fast temporal resolution of the Doppler reflectometer allows the possibility to measure the  $E_r$  and its shear during fast transitions in a discharge. By measuring the development of the absolute  $E_r$  shear at the edge L-H transition, one may obtain further insight into the reason for the improved confinement in H-modes. (Klinge has already begun to investigate this [61].) The casual development of  $E_r$  is also of great interest. Does the improvement in confinement occur due to the change in  $E_r$  or due to the change in the density and temperature profiles which then change  $E_r$ ? This information might be gained by operating the correlation Doppler reflectometer with a fixed microwave launch frequency separation and then monitoring  $\partial E_r / \partial r$  at the plasma pedestal as a function of time through the L-H transition.

The diagnostic is capable of providing further measurements of the turbulence properties, such as the density fluctuation level. This information is contained in the amplitude of the Doppler reflectometer signals. It would be interesting to obtain a simultaneous measurement of the  $E_r$  shear,  $L_r$  and density fluctuation level and to investigate the link between these properties. The BDT model predicts the existence of such a link.

Most of the measurements presented here were concentrated at the plasma edge. A future hardware upgrade includes the construction of a W-band Doppler reflectometer. The W-band covers the microwave frequency range 75-110 GHz, which will allow the diagnostic to penetrate deeper into the plasma core. A second hardware upgrade includes the construction of

remote steerable antennae. This will allow a scan of the turbulent wavenumber  $k_{\perp}$  while maintaining a fixed measurement configuration.

# Bibliography

- [1] H.A.Bethe, Phys. Rev. **55** (1939) 434
- [2] J.Wesson, *Tokamaks*, Clarendon Press, Oxford (1987)
- [3] A.Yoshizawa et al., *Plasma and Fluid Turbulence*, IOP Publishing Ltd, Bristol and Philadelphia (2003)
- [4] L.A.Artsimovich, Nucl. Fusion **12**, 215 (1972)
- [5] J.Hugill, Nucl. Fusion **23**, 331 (1983)
- [6] A.J.Wootton et al., Phys. Fluids B **2** 2879 (1990)
- [7] K.H.Burrell, Plasma Phys. Control. Fusion **36**, A291 (1994)
- [8] H.Biglari et al., Phys. Fluids **B2**, 1 (1990)
- [9] G.D.Conway et al., Plasma Phys. Control. Fusion **46**, 951 (2004)
- [10] M.Hirsch et al., Plasma Phys. Control. Fusion **43**, 1641 (2001)
- [11] M.Hirsch et al., Plasma Phys. Control. Fusion **46**, 593 (2004)
- [12] F.Wagner et al., Phys. Rev. Lett. **49**, 1408 (1982)
- [13] Special Issue on ASDEX Upgrade, Fusion Science and Technology **44**, 569 (2003)
- [14] A.Staebler et al., Proc. 18<sup>th</sup> Symp. Fusion Technology, Karlsruhe, 593 (1995)
- [15] O.Vollmer et al., Proc. 20<sup>th</sup> Symp. Fusion Technology, Marseille, 449 (1999)
- [16] J.M.Noterdaeme et al., Europhys. Conf. Abstr., 61 (1992)
- [17] R.Dux et al., Journal Nucl. Mater. **337**, 852 (2005)
- [18] ITER Physics Basis, Nucl. Fusion **39**, 2137 (1999)
- [19] M.E.Manso, Plasma Phys. Control. Fusion **35**, B141 (1993)
- [20] W.Suttrop et al., Plasma Phys. Control. Fusion **38**, 1407 (1996)

- [21] O.Gruber et al., Phys. Rev. Lett. **83**, 1787 (1999)
- [22] R.C.Wolf et al., Plasma Phys. Control. Fusion **41**, B93 (1999)
- [23] T.S.Taylor, Plasma Phys. Control. Fusion **39**, B47 (1997)
- [24] K.H.Burrell et al., Plasma Phys. Control. Fusion **44**, A253 (2002)
- [25] W.Suttrop et al., Plasma Phys. Control. Fusion **45**, 1399 (2003)
- [26] W.Suttrop et al., Plasma Phys. Control. Fusion **46**, A151 (2004)
- [27] A.Semet et al., Phys. Rev. Lett. **45**, 445 (1980)
- [28] S.F.Paul et al., Phys. Fluids **B4**, 2922 (1992)
- [29] D.L.Brower et al., Nucl. Fusion **27**, 2055 (1987)
- [30] R.L.Watterson et al., Phys. Fluids **28**, 2857 (1985)
- [31] R.Philipona et al., Phys. Fluids **B5**, 87 (1993)
- [32] P.C.Liewer et al., Nucl. Fusion **25**, 543 (1985)
- [33] R.J.Fonck et al., Plasma Phys. Control. Fusion **34**, 1993 (1992)
- [34] P.Cripwell et al., Proc. of 18<sup>th</sup> European Conf. on Controlled Fusion and Plasma Physics **14B**, Part I., 17 (1991)
- [35] T.L.Rhodes et al., Rev. Sci. Instrum. **63**, 4661 (1992)
- [36] T.L.Rhodes et al., Phys. Plasmas **9**, 2141 (2002)
- [37] G.D.Conway, Plasma Phys. Control. Fusion **39**, 407 (1997)
- [38] R.J.Groebner et al., Phys. Rev. Lett. **64**, 3015 (1990)
- [39] K.Ida et al., Phys. Rev. Lett. **65**, 1364 (1990)
- [40] A.R.Field et al., Nucl. Fusion **43**, 1191 (1992)
- [41] K.H.Burrell et al., Plasma Phys. Control. Fusion **34**, 1859 (1992)
- [42] E.J.Doyle et al., Phys. Fluids **B3**, 2300 (1991)
- [43] K.H.Burrell et al., Phys. Fluids **B2**, 1405 (1990)
- [44] A.R.Field et al., Proc. 18<sup>th</sup> European Conf. on Controlled Fusion and Plasma Physics, Berlin, **15C**, Part III, 113 (1991)

- [45] R.J.Groebner et al., Proc. 19<sup>th</sup> European Conf. on Controlled Fusion and Plasma Physics, Innsbruck, **16C**, Part I, 183 (1992)
- [46] R.J. Taylor et al., Phys. Rev. Lett. **63**, 2365 (1989)
- [47] R.R. Weynants et al., Plasma Physics and Controlled Nuclear Fusion Research 1990 (International Atomic Energy Agency, Vienna) **1**, 473 (1990)
- [48] K.Ida, Plasma Phys. Control. Fusion **40**, 1429 (1998)
- [49] K.C.Shaing et al., Phys. Fluids **B2**, 1492 (1990)
- [50] G.M.Staebler et al., Nucl. Fusion **31**, 1891 (1991)
- [51] A.B.Hassam et al., Plasma Phys. Control. Fusion **14**, 275 (1991)
- [52] B.A.Carreras et al., Phys. Fluids **B4**, 3115 (1992)
- [53] B.Scott, Physics of Plasmas **7**, 1845 (2000)
- [54] R.J. Groebner et al., Plasma Physics and Controlled Nuclear Fusion Research 1990 (International Atomic Energy Agency, Vienna) **1**, 453 (1991)
- [55] H.Matsumoto et al., Plasma Phys. Control. Fusion **34**, 615 (1992)
- [56] K.Ida et al., Phys. Fluids **B4**, 1360 (1992)
- [57] F.F.Chen, *Introduction to Plasma Physics and Controlled Fusion: Second Edition*, Plenum Press, New York, 1983
- [58] R.B.White et al., Plasma Physics **16** 565 (1974)
- [59] M.L.Pitteway, Proc. R. Soc. A **247**, 86 (1959)
- [60] E.Mazzucato, Review of Scientific Instruments **69**, 2201
- [61] S. Klenge, *Dynamik magnetisch eingeschlossener Plasmen am L-H Übergang*, PhD Thesis, Universität Stuttgart, Germany (2005)
- [62] W. Suttrop et al., Fusion Eng. Des. **60**, 297 (2002)
- [63] A.F.Harvey, *Microwave Engineering*, Academic Press, London, 1963
- [64] W.Schneider et al, Fusion Eng. Des. **48**, 127 (2000)
- [65] J.Schweinzer et al, Plasma Phys. Control. Fusion **34**, 1173 (1992)
- [66] H.Murmann et al., Review of Scientific Instruments **63**, 4941 (1992)
- [67] I.H.Hutchinson, *Principles of Plasma Diagnostics*, Cambridge University Press, Cambridge, 1987

- [68] E.Poli et al., *Comput. Phys. Commun.* **136**, 90 (2001)
- [69] K.H.Burrell et al., *Plasma Phys. Control. Fusion* **31**, 1649 (1989)
- [70] H.Zohm et al., *Nuclear Fusion* **35**, 543 (1995)
- [71] B.Scott, *Low frequency fluid drift turbulence in magnetised plasmas*, Habilitation Thesis, Universität Düsseldorf, Chapter 5
- [72] J.S.Bendat et al, *Measurement and Analysis of Random Data*, John Wiley & Sons, Inc., New York (1966)
- [73] T.Estrada et al., *Phys. Plasmas* **8**, 2657 (2001)
- [74] C.F.Maggi et al, 30<sup>th</sup> EPS Conference on Controlled Fusion and Plasma Physics, P1.63 (2003)
- [75] A.Kallenbach et al, *Nucl. Fusion* **30**, 645 (1990)
- [76] H.Meister et al, *Nucl. Fusion* **41**, 1633 (2001)
- [77] Y.B.Kim et al, *Phys. Fluids B3*, 2050 (1991)
- [78] D.Nishijima et al, *Plasma Phys. Control. Fusion* **47**, 2005 (89)
- [79] K.H.Burrell, *Phys. Plasmas* **4**, 1499 (1997)
- [80] Y.S.Na et al., submitted to *Nuclear Fusion*, (2005)
- [81] T.N.Carlstrom et al., *Phys. Plasmas* **3**, 1867 (1996)
- [82] H.Zohm, *Plasma Phys. Control. Fusion* **38**, 105 (1996)
- [83] R.J.Groebner et al., *Plasma Phys. Control. Fusion* **38**, 1249 (1996)
- [84] J.M.Noterdaeme et al., *Nucl. Fusion* **43**, 274 (2003)
- [85] J.E.Rice et al., *Nucl. Fusion* **38**, 75 (1998)
- [86] V.S.Chan et al., *Proc. 13th Topical Conf. on Radio Frequency Power in Plasmas*, Maryland, 45 (1999)
- [87] J.S.deGrassie et al., *Proc. 26th EPS Conf. on Controlled Fusion and Plasma Physics*, Maastricht, **23J**, 1189 (1999)
- [88] V.Rozhansky et al., submitted to H-mode workshop (2005)
- [89] G.Saibene et al., *Plasma Phys. Control. Fusion* **44**, 1769 (2002)
- [90] T.N.Carlstrom et al., *Plasma Phys. Control. Fusion* **36**, A147 (1994)

- [91] T.S.Taylor et al., Plasma Phys. Control. Fusion **36**, B229 (1994)
- [92] G.V.Pereverzev et al., IPP Report **5/98** (2002)
- [93] D.P.Coster et al, 32nd EPS Conference on Controlled Fusion and Plasma Physics, P1.008 (2005)
- [94] L.D.Horton et al, Nuclear Fusion **45**, 856 (2005)
- [95] S.I.Itoh et al., J. Phys. Soc. Japan **59**, 3815 (1990)
- [96] B.Kurzan et al., Plasma Phys. Control. Fusion **42**, 237 (2000)
- [97] M.Gilmore et al., Plasma Phys. Control. Fusion **42**, L1 (2000)
- [98] G.R.Hanson et al., Rev. Sci. Instrum. **61**, 3049 (1990)
- [99] E.Mazzucato et al., Phys. Rev. Lett. **71**, 1840 (1993)
- [100] Proceedings of the 7th International Reflectometry Workshop, Garching, Germany (2005)
- [101] E.Blanco et al., Review of Scientific Instruments **75**, 3822 (2004)
- [102] J.G.Blaschak et al., Journal of Computational Physics **77**, 109 (1988)
- [103] T.L.Rhodes et al., Plasma Phys. Control. Fusion **40**, 493 (1998)
- [104] J.S.Bendat et al., *Random Data Analysis and Measurement Procedures*, Wiley-Interscience, New York (1986)